2

UNITED
TECHNOLOGIES
RESEARCH
CENTER
East Hartford, Connecticut 06108

AFOSR-TR. 89-0439

R89-957334-1

Three Dimensional Flow and Temperature Profile Attenuation in an Axial Flow Turbine

REPORTED BY H. D. Joslyn

R. P. Dring

APPROVED BY R. W. Paterson

"Original contains color plates: All DTIC reproductions will be in black and white"

DATE March 15, 1989

NO. OF PAGES ____________ COPY NO. ____________

89

UNCLASSIFIED
SECURITY CLASSIFICATION OF THIS PAGE

REPORT DOCUMENTATION PAGE

Form Approved
OMB No. 0704-0188

1a. REPORT SECURITY CLASSIFICATION
Unclassified

1b. RESTRICTIVE MARKINGS

2a. SECURITY CLASSIFICATION AUTHORITY

2b. DECLASSIFICATION/DOWNGRADING SCHEDULE

3. DISTRIBUTION/AVAILABILITY OF REPORT
Approved for public release,
Unlimited distribution unlimited

4. PERFORMING ORGANIZATION REPORT NUMBER(S)

5. MONITORING ORGANIZATION REPORT NUMBER(S)
AFOSR-TR- 89-0439

6a. NAME OF PERFORMING ORGANIZATION
United Technologies
Research Center

6b. OFFICE SYMBOL (If applicable)

7a. NAME OF MONITORING ORGANIZATION
AFOSR

6c. ADDRESS (City, State, and ZIP Code)
Silver Lane
East Hartford, CT 06108

7b. ADDRESS (City, State, and ZIP Code)
Building 410
Bolling AFB, DC 20332

8a. NAME OF FUNDING/SPONSORING ORGANIZATION
AFOSR

8b. OFFICE SYMBOL (If applicable)
NA

9. PROCUREMENT INSTRUMENT IDENTIFICATION NUMBER
F49620-86-C-0020

8c. ADDRESS (City, State, and ZIP Code)
7b. AFOSR/NA
Bolling AFB, DC 20332

10. SOURCE OF FUNDING NUMBERS

PROGRAM ELEMENT NO.	PROJECT NO.	TASK NO.	WORK UNIT ACCESSION NO.
61102F	2307	A4	

11. TITLE (Include Security Classification)
Three Dimensional Flow and Temperature Profile Attenuation in an Axial Flow Turbine

12. PERSONAL AUTHOR(S)
Joslyn, H. David; Dring, Robert P.

13a. TYPE OF REPORT
Final

13b. TIME COVERED
FROM 12/15/85 TO 3/15/89

14. DATE OF REPORT (Year, Month, Day)
1989 March 15

15. PAGE COUNT
136

16. SUPPLEMENTARY NOTATION

17. COSATI CODES

FIELD	GROUP	SUB-GROUP

18. SUBJECT TERMS (Continue on reverse if necessary and identify by block number)
Turbine, Aerodynamics, Temperature Redistribution

19. ABSTRACT (Continue on reverse if necessary and identify by block number)

The strongly three dimensional and highly unsteady nature of the flow in axial turbines, has, until recently, defied in-depth analysis. On the other hand, the benefits that can be realized from an improved capability to predict the aerodynamics and heat transfer in turbines are numerous. These benefits include improved performance through higher efficiency, higher thrust-to-weight ratio through higher turbine inlet temperature, and improved durability through more precise predictions of local heat load.

Of particular interest in the present program were the aerodynamic mechanisms affecting the attenuation of a radial temperature profile in the flow as it passed through the turbine. The radial temperature profile in the flow exiting a combustor and entering a turbine can range from compressor exit temperature (≈1100°F) near the hub and tip end walls to a maximum (as high as 3200°F) in the midspan region. The heat load at any location on the turbine airfoils or end walls will depend strongly on the local gas temperature at that location and hence the mixing, or attenuation, of the inlet temperture profile is of critical importance.

The objective of this program was to examine the three dimensional nature of the flow in a turbine with particular focus on the mechanisms affecting the mixing and attenuation of an inlet temperature profile.

The present program has advanced the state-of-the-art by providing: (1) an exhaustive aero-dynamic data base for the three dimensional flow in a large scale axial turbine, (2) an exhaustive data base documenting the mixing of a simulated combustor exit temperature profile as it passed through the tubine, and (3) an assessment of a state-of-the-art three dimensional, time accurate, Navier-Stokes prediction of the flow in the turbine stage.

20. DISTRIBUTION/AVAILABILITY OF ABSTRACT
UNCLASSIFIED/UNLIMITED

21. ABSTRACT SECURITY CLASSIFICATION
UNCLASSIFIED

22a. NAME OF RESPONSIBLE INDIVIDUAL
H. HELIN

22b. TELEPHONE (Include Area Code)
202 767 0471

22c. OFFICE SYMBOL
AFOSR/NA

DD Form 1473, JUN 86 Previous editions are obsolete.

SECURITY CLASSIFICATION OF THIS PAGE
UNCLASSIFIED

ABSTRACT

The strongly three dimensional and highly unsteady nature of the flow in axial turbines has, until recently, defied in–depth analysis, ~~On the other hand,~~ the benefits that can be realized from an improved capability to predict the aerodynamics and heat transfer in turbines are numerous. These benefits include improved performance through higher efficiency, higher thrust–to–weight ratio through higher turbine inlet temperature, and improved durability through more precise predictions of local heat load.

Of particular interest in the present program were the aerodynamic mechanisms affecting the attenuation of a radial temperature profile in the flow as it passed through the turbine. The radial temperature profile in the flow exiting a combustor and entering a turbine can range from compressor exit temperature (≈1100°F) near the hub and tip end walls to a maximum (as high as 3200°F) in the midspan region. The heat load at any location on the turbine airfoils or end walls ~~will~~ depend strongly on the local gas temperature at that location. ~~and~~ hence the mixing, or attenuation, of the inlet temperature profile is of critical importance.

The objective of this program was to examine the three dimensional nature of the flow in a turbine with particular focus on the mechanisms affecting the mixing and attenuation of an inlet temperature profile.

The present program has advanced the state–of–the–art by providing: (1) an exhaustive aerodynamic data base for the three dimensional flow in a large scale axial turbine; (2) an exhaustive data base documenting the mixing of a simulated combustor exit temperature profile as it passed through the turbine; and (3) an assessment of a (507A) ~~state–of–the–art~~ three dimensional, time accurate, Navier–Stokes prediction of the flow in the turbine stage.

TABLE OF CONTENTS

TABLE OF CONTENTS (Concluded)

I. INTRODUCTION

I.1 BACKGROUND

Turbine heat transfer has historically been one of the "barrier technologies" in the development of the gas turbine. As the technology has advanced this fact has become even clearer. It is recognized that in the near future, "Turbines will be required to operate at near–stoichiometric (3500–4000°F) inlet temperatures, yet maintain efficiencies in the 88–94% range. Increased cooling effectiveness to 0.85 and reduced total cooling flows to 5% ..... are required to meet these goals." * This is, to say the least, a challenging situation.

The main focus of this challenge is in the complexity of the flow in a turbine. The flow is highly three dimensional due to both the inviscid and viscous flow mechanisms present. Even if the flowpath and airfoil geometries were only two dimensional the flow would still be strongly three dimensional. This situation can be expected to worsen because the trend in the industry is to increasingly three dimensional geometries since this leads in the direction of higher efficiency. There is further complexity in the fact that the flow is highly unsteady due to both random and periodic fluctuations, i.e. turbulence and stator/rotor interactions. The high levels of combustor–generated turbulence entering a turbine coupled with the wake–generated turbulence produced within the turbine, and the strong periodic unsteadiness resulting from the closely spaced stator and rotor rows, are known to have a powerful impact on the flow.

In spite of this formidable situation dramatic improvements have been achieved in engine performance through improved turbine cooling technology. These improvements can be seen in the fact that while allowable metal temperatures have only risen by approximately 200°F in the last 20 years, turbine inlet temperatures have risen by approximately 800°F in the same period. This improvement is due to advances in the areas of predicting external heat loads, improved film cooling schemes, and improved airfoil internal cooling schemes.

The thermal analysis of a turbine airfoil is based on the delicate balancing of aerodynamics and thermodynamics. The external aerodynamics dictates the nature of the inviscid velocity distribution on the airfoil surface. The surface boundary layer dictates the heat load that the airfoil internal cooling scheme must absorb. This heat load is influenced by at least two additional factors, the introduction of film cooling, and the potentially nonuniform distribution of adiabatic recovery temperature in the free–stream flow. The internal cooling scheme of the airfoil must be locally tailored to absorb the highly nonuniform heat load and to produce an airfoil surface temperature distribution which is acceptable both in terms of the temperature levels and their gradients. Most of these aspects of heat transfer technology have been the focus of intense research over the years.

* Quoted from the 1987 brochure for the Integrated High Performance Turbine Engine Technology initiative (IHPTET).

There is, however, a variety of turbine heat transfer mechanisms that have received very little attention for the simple reason that they are difficult to simulate experimentally. These are the mechanisms related to the actual turbine environment. They are related to the fact that the adiabatic recovery temperature of the combustor–generated flow entering the turbine is highly nonuniform, both circumferentially and radially. While the presence of these mechanisms has been acknowledged by the industry for many years there is no definitive body of information currently available to quantify their impact.

The designer's goal is to devise an airfoil cooling scheme which produces not only the desired averaged temperature, but also an acceptably uniform temperature, i.e., controlling the temperature gradients. Airfoils rarely burn out "on the average." They burn out locally. This necessitates designing a cooling scheme not for the average heat load, but for the local heat load. Since the adiabatic recovery temperature of the flow is the driving potential for the heat load, and since the adiabatic recovery temperature in the flow entering the turbine is highly nonuniform, it would be of value to be able to predict the attenuation (mixing) of the temperature profile through the turbine and the distribution of the recovery temperature on the airfoil and end wall surfaces. The data acquired in this program gives a basis on which designers can begin to estimate the distribution of the adiabatic recovery temperature in the flow as well as on the airfoil and end wall surfaces.

In brief, the present program provides documentation of the three dimensional flow in a one and one half stage turbine model. This documentation includes surface flow visualization, airfoil pressure distributions, and aerodynamic traverse data downstream of each airfoil row (total and static pressures, flow speed, yaw, and pitch). These experimental results are compared with results computed by Rai (1987) for this turbine. The redistribution of an inlet temperature profile was simulated by measuring the redistribution of an inlet trace gas profile. The trace gas concentration (simulating adiabatic recovery temperature) was documented locally on the airfoil and end wall surfaces as well as with traverse measurements in the flow.

I.2 TECHNICAL APPROACH

I.2.a Aerodynamics

Temperature profile attenuation occurs because of radial transport. If the flow remained on stream surfaces, as assumed in strip theory, existing prediction methods would be sufficient. It is an unavoidable fact, however, that there are always strong radial transport mechanisms in turbines. A partial list of these radial transport mechanisms divided into two broad categories is as follows.

Deterministic:

- End wall – airfoil boundary layer interactions
- Viscous and inviscid secondary flows
- The relative eddy
- Rotor tip leakage
- Airfoil boundary layers
- Airfoil wakes
- Wake – airfoil interaction
- Leading edge horseshoe vortices
- Three dimensional airfoil and end wall geometries

Diffusive:

- Molecular diffusion
- Turbulent diffusion

At the outset of this program it was anticipated that the deterministic mechanisms would be dominant. An analysis by Adkins and Smith (1982) based on these mechanisms had been successful in predicting many aspects of spanwise mixing in a number of axial compressors. Since that time, however, something of a controversy has arisen over the relative contributions of the deterministic and diffusive mechanisms. The works of Gallimore and Cumpsty (1986) and Gallimore (1986) pointed out that a model based on diffusive mechanisms could also predict many aspects of spanwise mixing in axial compressors. More recently Wisler, Bauer and Okiishi (1987) have demonstrated that there are regions of the flow in an axial compressor where one or the other mechanism dominates.

All of this previous work has been in axial compressors. The flow in axial turbines is, to put it mildly, very different. Turbines have strong flow accelerations and much higher flow turning. The secondary flows in turbines are also much stronger. The motivation for the aerodynamic documentation of the turbine was to be able to quantify the relative strengths of these mechanisms.

In this experiment the turbulence at the turbine inlet (Plane 1) is small relative to the turbulence exiting a combustor. The LSRR inlet turbulence at Plane 1 is 0.5% while estimates of the turbulence in combustor exit flows are in the vicinity of 10%. This issue of the relative importance of the deterministic and diffusive mechanisms would, to a degree, be answered by an experiment with a high turbine inlet turbulence. However, this is beyond the scope of the present program.

Since the beginning of this program there has been a dramatic advancement in the computational state–of–the–art. The first evidence of this was seen in the work by Rai (1987) in which he calculated the flow through the entire LSRR first stage. His calculation was three dimensional, compressible, viscous, and in a time accurate manner it captured the unsteadiness due to stator–rotor interaction. Accordingly, carrying out an in–depth assessment of Rai's computation became a major element of the present program.

A study of the effect of an inlet temperature profile on turbine performance was carried out by Stabe et al. (1984). They studied a single stage gas generator turbine with an axisymmetric inlet temperature profile. Their results indicated that turbine aerodynamic performance was very insensitive to the inlet temperature profile. It should be pointed out, however, that the magnitude of the temperature profile they used was very weak when compared to those commonly occurring in engines.

In summary, the intent of the aerodynamic portion of the experiment was to document three dimensional flow in a turbine, i.e., the radial transport. This was to be done by measuring the fullspan pressure distributions and by obtaining surface flow visualization on all three rows of airfoils. In addition, fullspan radial/circumferential traverse data was to be obtained in the flow downstream of each airfoil row. This traverse data was to include the total and static pressures and the flow yaw and pitch angles. From these results the axial, tangential, and radial components of the local velocity vectors could be determined.

I.2.b Trace Gas Simulation

The primary objective of the program was to determine the degree to which an axisymmetric inlet temperature profile was attenuated, or mixed out, by the three–dimensional aerodynamic mechanisms present in a turbine. This was accomplished by measuring the aerodynamic flow field in the turbine and by measuring a simulated temperature profile as it was convected through the turbine. It was recognized that the temperature drop due to work extraction was not modeled by this approach, however, this aspect of the temperature field can be determined on a first principles basis.

Outside of the work extraction process, the temperature field does not play a major role in the three–dimensional nature of the flow in a turbine. Munk and Prim (1947) demonstrated that temperature gradients do not affect the streamline pattern of a flow. Their analysis, however, was restricted to flows in the absolute frame of reference. An extension of these concepts to the rotating frame of reference was demonstrated by Hawthorne (1974). He showed that secondary vorticity in the rotating frame of reference could be generated by gradients in the rotary total pressure as well as by gradients in the rotary total temperature (or density). For constant density flow in the rotating frame, the rotary total pressure is the kinematic equivalent of total pressure in the absolute frame in that a gradient in rotary total pressure is required to generate secondary vorticity. As pointed out by Hawthorne (1974) in the discussion of his Eq. 54, the effects of the rotary total pressure and temperature gradients will generally reinforce each other. However, it can also be seen in Hawthorne's Eq. 54 that the pressure gradient term should generally dominate the temperature gradient term.

The conclusion here was that, in spite of the fact that the work extraction process and density gradients were not being modeled, the trace gas technique would give a reasonable simulation of the attenuation of an inlet temperature profile.

The application of the mass transfer analogy to obtain heat transfer information, i.e., temperature field redistributions, has been well documented in the past by Eckert and Goldstein (1976), Pederson et al. (1977), and by Dring et al. (1980). The main assumption in this analogy is that throughout the flow field the turbulent Prandtl number (which governs heat transfer) and the turbulent Schmidt number (which governs mass transfer) vary in such a manner that their ratio, the turbulent Lewis number is close to unity at all points. This assumption has been shown to be accurate for turbulent wakes and jets by Reynolds (1976). Although there are basic differences in the flow, it was expected that the analogy would be even better in the present turbine flow field due to the large scale viscous and inviscid radial flow mechanisms present.

The simulation was carried out using a distribution of a trace gas to simulate the total temperature field, that is, the radial temperature profile at the turbine inlet was simulated with a radial (axisymmetric) profile of trace gas concentration. Carbon dioxide was chosen as the trace gas. Its molecular weight (44) is somewhat greater than that of air (29) but it has the advantages that it is neither toxic nor combustible. Other experimenters have used ethylene as a trace gas because its molecular weight (28) is close to that of air. The safety hazard of using large quantities of a combustible gas precluded its application in the present experiment. The effects of the molecular weight of the trace gas are essentially eliminated as a result of the very low concentration levels used in the experiment. The maximum concentration was typically 1500 ppm (1000 to 1200 ppm above ambient), or 0.15%.

The mass transfer analogy was chosen to study turbine inlet temperature profile attenuation since, for the present application, a mass transfer process could be set up with greater accuracy in the boundary conditions. This included a well defined axisymmetric inlet trace gas profile and "adiabatic" surfaces throughout the turbine model. In addition, a mass transfer process could be studied more accurately and more economically than the corresponding thermal process.

The trace gas technique was applied to the problem of turbine temperature profile attenuation in a "proof–of–principles" experiment by Joslyn and Dring (1988). This paper demonstrated both the techniques necessary to generate the desired inlet profile as well as the measurement technique and its application in both the absolute and rotating frames of reference.

I.3 PREVIOUS STUDIES ON THE UTRC/LSRR TURBINE MODEL

As a result of the large variety of experiments that have been carried out on the Turbine Model in the UTRC/LSRR it has become a popular benchmark on which to carry out assessments of various physical models and computational methods. A brief summary of these references is given below. Complete citation information is given in the REFERENCES.

Aerodynamics (Experimental)
- — Dring and Joslyn (1981)
- — Dring, Joslyn, Hardin and Wagner (1981)
- — Dring and Joslyn (1983)
- — Joslyn and Dring (1983)
- — Joslyn, Dring and Sharma (1983)
- — Sharma et al. (1985)
- — Sharma et al. (1988)

Aerodynamics (CFD)
- — Rai (1987)
- — Rai and Dring (1987)
- — Madavan, Rai and Gavali (1989)
- — Adamczyk et al. (1989)

Axisymmetric profile attenuation
- — Joslyn and Dring (1988)

Nonaxisymmetric effects (hot streaks and phantom cooling)
- — Butler et al. (1986)
- — Rai and Dring (1987)
- — Roback, Dring and Joslyn (1988)

Heat transfer and film cooling
- — Dring, Blair and Joslyn (1980)
- — Dring, Blair and Joslyn (1987)
- — Dring et al. (1988)
- — Blair, Dring and Joslyn (1989a)
- — Blair, Dring and Joslyn (1989b)

II. DESCRIPTION OF THE EXPERIMENT

II.1 LARGE SCALE ROTATING RIG (LSRR)

The Large Scale Rotating Rig (LSRR) was designed for carrying out detailed experimental investigations of the flow within turbine and compressor airfoil rows. Primary considerations were to provide a facility which would: (1) be of sufficient size to permit a high degree of resolution of three–dimensional flows, (2) possess a high degree of flexibility in regard to the configurations which could be tested, and (3) enable measurements to be made directly in the rotation frame of reference.

The facility is of the open circuit type. Flow enters through a 12 foot diameter inlet. A 6 inch thick section of honeycomb is mounted at the inlet face to remove any cross–flow effects. The inlet smoothly contracts the cross section down to a 5 foot diameter. The flow then passes through three fine mesh screens to reduce the turbulence level.

The test section consists of a series constant diameter casings enclosing the first stage stator and rotor, and the second stator of the turbine model (Figs. II–1 and II–2). The turbine has a hub/tip ratio of 0.8 and all three airfoils have aspect ratios close to unity (Fig. II–3). As can also be seen in Fig. II–3, the axial gaps between the rows can be varied greatly. In a previous study of rotor–stator interaction (Dring et al., 1981) the gap between the first stage stator and rotor was set at both 15% and 65%. The midspan sections of the first stage airfoils are shown in Fig. II–4 in the 15% gap configuration. In the present program the 50% gap configuration was used. This was done to enable traverse data to be taken at Plane 2 (which is 17% behind the first stator) and at Plane 3 (which is 36% behind the rotor). The percentages here are in terms of airfoil axial chord. Traverse data was also taken at Plane 4 which is 14% behind the second stator. Inlet traverse documentation was done at Plane 1 which is 97% upstream of the first stator leading edge.

Downstream of the test section the flow passes through an annular diffuser into a centrifugal blower and is discharged from the rig. A vortex valve at the blower inlet controls the flow rate. The blower can provide a pressure rise of up to 21 inches of water. This enables axial velocities in the turbine test section of up to 80 feet per second. The rotor is driven or braked by a hydraulic pump and motor system which is capable of shaft speeds up to 890 rpm.

II.2 AERODYNAMIC INSTRUMENTATION

Aerodynamic instrumentation is available in the LSRR for making both steady–state and high–response measurements of aerodynamic flow parameters including: total pressure, static pressure, flow velocity, flow direction, and temperature. These capabilities exist in both the stationary and rotating frames of reference. The stationary frame probe traverse mechanism can be positioned at selected axial planes. This traverse mechanism can drive a probe radially, circumferentially, and rotate it in yaw. A separate traverse mechanism for the rotating frame of reference is mounted inside the hub. This traverse can also drive a probe radially, circumferentially, and in yaw.

A dedicated, on–line, automatic, data acquisition and control system is used to monitor and control the experiment. This system calibrates all transducers (in both the rotating and stationary frames), monitors the turbine flow coefficient (C_x/U_m) , controls probe position, and acquires, reduces, prints, and plots the data.

All of the traverse and rake probes, both the Kiel probes as well as the 5–Hole probe, were standard United Sensor products.

The instrumentation in the LSRR that was used in this program was as follows.

Airfoil static pressure and trace gas sampling sites –
    22 locations around each airfoil perimeter and at
    7 spanwise locations; 3, 12.5, 25, 50, 75, 87.5, and 98% span

Hub and Tip end wall trace gas sampling sites –
    ≈30 on each end wall

Rotor leading edge trace gas sampling rake –
    17 elements located radially in the rotor leading edge plane

Traverses (5–Hole probe and trace gas sampling) –

Plane 1 (Inlet, 97% upstream of the first stator)
Radial traverse at 4 circumferential locations

Plane 2 (17% aft of the first stator)
Radial/Circumferential traverse in the stationary frame from 5 to 95% span over 2 first stator pitches and, a 17 element rake mounted on the rotor hub in the plane of the rotor leading edge.

Plane 3 (36% aft of the rotor)
Radial/Circumferential traverse in the rotating frame from 5 to 95% span over 2 rotor pitches and, Radial/Circumferential traverse in the stationary frame from 5 to 95% span over 2 first stator pitches

Plane 4 (14% aft of the second stator)
Radial/Circumferential traverse in the stationary frame from 5 to 95% span over 2 first stator pitches (data at this plane was averaged over 2 second stator pitches.)

II.3 TRACE GAS INSTRUMENTATION

The LSRR has an independent system to measure trace gas concentration. Concentrations were determined by drawing a gas sample through either a conventional surface static pressure tap, through a rake in the flow, or through a traverse probe in the flow. The static pressure taps were located both on the airfoils and on the end walls. Measurements were made in both the stationary and rotating frames of reference.

Gas samples were drawn from the sampling site (tap, rake or probe) and fed into a gas analyzer. Since carbon dioxide was used as the trace gas, a Beckman Non–Dispersive Infrared (NDIR) analyzer (Model 865) was used to measure the concentrations. The output of the NDIR was acquired, recorded, printed and plotted by its own dedicated minicomputer. This computer also calibrated of the NDIR using a series of calibration gases. The accuracy of the NDIR was 5 ppm. Ambient concentration varied between 300 and 500 ppm. The inlet concentration profile varied from ambient near the end walls to 1000 to 1500 ppm above ambient at its maximum.

This trace gas measurement technique has been demonstrated previously in the LSRR turbine model in studies of the redistribution of (1) an axisymmetric inlet radial profile (Joslyn and Dring, [1988]) and (2) a simulated combustor generated hot–streak (Butler et al., [1986]).

The measurement sites for the trace gas testing were the same as those for the aerodynamic testing. They are summarized at the end of Section II.2.

II.4. DATA PRESENTATION FORMAT

All of the data that were acquired in this program were reduced to dimensionless parameters. The aerodynamic pressure data were reduced to a pressure coefficients based on the turbine inlet total pressure (PTOA) and a dynamic pressure (Q_{Um}) based on the midspan wheel speed (U_m). The velocities were nondimensionalized with the midspan wheel speed. Flow angles were measured from the axial direction. "Circumferentially averaged" flow angles were based on averaged velocity components rather than on averaged angles. All this is summarized as follows.

Absolute total pressure,	CPTABS	= (PTOA – PTABS)/Q_{Um}
Relative total pressure,	CPTREL	= (PTOA – PTREL)/Q_{Um}
Rotary total pressure,	CPTROT	= (PTOA – PTROT)/Q_{Um}
Static pressure,	CPS	= (PTOA – PS)/Q_{Um}
Absolute speed,	C	= (C/U_m)
Relative speed,	W	= (W/U_m)
Axial speed,	CX	= (C_x/U_m)
Absolute tangential speed,	CT	= (C_t/U_m)
Relative tangential speed,	WT	= (W_t/U_m)

Area–average of any quantity “X”, XAA $= X^{-a}$

Mass–average of any quantity “X”, XMA $= X^{-m}$

The trace gas concentration data was also reduced to a dimensionless coefficient based on the maximum and minimum (ambient) concentrations at the turbine inlet, Plane 1.

$$F = (C - C_{min})/(C_{max} - C_{min})$$

where C_{max} and C_{min} are at Plane 1 and where $C_{min} \approx C_{amb}$. Thus, throughout the turbine the concentration parameter varied between 0.0 and 1.0. The nominal C_{max} was based on the average of a number of radial surveys at the turbine inlet plane. Since the concentration in the incoming flow was not precisely axisymmetric, there are small regions in the flow where the concentration parameter exceeded 1.0.

All circumferential averages of the concentration parameter are area–averages.

III. TEST CONDITIONS

III.1 NOMINAL AERODYNAMIC CONDITIONS

Because the flow in the LSRR is essentially incompressible ($M < 0.2$) there is only one parameter that controls the velocity triangles, the flow coefficient, C_x/U_m . The nominal design value of the flow coefficient for the turbine model is 0.78. Although the turbine has been operated over a wide range of flow coefficient in the past (Blair, Dring and Joslyn, 1989b), in the present program all of the data were acquired at the nominal design value. This was done by setting the shaft speed to 410 rpm and the axial velocity at the model inlet (Plane 1) to 75 ft./sec. At these conditions, the Reynolds numbers for the three airfoils (based on axial chord and midspan exit flow speed) were as follows.

First Stator	$6.4x10^5$
Rotor	$5.8x10^5$
Second Stator	$5.9x10^5$

The turbine model has been operated in the past with different levels of inlet turbulence. The nominal inlet turbulence level is 0.5%. By installing a turbulence generating grid, values as high as 10% have been produced (Blair, Dring and Joslyn, 1989b). The turbulence generating grid was not used in the present experiment and hence the inlet turbulence level was 0.5%.

The hub and tip boundary layers at the turbine inlet (Plane 1) were characterized as follows.

Plane 1 (97% upstream of the stator)	Hub	Tip
Displacement thickness (% span)	0.9	1.5
Momentum thickness (% span)	0.7	1.1
Thickness @ 99% free stream (% span)	5.5	10.0

III.2 INLET TRACE GAS PROFILE

The inlet trace gas profile was generated with an array of five concentric injector rings located in a plane 63 inches upstream of the first stator leading edge. The center body ended 24 inches upstream of the leading edge and hence the flow velocity around the injector rings was very low. The rings were located far enough upstream of the first stator (approximately 13 chords) such that their wakes were completely mixed out at the inlet traverse plane (Plane 1). The 3:1 flow area contraction between the rings and Plane 1 (due to the 0.8 hub/tip ratio) also contributed to the absence of the ring wakes.

The injector rings were fabricated from stainless steel tubes 0.5 inches in diameter. This was large enough such the static pressure in the rings was constant circumferentially. Around the circumference of each ring 144 miniature brass nozzle inserts, 0.020 inches in diameter, were uniformly distributed.

Trace gas (carbon dioxide) was injected into the flow simultaneously through all five rings. By independently controlling the flow to each ring the radial trace gas concentration profile at Plane 1 could be tailored to simulate any number of combustor exit (turbine inlet) temperature profiles. The profile used in this program was lowest at the hub and tip (i.e., ambient concentration, ≈ 400 ppm) and had its maximum near 60% span (typically 1200 ppm above ambient). This type of profile was typical of a wide range of engine applications.

The single major problem in this approach was in achieving an acceptable degree of axisymmetry in the inlet trace gas profile (at Plane 1). This problem was aggravated by small differences in the size of the 720 holes in the injector rings and by minuscule distortions in the flow over the rings. The problem was further complicated by the fact that while a large number of inlet surveys would be needed to exhaustively document the inlet concentration distribution, practicality limited us to a relatively small number. In this program surveys in Plane 1 were carried out at 4 circumferential locations. It will be shown in the discussion of the results that follows that a reasonably axisymmetric distribution was achieved.

IV. COMPUTATIONAL PREDICTION

The data collected in this program was used as a basis for assessing the computational prediction by Rai (1987) of the flow through the first stage (stator and rotor). The prediction is based on a three–dimensional, unsteady, thin–layer Navier–Stokes code. Although the code was time–accurate, the assessment was limited to time–averaged results. The code used patched and overlaid grids that moved relative to each other to simulate the relative motion of the stators and rotors. The turbulence model was a modified Baldwin–Lomax model (Baldwin and Lomax, 1978, and Hung and Buning, 1985). The hub and tip boundary layers as well as the flow through the rotor tip clearance gap were all modeled in the calculation.

Although the code (Rai, 1987) was run at the actual Mach and Reynolds numbers of the experiment, there were a number of geometric differences. Since there were 22 first stator airfoils and 28 rotor airfoils in the turbine model, complete geometric similarity, i.e., the same airfoil count ratio, would have required a calculation with 25 airfoils ([22 + 28]/2). In order to reduce the computation time the rotor chord and pitch were both increased by a factor of ([14/11] = 1.273). This permitted a calculation with only 2 airfoils. The major impact of this approximation was to reduce the rotor aspect ratio (span/axial chord) by a factor of 1.273 from 0.95 in the experiment to 0.74 in the calculation. This reduction tended to cause an increase in the extent of the predicted rotor secondary flows.

In addition, the calculation was run with a 15% axial gap between the stator and the rotor. This gap was chosen in order to duplicate that of the rotor/stator interaction experiment carried out by Dring et al. (1981). Keep in mind, however, that the axial gap in the present experiment was 50% (see Fig. II–3). This, and other earlier works (Blair, Dring and Joslyn [1989a & 1989b]) have shown that axial gap has no significant impact on either the time–averaged pressure distributions or the time–averaged heat transfer coefficients on the stator or the rotor. This does not mean, however, that the secondary flow and other viscous mechanisms are unaffected by the stator/rotor axial gap.

The final geometric difference was that while the rotor tip clearance in the experiment was 1.0% of span, the clearance in the calculation was 0.4% of span. Because of these differences in the rotor aspect ratio and tip clearance, the present assessment was limited to the stator flow. It was felt that the small rotor aspect ratio in the computation would have resulted in unrealistically strong secondary flow and that the small tip clearance would have resulted in an unrealistically weak leakage flow.

An improved version of the code has been presented by Madavan et al. (1989). This version had a finer grid (twice as many grid surfaces in the spanwise direction) and had been applied to the same turbine but with the rotor aspect ratio held at 0.95 and the stator aspect ratio reduced by the factor of 1.273 from 1.01 to 0.79. Generally speaking, the two calculations were in good agreement but the fine grid calculation gave better results in the regions near the airfoil and end wall surfaces. This calculation, however, also had the small rotor tip clearance used by Rai, 1987 (0.4% of span vs. 1.0% in the experiment).

It is anticipated (Rai, 1989a) that a calculation will soon be carried out in which the rotor aspect ratio, the rotor tip clearance, and the stator–rotor axial gap are equal to the experimental values. A comparison of the computational and experimental results for the flow over the rotor will be carried out at that time.

A number of final comments regarding the code are as follows. Earlier predictions with a two–dimensional version of the code for both the steady and unsteady airfoil static pressures at midspan were in good agreement with experimental data (Rai, 1987). Improvements in the two–dimensional version of the code to account for airfoil count ratios other than unity were shown to give even better results (Rai and Madavan, 1988). Although limited to an airfoil count ratio of unity, the three–dimensional versions of the code gave a similar good prediction of the unsteady airfoil static pressures at midspan.

The present assessment was carried out by comparing the experimental results with the time averages of the computed results presented by Rai (1987). Dr. Rai provided the time–averaged stator and rotor pressure distributions and the airfoil and end wall limiting streamlines. Dr. Rai also provided the time–averaged values of the components of the velocity vectors and the time–averaged static pressure.

Time–averaged computed results in the absolute frame were provided at a plane 9% downstream of the stator trailing edge, versus 17% in the experiment (Fig. II–3). Absolute, relative, and rotary total pressures were calculated from these results. Comparisons with the rotor results will await the availability of computed results for the correct rotor aspect ratio, tip clearance, and axial gap.

The computed results were presented using the same plotting format that was used for the experimental results. However, the points plotted were the computational grid points instead of the traverse measurement locations.

Generally speaking, the agreement between the results computed by Rai (1987) and the experimental results was extremely encouraging. Most of the physical mechanisms seen in the experiment were also evident in the computation. While the qualitative agreement was excellent the quanitative agreement varied. In the section that follows, the measured and computed results will be presented and discussed together.

V. MEASURED RESULTS AND COMPUTATIONAL ASSESSMENT

The discussion of the measured results and the assessment of the computation (Rai, 1987) will be done simultaneously and in the following order.

Aerodynamics Results:
- Surface limiting streamlines
- Airfoil pressure distributions
- Aerodynamic traverse results

Trace Gas Results:
- First stator
- Rotor
- Second stator

Since the discussion is related closely to the figures, the text will be tied to each figure being discussed by a heading. The purpose of this is to improve cross–referencing between the text and the figures.

V.1 AERODYNAMICS RESULTS

V.1.a Surface Streamlines

Figs. V–1 through V–4

The first comparisons between the measured and computed results were based on the surface streamlines. This comparison was made first since these patterns very quickly give a clear impression of the three–dimensional nature of the flow through the turbine. The experimental results (Figs. V–1 through V–3) were obtained by bonding Ozalid paper to the airfoil and end wall surfaces and then flowing a small amount of gaseous ammonia back through the surface static pressure taps. The ammonia reacted with the paper leaving permanent blue streaks. In some cases the ammonia was introduced through a fine hypodermic tube in the flow. The computed results (Fig. V–4) were generated by tracking particles as they were convected (in the time–averaged flow) along the computational grid surface closest to the airfoil or end wall.

The flow visualization on the suction surfaces of the first and second stators and on the pressure surface of the rotor is shown in Fig. V–1. The hub end wall flow visualization is also shown. This photograph was constructed by making a model of the turbine and bonding the exposed Ozalid paper to it. In a similar manner, the flow visualization on the pressure surfaces of the first and second stators and on the suction surface of the rotor is shown in Fig. V–2. The tip end wall flow visualization for the first and second stators is shown in Fig. V–3. For the sake of clarity arrows have been added to the streaks on the Ozalid paper.

The measured and computed results were in rather good agreement on the first stator. They indicated a midspan region which was very nearly two–dimensional on both the suction and pressure surfaces. The hub and tip secondary flows were clearly apparent near the end walls on the airfoil suction surface, with that at the tip being the stronger of the two. The hub and tip end wall results showed the over–turning due to secondary flow. Horseshoe vortices at the hub and tip leading edges were evident near the end walls on the forward portion of the airfoil pressure surface as well as on the end walls themselves.

The difference between the rotor aspect ratio used in the experiment (0.95) and in the computation (0.74) caused the measured and computed results to differ quantitatively (but not qualitatively). In particular, the lower aspect ratio in the calculation caused the secondary flows on the suction surface to be stronger than in the experiment. In the calculation the hub and tip secondary flows merged at 67% span whereas in the experiment they merged at about 55% span. This may also have been due in part to the small rotor tip clearance used in the calculation (0.4% versus 1.0%).

The dominant feature on the rotor pressure surface was the radial flow toward the tip due to the relative eddy. This is an inviscid mechanism due to the relative vorticity in the rotating frame of reference. Its effect was strongest on the forward portion of the pressure surface because the surface flow speed was lowest there (Dring and Joslyn, 1983). The surface streamlines turned away from the radial direction as the flow accelerated toward the trailing edge. The hub end wall flow showed the strong over–turning due to secondary flow.

The surface flow on the second stator was similar to that on the first stator. This was true in spite of the fact that this stator was geometrically far more similar to the rotor. The midspan region on both the suction and pressure surfaces was relatively two–dimensional. The region influenced by the tip secondary flow was much larger than that influenced by the hub secondary flow. This aspect of the similarity was due to the fact that both stators had a large exit swirl and hence a strong radial static pressure gradient. This gradient tended to drive low total pressure fluid, such as that in the secondary flow vortices, inward toward the hub. The absence of radial flow on the pressure surface was due to the stator being in the stationary frame of reference and hence having no relative eddy. The flow on the hub end wall showed clear evidence of over–turning due to secondary flow, and also the presence of a leading edge horseshoe vortex.

V.1.b Airfoil Pressure Distributions

Fig. V–5

The midspan static pressures for the three turbine airfoils are shown in Fig. V–5. All three airfoils are included here but the axial gaps between them are not drawn to scale. Also included in the figure are the absolute and relative total pressures and the static pressures in the axial gaps between adjacent airfoil rows. These were obtained from the traverse results acquired downstream of each airfoil row at midspan.

These results show the drop in the static and total pressures across each row and across the turbine. It can also be seen that in spite of the generally favorable static pressure gradients, there are also strongly adverse pressure gradient regions on the suction surface of each airfoil.

Fig. V–6

Comparisons of the measured and computed results for the first stage stator and rotor are shown in Fig. V–6 for the 2%, 50% and 98% span locations. The curves are the time–averaged computed results and the symbols are the measured results.

The measured rotor pressure distribution data are shown as pairs of symbols at the 2% and 50% span locations. These two symbols represent the range of the measurements that have been taken on the rotor during the various experiments that have been conducted between 1977 and 1988. A similar comparison for the first stator showed that the range of measurements for this airfoil was within the size of the symbols.

The computed results for the stator and rotor are by Rai (1987). This comparison was made in spite of the fact that the rotor aspect ratio in the computation was low (by the factor of 11/14) and in spite of the fact that the tip clearance was too small (0.4% vs. 1.0% span). The results by Madavan et al. (1989), however, showed that the impact of the rotor aspect ratio on the rotor pressure distributions was relatively small. The same can not necessarily be said for the effect of rotor tip clearance, especially at the 98% span location. This question remains to be answered (Rai, 1989a).

In general, the agreement between the measured and computed pressure distribution results was excellent. For the stator the agreement was excellent from hub to tip. For the rotor the agreement at the hub was reasonably good and the results of Madavan et al. (1989) show that the suction surface agreement gets better when the correct aspect ratio (and a finer computational grid) were used. At the rotor midspan agreement was excellent. At the tip, however, there was a difference between the measured and computed results on the aft portion of the rotor suction surface. This discrepancy may well have been due to the small tip clearance used in the Rai (1987) calculation.

Fig. V–7

Since the calculations by Rai (1987) and Madavan et al. (1989) included only the first stage stator and rotor, the measured pressure distributions for the second stator were compared with the two–dimensional potential flow analysis by Caspar et al. (1980). It should be noted, however, that this calculation included the effects of total pressure loss and streamtube contraction. The symbols in Fig. V–7 represent the measured results and the curves represent the computed results. The aerodynamic input to the to the potential flow analysis included the inlet and exit flow angles, the stream tube contraction, and the total pressure loss (or gain). All of this input was calculated from the circumferentially averaged traverse data at the appropriate span location. This approach does not account for the fact that there was significant radial transport upstream of, within, and downstream of the airfoil.

The agreement between the measured and computed results for the second stator (Fig. V–7) was reasonably good, especially on the pressure surface. The measured and computed results on the suction surface showed the same trend of the minimum pressure moving forward from the hub (2% span) to the tip (98% span). The suction surface results at the tip suggested that the second stator was operating with a less positive incidence than that which was calculated from the rotor exit traverse data. The rotor exit traverse data (Fig. V–9k) showed some very strong gradients in absolute flow angle due to the rotor tip leakage in this region. Thus there was a strong likelihood that the actual stator incidence was significantly different than that used in the calculation.

This completes the discussion of the measured and computed pressure distribution results. In general the agreement was good but it was shown that radial mixing can have a significant impact on the affective incidence an airfoil responds to. The surface streamlines as well as the airfoil pressure distributions indicated that all three rows of airfoils were free of any significant boundary layer separation.

V.1.c Traverse Results

The contour plots of the various measured and computed (Rai, 1987) quantities were based on the same plotting routine. In order to get a feeling for the number of points (both measured and computed) that went into these plots, the individual points were plotted in the secondary flow vector plots (Fig. V–8i). The measurement locations were especially dense in the regions where the gradients were, strong, i.e., in the wakes and near the end walls. Note that, in order to demonstrate periodicity, the measurements were taken over two first stator pitches. For the sake of clarity a large number of radial grid locations near the end walls have been deleted in the computed figure. Although the computation was over one first stator pitch, it has been repeated over a second pitch in order to be geometrically similar to the measured data.

Both the measured and the computed results have been plotted with the same increments between contours, as follows.

Quantity	Contour Increment
CPTABS	0.10
CPTROT	0.10
CPS	0.10
(C/U_m)	0.05
(W/U_m)	0.05

The measured and computed results were also plotted together in terms of the spanwise distributions of their circumferential averages. Two circumferential averages were used in these comparisons depending on the specific quantity being averaged. The two averages were the area–average and the mass–average. They are defined as follows.

Area–average of a quantity, "F":

$$F^{-a} = FAA = \int_0^\tau F \cdot dy \Big/ \int_0^\tau dy$$

Mass–average of a quantity, "F":

$$F^{-m} = FMA = \int_0^\tau F\varrho C_x \cdot dy \Big/ \int_0^\tau \varrho C_x dy$$

The choice of which average was used was based on through flow analysis considerations (Dring and Oates, 1989a and 1989b). The particular average used for each quantity is summarized below.

Quantity	Area Avg. (AA) or Mass Avg. (MA)
CPTABS	MA
CPTROT	MA
CPS	AA
(CX/UM)	AA

Absolute and relative flow angles were also calculated based on the way they would be used in a through flow calculation, i.e., as the arctangent of the ratio of the area–averaged tangential and axial velocity components (CTAA or WTAA and CXAA). The absolute and relative flow angles were calculated as follows.

$$\alpha = \text{Arctan (CTAA/CXAA)}$$

$$\beta = \text{Arctan (WTAA/CXAA)}$$

Finally, in the plots of the secondary flow velocity vectors, the length of the arrows was proportional the the secondary flow speed. The same proportionality factor was used for both the measured and computed results. The secondary flow vectors represent the total velocity vector viewed from a particular direction. This viewing direction was on a cylindrical surface and in the yaw direction corresponding to the averaged flow angle at a particular radius. In general this averaged yaw angle was calculated at midspan (50% span), however, in one case it was calculated at 90% span in order to show the rotor tip leakage vortex more clearly.

Fig. V–8a

Total pressure contours at Plane 2 in the flow downstream of the first stator were shown in Fig. V–8a. The measured results were for a location 17% aft of the trailing edge and the computed results (Rai, 1987) were for a plane 9% aft (see Fig. II–3). Both sets of results were for airfoils with the same aspect ratio.

The measured and computed results were in excellent qualitative agreement. Both show the migration toward the hub of the low total pressure hub and tip secondary flow regions. The measured and computed low total pressure regions were also close in terms of the local loss. Both results have a maximum local loss of about 1.5 for the tip secondary flow (near 65% span) and 2.5 for the hub secondary flow (near 13% span). The measured results indicated a thicker end wall boundary layer at the tip than at the hub. This was due in part to the thicker inlet (Plane 1) boundary layer at the tip (see Section III.1). The computed end wall boundary layers were thin because they started at Plane 1.

Fig. V–8b

The computed results in Fig. V–8a in general have not captured the magnitudes of the local gradients. This is due the coarseness of the grids used. The significant improvement that Madavan et al. (1989) were able to obtain with a finer grid confirms this. The problem was clearest at midspan. The circumferential variation of the midspan results in Fig.V–8a was shown in Fig. V–8b. This plot included both the inlet total pressure at Plane 1 (CPTABS = 0) as well as the total and static pressures at the stator exit (Plane 2).

The computed static pressure distribution had a much greater variation than the measured distribution. This was primarily due to the fact that while the measurement plane was 17% aft of the stator the computational plane was only 9% aft (see Fig. II–3).

The measured total pressure profile in Fig. V–8b was not only very periodic, but it also showed that the total pressure in the potential flow region between the wakes was equal to the inlet value (as expected). While the depth of the computed wake was similar to the measured value, it was approximately twice as wide. In addition, in the region between wakes there were small positive and negative differences between the computed total pressure and the inlet value. The reason for these small differences is not clear at this time. It was felt that they may be due in part to the fact that the total pressure was computed from the time–averaged static pressure and velocity components. A truly time averaged total pressure might behave differently, however, it might still have this behavior due to the unsteadiness in the flow.

Fig. V–8c

The mass averaged total pressure loss (ΔPT/QUm) at midspan for the measured first stator wakes shown in Fig. V–8b was 0.14. A boundary layer analysis (Edwards et al. [1981], and Carter et al. [1982]) using the turbulent mixing model by Cebeci and Smith (1974) was carried out based on the computed stator pressure distribution (Fig. V–6b) and on the wake–mixing analysis of Stewart (1959). This analysis gave a total pressure loss of 0.12 (vs. 0.14). The fact that the measured value was higher may be a result of several things. It was seen in the surface flow patterns (Figs. V–1 through V–4) and in the total pressure contour plot (Fig. V–8a) that the stator tip secondary flow had penetrated inward to the midspan region. This could also be seen in the secondary flow vector plot for this plane (Fig. V–8i). The gradient in stator loss from hub to tip could be seen in Fig. V–8c. This figure shows the hub–to–tip variation of the measured and computed mass–averaged total pressure aft of the first stator. It was interesting to note that the measured loss between 23% and 40% span agreed closely with the value of 0.12 predicted at midspan.

It was known from heat transfer measurements made on this stator (Blair et al., 1989a) that for the present low turbulence (0.5%) inlet conditions, the stator boundary layer was laminar up to the minimum pressure, where a rapid transition to turbulent flow occurred. A boundary layer analysis simulating this situation was carried out using the code by Edwards et al. (1981) and Carter et al. (1982), and the transitional mixing model by McDonald and Kreskovsky (1974). A free–stream turbulence of 10% was needed for the prediction to match the transitional behavior of the measured heat transfer data (Blair et al., 1989b, see Fig. 9a). This approach predicted a loss which was 30% smaller than the fully turbulent prediction (0.083 vs. 0.12). This suggested that there was no location in the wake of this stator where the flow (or the loss) was purely two dimensional.

The mass averaged total pressure loss ($\Delta PT/QUm$) at midspan was 0.26 for the computed first stator wake shown in Fig. V–8b. This large value was primarily due to the unsteadiness and three dimensionality of the flow and to the coarseness of the outer computational grid. A calculation was carried out for purely two–dimensional turbulent flow around the midspan section of the stator (Rai, 1989b). This calculation employed a much finer outer computational grid than the three–dimensional calculation (Rai, 1987). Using this refined outer grid, the mass averaged total pressure loss was predicted to be 0.13 (see Fig. V–8c). This was close to the value of 0.12 predicted by the turbulent boundary layer analysis.

Since the absolute total pressure in the flow entering the stator was at a CPTABS of 0.0, Fig. V–8c is a direct measure of the total pressure loss across the stator. Recall that the displacement and momentum thicknesses of the hub and tip inlet boundary layers were on the order of 1% of span (see Section III–1). As far as the spanwise trends were concerned, Fig. V–8c showed that all of the maxima and minima caused by the hub and tip secondary flows in the measured results were also present in the computation. The sensitivity of the computed results at midspan to grid refinement suggested that the quantitative agreement of the spanwise distribution could be improved significantly by grid refinement. It should be pointed out, however, that the that the spanwise integrated loss from the experimental results exceeded that of the computed results by roughly 15%. One possible reason for this difference might be that the calculation began one chord upstream of the stator with no end wall boundary layers.

Fig. V–8d

The measured and computed static pressure fields downstream of the stator are shown in Fig. V–8d. The two were very similar both in terms of distribution and level. The somewhat stronger circumferential variations in the computed results were due to the fact that the computed results were from a plane located closer to the stator trailing edge than the measured results (Fig. II–3). It might also be due to the coarseness of the computational grid.

Fig. V–8e

The excellent agreement between the measured and computed static pressure results could also be seen in the spanwise distribution of their circumferential area–averages (Fig. V–8e). The slight difference in the slopes may also be due to the different plane locations of the measured and computed results. This figure shows the high density of the computational grid near the end walls.

Fig. V–8f

The measured and computed results are presented in Fig. V–8f in terms of rotary total pressure.

$$\mathrm{PTROT} = \mathrm{PTREL} - \mathrm{QU}$$

In the rotating frame of reference this parameter is the kinematic equivalent of absolute total pressure in the stationary frame of reference. Just as a gradient in absolute total pressure is required to generate a secondary flow in the stationary frame of reference, a gradient in rotary (not relative) total pressure is required to generate a secondary flow in the rotating frame of reference (Hawthorne, 1974). The most disturbing feature in this otherwise excellent comparison was the circumferential gradients in the region between the wakes in the computed results. The measured results showed a very nearly axisymmetric distribution in this area. Admittedly, however, the computed gradients were rather weak.

Fig. V–8g

The rotary total pressure was circumferentially mass–averaged and the measured and computed results are presented in Fig. V–8g. The computed results had a slightly stronger gradient in the midspan region but, in general, the strong gradients were limited to the end wall regions. It could thus be anticipated that that there would be little or no gradient–driven secondary flow in the midspan region of the rotor. Parenthetically, the secondary flow due to the "relative eddy" is not gradient–driven. It is driven by the axial component of vorticity due to the rotating frame of reference (Dring and Joslyn, 1983). It is the relative eddy that gave rise to the the radial flow toward the tip on the rotor pressure surface (Figs. V–1 and V–4a).

Fig. V–8h

Since the comparison between the measured and computed static pressure fields was so good (Fig. V–8d and e), it was not surprising that the distributions of absolute flow speed were also good (Fig. V–8g). The circumferential gradients were stronger in the computed speed for the same reason they were in the computed static pressure (i.e., being closer to the stator trailing edge).

Fig. V–8i

The measured and computed secondary flow vectors downstream of the first stator are shown in Fig. V–8i. The radial component of each vector was proportional to the radial velocity component. The tangential component of each vector was proportional to the difference between the actual tangential velocity component and the tangential velocity component corresponding to the actual axial velocity component and the area averaged yaw angle at midspan. This corresponds to looking upstream at the velocity vectors from the direction of the averaged yaw angle at midspan.

In the measured results each vector represents a measurement location. It can be seen that the data density was highest in the airfoil wakes and near the end walls. In the computed results each vector represented a grid point location. It can be seen that the data density was highest near the end walls and that it was relatively sparse in the midspan region. Not all of the computational grid points have been shown in the figure. Several radial planes very close to the hub and tip end walls were deleted for the sake of clarity.

Both the measured and computed results showed the radial transport toward the hub in the stator wake due to the strong radial static pressure gradient at this plane (Figs. V–8d and e). This was the mechanism that moved the tip secondary flow away from the tip end wall and toward the hub (Fig. V–8a). It was the same mechanism that drove the hub secondary flow down toward the hub end wall (Fig. V–8a). The radial flow toward the tip in the computed results was not apparent in the measurements. The reason for this may be related to the larger axial gap in the experiment (50% vs. 15%).

The vortical motion in the hub secondary flow that can be seen in the measurements was not clearly evident in the computations. The primary reason for this was insufficient grid resolution in the radial direction. Two or three radial planes were insufficient to describe a vortical flow field of this type.

Fig. V–8j

The circumferentially area–averaged axial velocity component was plotted as a function of span in Fig. V–8j. Here again, the measured and computed results were seen to be in excellent agreement both in terms of level and trend.

Fig. V–8k

The spanwise distributions of the measured and computed absolute yaw angles aft of the first stator are shown in Fig. V–8k. These angles were based on the area–averaged velocity components, as required by through flow theory (Dring and Oates, 1989a and b). The agreement was generally excellent in both level and trend. Near the end walls the computed results indicated the expected trend toward over–turning. Similar over–turning could also be seen in the computed stator hub limiting stream lines (Fig. V–4c). The experimental flow visualization results also showed this trend toward over–turning on the hub end wall (Figs. V–1, 2, and 3). The measured flow angles near the tip, however, indicated a trend toward under–turning (toward axial). This difference may be a result of a problem with the instrumentation (due to wall interference effects). There was also the possibility that the entire trend toward over–turning occurred between 95% span and the tip end wall. This would not be inconsistent with the computed results.

Fig. V–8l

The spanwise distributions of the measured and computed relative yaw angles aft of the first stator are shown in Fig. V–8l. Here qualitative agreement was good in that all the maxima and minima of the prediction were present in the data. There was, however, a general degradation in the quantitative agreement. The problem of under–turning near the tip could also be seen here in the last two measured points.

This completes the discussion of the measured and computed aerodynamic results downstream of the first stator. Discussion will now turn to the aerodynamic data acquired downstream of the rotor. As mentioned above, since neither the calculation by Rai (1987) nor that by Madavan et al. (1989) were carried out with both the correct rotor aspect ratio and tip clearance they were not be compared with the measurements. It is anticipated, however, that such a calculation will be available in the near future (Rai, 1989a). Accordingly, the discussion below will focus purely on the measured results.

Fig. V–9a

The flow aft of the rotor is shown in terms of contours of rotary total pressure in Fig. V–9a. Here again, the traverse data was acquired over two rotor pitches. Since there were 22 first stator airfoils and 28 rotor airfoils the circumferential width of the figure was reduced by a factor of (11/14).

There was a large low total pressure region down stream of the rotor centered at about 60% span. This was due to the secondary flows occurring as the hub and tip end wall flows impacted the rotor suction surface and moved toward the midspan region (Fig. V–2). It was interesting to note that the hub and tip secondary flows had merged into a single low total pressure region. This region was located very close to the center of the tip secondary flow vortex (Fig. V–9g).

Somewhat similar results from a plane cascade experiment were reported by Moore and Ransmayr (1984) and by Moore and Adhye (1985). Their cascade experiment was carried out using an airfoil section which was nominally identical to the present rotor midspan section. Their cascade aspect ratio was 1.00 which is also very close to that of the present rotor (1.06). Their results showed that the low total pressure regions due to the hub and tip secondary flows moved away from the end walls, toward midspan, and that at a plane located 40% aft of the airfoil trailing edge they essentially merged into a single low total pressure region (Moore and Adhye [1985], Figs. 8 and 10). This was consistent with the present results which were taken 36% aft of the rotor trailing edge (Fig. II–3). The present results were also very similar to those presented by Madavan et al. (1989) in their Fig. 20b. Keep in mind that this similarity was achieved in spite of the difference in rotor tip clearance. The effect of the rotor tip leakage flow in the measurements could be seen by the regions of low rotary total pressure between 80% span and the tip. Recall that the rotor tip clearance was 1.0% span.

Fig. V–9b

The circumferentially mass–averaged rotary total pressure was plotted as a function of span in Fig. V–9b. The low total pressure regions due to the hub and tip secondary flows and the rotor tip leakage could be seen around 50% and 90% span respectively. The lifting of the secondary flows away from the hub caused a relatively high total pressure in this region.

An indication of the loss in rotary total pressure across the rotor could be seen by overlaying the inlet and exit rotary total pressure profiles (Figs. V–8g and V–9b). This showed a large loss across the entire rotor span, varying from about 0.4 at 15% span to 0.9 near midspan.

Figs. V–9c and d

The distribution of the static pressure aft of the rotor is shown in Fig. V–9c. The gradients here were very weak for two reasons. First, this traverse plane was 36% aft of the rotor trailing edge (Fig. II–3) and hence the circumferential gradients due to the rotor airfoil potential flow were weak. Second, because the absolute swirl aft of the rotor was low (≈35°), the radial static pressure gradient was weak. This could be seen in Fig. V–9d where the area–averaged static pressure is shown as a function of span. Note that the absolute swirl aft of the first stator was large (≈68°), resulting in a much stronger radial static pressure gradient (Fig. V–8e).

Fig. V–9e

The spanwise distribution of the circumferentially mass–averaged absolute total pressure is presented in Fig. V–9e. The main point to be seen here was that aside from a slight negative gradient there are no strong gradients in the midspan region and hence the secondary flow in the second stator should be dominated by the end wall flows.

Fig. V–9f

The radial/circumferential distribution of the relative flow speed aft of the rotor is illustrated in Fig. V–9f. The distribution here was similar to the rotary total pressure distribution (Fig. V–9a). The relative flow speed was also quite different from the first stator exit absolute flow speed distribution (Fig. V–9h) in that there were no strong spanwise static pressure gradients aft of the rotor as there were aft of the first stator. This was due to the low absolute swirl aft of the rotor (compare Fig. V–8e for the stator with Fig. V–9d for the rotor).

Fig. V–9g

The secondary flow velocity vectors in the flow aft of the rotor are shown in Fig. V–9g. This plot was generated in the same way as Fig. V–8i for the flow aft of the first stator. Here also the viewing angle was the averaged relative yaw angle at midspan. Two distinct counter–rotating vortices were clearly evident in the flow downstream of each rotor airfoil passage. These were the hub and tip secondary flow vortices. Their origins on the hub and tip end walls of the rotor passage could be seen in the rotor flow visualization (Fig. V–2). As mentioned above, the region of low rotary total pressure (Fig. V–9a) was centered over the tip secondary flow vortex at about 60% span.

Fig. V–9h

It is nearly impossible to see the tip leakage vortex in Fig. V–9g because the axis of this vortex was not aligned with the viewing direction (the averaged flow direction at midspan). Since this vortex was centered at about 90% span (Fig. V–9a) it could be seen more clearly when viewed from the averaged flow direction at this span location. Such a view is shown in Fig. V–9h where the tip leakage vortex is now much more apparent. There is about an 8° difference in these two viewing directions (Fig. V–9j). Note that the two secondary flow vortices also look quite different when viewed from this new direction.

Fig. V–9i

The spanwise distribution of the circumferentially area–averaged axial velocity component is plotted in Fig. V–9i. The under–turning in the region between the hub and tip secondary flow vortices caused a higher axial velocity in this region (near midspan). Conversely, the over–turning regions above and below the two secondary flow vortices have caused a lower axial velocity in these regions (near 10% and 80% span). The higher axial velocity due to the under–turning caused by the tip leakage could be seen near the tip.

Fig. V–9j

This whole issue of under– and over–turning becomes clearer when once considers the spanwise distribution of the rotor relative exit flow angle (Fig. V–9j). This plot of flow angle very closely resembles the plot of axial velocity above when it is inverted. Regions of high angle (over-turning) correspond to regions of low axial velocity, and vice–versa.

Fig. V–9k

The same observations made above for the relative flow angle are true also for the absolute flow angle (Fig. V–9k). The main difference is that the variations in absolute angle are much larger due to the subraction of wheel speed from the relative velocity vector.

This completes the discussion of the measured aerodynamic results downstream of the rotor. Discussion will now turn to the aerodynamic data acquired downstream of the second stage stator.

Fig. V–10a

The aerodynamic traverse results acquired downstream of the second stage stator are summarized in Fig. V–10. This traverse plane (Plane 4) was located 14% aft of the second stator trailing edge (Fig. II–3). Since there were 22 first stators and 28 second stators there was no practical way of quantifying the "average" passage (short of taking traverse data behind 14 adjacent second stator passages). The difficulty here could be seen in the absolute total pressure contours shown in Fig. V–10a. This data was taken over two first stator pitches (or 2.545 second stator pitches). The effects of the first stator could be seen most clearly in the non–periodic nature of the relatively weak gradients in the flow between the second stator wakes. The wakes themselves, however, were surprisingly periodic.

In spite of the fact that the second stator geometry was far more similar to the rotor than to the first stator, the second stator wake was far more similar to that of the first stator (compare Fig. V–10a with Figs. V–8a and V–9a). The main reason for this was that the flow aft of both stators had a much larger absolute swirl, and hence a much stronger radial static pressure gradient, than the flow aft of the rotor. This gradient drove the low total pressure fluid toward the hub. In the absence of this gradient the low total pressure fluid tended to accumulate near midspan. This was true both for the rotor (Fig. V–9a) and for a similar plane cascade (Moore and Ransmayr [1984] and by Moore and Adhye [1985]), both of which had aspect rations near unity.

Fig. V–10b

The circumferentially mass–averaged absolute total pressure aft of the second stator is presented as a function of span in Fig.V–10b. In an effort to deal with the issue of defining an "average" passage the results were averaged both over two first stator passages and over two second stator passages. The differences between the two were generally smaller than the symbol size. Only near the end walls did the differences approach 0.1. Accordingly, all of the data presented here were averaged over two second stator pitches.

The total pressure loss across the second stator could be seen by overlaying the inlet and exit total pressure profiles (Figs. V–9e and V–10b). The result was that there was a total pressure "loss" region near the hub and a "gain" region near the tip. The maximum changes in CPTABS were on the order of 0.2. This observation of a local "gain" in total pressure indicated that there must have been significant radial transport of the high and low total pressure fluid occurring between the stator inlet and exit (Planes 3 and 4). This is reinforced by the observations concerning the inlet flow angle for the second stator at 98% span (see the discussion of Fig. V–7).

Fig. V–10c

The static pressure field aft of the second stator is shown in Fig. V–10c. This distribution was very similar to that measured aft of the first stator (Fig. V–8d). Both had a strong spanwise gradient due to the large absolute swirl in the flow. Both also had relatively weak circumferential gradients due to the relatively large distance between the airfoils and the traverse planes (Fig. II–3).

Fig. V–10d

The spanwise gradient in the circumferentially area–averaged static pressure aft of the second stator (Fig. V–10d) was somewhat weaker than that behind the first stator (Fig. V–8e) due to its lower absolute swirl angle.

Figs. V–10e and f

The contours of rotary total pressure aft of the second stator were very similar to the absolute total pressure contours (Fig. V–10e). The absence of any strong radial gradients in the circumferentially mass–averaged rotary total pressure (Fig. V–10f) indicated that if there were a second stage rotor, it would not have and strong gradient–driven secondary flow in the midspan region.

Fig. V–10g

The contours of absolute flow speed aft of the second stator are illustrated in Fig. V–10g. Not only were the second stator wakes evident in the flow, but so also were the radial gradients in speed between the wakes due to the strong spanwise static pressure gradient.

Fig. V–10h

As can be seen in Fig. V–10h, there was a very strong secondary flow present. As with the first stator, there was strong flow from tip to hub in the wakes due to the radial static pressure gradient. Close to the hub (≈10% span) in each wake there was a strong vortical motion that could be a result of the hub secondary flow. There was also a relatively weak vortical motion of opposite sign in the regions between the wakes, around 30% span. This weaker vortex varied in radial and circumferential location from passage to passage. It might have been a vestige of the rotor secondary flow.

It appeared that there was under–turning near the hub and tip end walls. This was in the direction opposite to that expected for secondary flow (i.e., over–turning). Inspection of the spanwise distribution of the absolute flow angle at this plane (Fig. V–10j) suggested that the hub and tip secondary flows were in fact present, and in the expected direction, but that they were limited to regions very close to the end walls.

The conclusion reached from these results is that the secondary flows over the second stator were far more complex that either the first stator or rotor. The main reason for this was probably that the vorticity in the flow through the second stator passages was strongly influenced by both the upstream rotor and possibly even by the upstream stator.

Fig. V–10i

The spanwise distribution of the axial velocity component is shown as a function of span in Fig. V–10i. The under–turning observed above in the secondary flows near the hub and tip end walls had caused higher than average axial velocity in these regions. The over–turning due to secondary flow caused the axial velocity to begin to decrease very close to the end walls.

Fig. V–10j

These under– and over–turning patterns could be clearly seen in the spanwise distribution of the absolute flow angle presented in Fig. V–10j. The under–turning near the hub reached a maximum at about 10% span and that near the tip it reached a maximum at about 90% span. The over–turning due to secondary flow was evident between these maxima and the end walls where the flow tended toward tangential (90°).

Fig. V–10k

Finally, the spanwise variation of the relative flow angle aft of the second stator is presented in Fig. V–10k. It was similar to the absolute angle profile except that it was skewed and that the variations were larger due to subtracting wheel speed from the velocity vector.

This concludes the presentation of the measured and computed aerodynamic results. The intent in acquiring all this aerodynamic data was that it would provide: (1) a good basis for the assessment of computational methods, and (2) an explanation for the profile attenuation data that will be discussed in the following section.

V.2. Trace Gas Results

Fig. V–11

The inlet trace gas profile was generated by adjusting the CO2 flow rate to each of the five injector rings upstream of the test section (see Section III–2). It was documented at Plane 1, 97% upstream of the stator leading edge. This inlet documentation was carried out by making radial traverses at four circumferential locations. After considerable adjustment the results presented in Fig. V–11 were obtained. The range of concentrations at each radial location is indicative of the degree of axisymmetry achieved in the inlet flow. The non–axisymmetry in the inlet trace gas concentration parameter was ≈0.1. The measurement uncertainty in the NDIR readings (both here and in the data presented below) was much less than this. The average of the four inlet profile measurements was also shown. For clarity, it was shown separately in Fig. V–12.

Fig. V–12

The average inlet trace gas profile is shown in Fig. V–12. This profile served as a basis of comparison for the data measured at the various locations across the turbine. The dimensionless concentration parameter (see Section II–4) was based on this profile, 0.0 representing the minimum and 1.0 the maximum. The location of the maximum at 60% span corresponded to typical engine turbine inlet temperature profiles.

The radial area–average of the inlet trace gas profile at Plane 1 was 0.57. Since the flow velocity at this plane was axial and uniform (except for the hub and tip boundary layers) this average corresponded closely to the concentration that the flow in the turbine will approach as it becomes increasingly mixed out.

V.2.a. First Stator

Fig. V–13

The trace gas measurements made on the surface of the first stage stator are presented in Fig. V–13. These results were based on measurements made at 7 span locations and at 22 locations around the perimeter of the airfoil. The concentrations were rendered in terms of color contours to indicate the variation of the dimensionless concentration parameter between 0.0 (dark blue) and 1.0 (dark red). Generally speaking, the distributions of the high and low concentration fluid on the airfoil surfaces were what one might have expected based on the surface flow visualization (Figs. V–1 through V–3).

There was a high concentration region around midspan extending from the leading to the trailing edge of the airfoil. It was nearly uniform in spanwise extent on the pressure surface but on the suction surface there was a spanwise contraction due to the hub and tip secondary flows. The tip secondary flow was seen to be the stronger of the two due to the general tip–to–hub transport of the low momentum fluid. The hub end wall concentration was relatively uniform and at a very low level. This was also true for the tip end wall (not shown).

Fig. V–14

Concentration measurements made at the 7 span locations on the stator leading edge were compared with the average inlet profile in Fig. V–14. The only major change was an increase in concentration at the stator tip and a much smaller increase at the hub. These increases may have been due to the leading edge horseshoe vortex bringing higher concentration fluid out toward the end wall. The increases may also have been due partially to the non–axisymmetry of the inlet concentration. The increase at the tip, however, was too large to attribute to non–axisymmetry. The horseshoe vortex, therefore, could be an important mechanism for transporting hot core–flow fluid to the end walls.

Fig. V–15

The traverse data aft of the first stator is shown in Fig. V–15. As with the aerodynamic measurements, data was acquired over two first stator pitches. The periodicity in these results was consistent with an inlet non–axisymmetry of ≈0.1.

The dominant feature in these contours was the radial transport toward the hub that occurred in the stator wakes. This could be seen by comparing this concentration data with the stator exit total pressure data in Fig. V–8a and with the stator exit secondary flow data in Fig. V–8i. The strong flow toward the hub in the stator wake (Fig. V–8i) carried the high and low concentration fluid with it. There was also evidence that the secondary flow was driving low concentration fluid up the stator suction surface near the hub. Between the wakes the contours remained relatively axisymmetric. The main driver for temperature profile attenuation here was the radial transport due to the secondary flow and due to the airfoil wake.

Fig. V–16

The concentration data aft of the first stator was circumferentially area–averaged and compared with the inlet profile in Fig. V–16. The most noticeable change across the stator (between Planes 1 and 2) was the reduction in the maximum (from 1.0 to under 0.9). There was also evidence of transport of high concentration fluid down onto the end walls.

Fig. V–17

Another type of measurement aft of the first stator was obtained using the rotor leading edge rake. This rake was mounted on the rotor hub, at the leading edge plane. This plane was 50% aft of the stator trailing edge, compared to the Plane 2 traverse location, 17% aft (see Fig. II–3). The rotor rake results were compared with the stator exit traverse results and with the inlet profile in Fig. V–17.

A note of caution should be made about the concentration data acquired in the rotating frame of reference. The rotating frame results represent the circumferential average of the spatially non–axisymmetric inlet profile. This needs to be kept in mind when comparing them with data taken in the absolute frame.

With this caution in mind, it appeared that there had been an additional reduction in the maximum concentration near midspan and additional transport of high concentration fluid onto the end walls, especially at the tip. Recall that the traverse data was acquired 17% aft of the stator and that the rake data was acquired 50% aft.

V.2.b. Rotor

Fig. V–18

The trace gas measurements made on the surface of the rotor are presented in Fig. V–18. These results were based on measurements made at 7 span locations and at 22 locations around the perimeter of the airfoil. The concentrations have been rendered in terms of color contours to indicate the variation of the dimensionless concentration parameter between 0.0 (dark blue) and 1.0 (dark red). Generally speaking, the distributions of the high and low concentration fluid on the airfoil surfaces were what one might have expected based on the surface flow visualization (Figs. V–1 through V–3).

Generally speaking, the three–dimensional flow mechanisms were much stronger on the rotor than on the first stator (Fig. V–18 vs. V–13). This could be seen on both the suction and pressure surfaces. The suction surface was strongly influenced by the hub and tip secondary flows. They prevented the high concentration fluid (red) from reaching the trailing edge by driving the lower concentration fluid (turquoise, green and yellow) from the end walls out onto the rotor suction surface. The relatively high concentration region at the tip (the yellow along the aft portion of the suction surface) was attributed to the leakage flow through the rotor tip clearance.

Strong radial transport was present on the pressure surface due to the "relative eddy" (Dring and Joslyn, 1983). This inviscid mechanism was strictly associated with the rotating frame of reference. Its primary effect was to transport the high concentration fluid that entered the rotor passage at midspan outward toward the tip along the pressure surface. This was felt to be the source of the relatively high concentration (yellow) tip leakage fluid on the suction surface near the tip. This fluid had been transported radially out toward the tip along the pressure surface. It was then convected through the rotor tip clearance gap by the strong pressure gradient there. The conclusion here was that the temperature of the flow leaking over a rotor tip may not be the relatively cool fluid that enters the rotor passage near the tip, but rather the much hotter fluid that enters the passage in the midspan region. This is probably one of the reasons why rotor tip durability has frequently been a problem throughout the industry.

As on the first stator hub, the concentration distribution on the rotor hub was very uniform and at a relatively low level.

Fig. V–19

The concentration profile from the leading edge measurements made at the seven spanwise locations on the rotor airfoil were compared with the rotor leading edge rake data and with the turbine inlet profile in Fig. V–19. These results continue to show a reduction of the maximum concentration and an increase near the end walls. The mechanisms contributing to this included the radial flow in the stator wake and in its secondary flow, and also possible horseshoe vortices on the rotor leading edge.

Fig. V–20

The traverse data taken in the rotating frame of reference at Plane 3, 36% aft of the rotor, are presented in Fig. V–20. These results were acquired over two rotor pitches. All non–axisymmetry at the rotor inlet was averaged out by the rotor motion. Accordingly, the profile redistribution at this plane was due to the rotor secondary flow (Fig. V–9g). The maximum concentration had been reduced from about 0.85 at the rotor leading edge rake to about 0.7 at the traverse plane. There was a high degree of periodicity in the results due to the rotor averaging out inlet non–axisymmetries. The fact that these contours were driven by secondary flow can be seen by over laying Figs. V–20 and V–9g.

Fig. V–21

The traverse data taken in the stationary frame of reference at Plane 3, 36% aft of the rotor, are presented in Fig. V–21. These results were acquired over two first stage stator pitches. It was evident from the periodic variations in these results that the distortions introduced by the first stator were being convected through the rotor. Unlike the rotating frame results, these results also contained the influence of the non–axisymmetries in the turbine inlet concentration. It is noteworthy that these distortions existed aft of the first stage. This suggested that it might be possible to reduce the second stator heat load by setting the second stator airfoil count equal to that of the first stator and by locating the airfoils in the relatively cool parts of the flow.

It was interesting to note that the maximum concentration in both the rotating and stationary frame traverses was somewhat above 0.7. This indicated that the temporal and spatial variations in both frames of reference are of the same magnitude (max – min. ≈0.2).

Fig. V–22

The absolute and rotating frame traverse results aft of the rotor (Plane 3) were circumferentially averaged and plotted as functions of span along with the turbine inlet profile. Ideally, these two rotor exit profiles should be the same. The rotating frame results did, in fact, represent a true circumferential average. The absolute frame results were affected by the non–axisymmetries at the turbine inlet. As pointed out above, the difference was typically less than 0.1.

Fig. V–23

Upon comparing the rotor inlet rake results (Fig. V–19) with the rotor exit traverse results (Fig. V–22) as to the trace gas concentration in the tip region it could be seen that there was a large increase from the rotor inlet to the rotor exit. The rotor inlet rake indicated a concentration near the tip of about 0.35. The rotor exit traverses in both the absolute and rotating frames indicated a tip concentration of about 0.55. These results, along with data acquired on the stationary rotor tip shroud between the rotor leading and trailing edges, are shown in Fig. V–23. A general increase in the concentration at the tip could be seen from the rotor leading edge to the rotor exit traverse plane (36% aft). This increase was due to the transport toward the tip of high concentration fluid in the midspan region. This transport was due to both the relative eddy and the rotor tip secondary flow vortex.

The shroud results plotted in Fig. V–23 between the rotor leading and trailing edges were the averages of seven measurements distributed over one first stator pitch at each axial location. The "Max" and "Min" lines represent the envelope of these results. The width of this band was due partially to the non–axisymmetry of the concentration in the inlet flow and partially to the non–axisymmetries caused by the first stator.

V.2.c. Second Stator

Fig. V–24

The trace gas measurements made on the surface of the second stage stator are presented in Fig. V–24. These results were based on measurements made at 7 span locations and at 22 locations around the perimeter of the airfoil. The concentrations were rendered in terms of color contours to indicate the variation of the dimensionless concentration parameter between 0.0 (dark blue) and 1.0 (dark red). Generally speaking, the distributions of the high and low concentration fluid on the airfoil surfaces were what one might have expected based on the surface flow visualization (Figs. V–1 through V–3).

The fact that the mixing across the rotor was strong was evident by the washed out appearance of the color contours on the second stator. The flow has been driven to approach the average concentration of 0.57. This corresponds to the green side of the yellow contour.

As on the first stator, the distribution on the second stator pressure surface was relatively uniform from the leading edge to the trailing edge. Both the suction and pressure surfaces no longer have distributions which are symmetric about midspan (as on the first stator) but rather they had an almost linear gradient from lower concentrations at the hub to higher concentrations at the tip. This was a result of the radial redistribution through the rotor passage due to the relative eddy (rotation of the Bernoulli surfaces).

As on the first stator and rotor hubs, the concentration distribution on the second stator hub was very uniform and at a relatively low level. The same was true for the tip end wall (not shown).

The conclusion reached here was that the radial redistribution occurring in the rotor transported the higher concentration fluid out toward the second stator tip. This suggests that the high heat load conditions on second stators will be nearer the tip, rather than at midspan. Parenthetically, the relative eddy is an inviscid mechanism (Dring and Joslyn, 1983). One would expect that it would be predicted relatively accurately with the three–dimensional Euler calculations that are becoming increasingly common in the industry.

Fig. V–25

The concentration profile from the leading edge measurements made at the seven spanwise locations on the second stator airfoil were compared with the circumferentially averaged rotor exit traverse data (acquired in the rotating frame) and with the turbine inlet profile in Fig. V–25. The attenuation of the concentration profile has continued to the point that at this plane it was nearly linear from hub to tip. The level was probably high (relative to the rotating frame data) due to the non–axisymmetries in the inlet concentration.

Fig. V–26

The results of the traverse data taken at Plane 4, 14% aft of the second stator, are presented in Fig. V–26. The most striking feature here was that the concentration distribution was nearly axisymmetric and that the hub–to–tip gradient was very weak. The data here was acquired over two first stator pitches, however, because of the axisymmetry, it didn't matter much whether it was averaged across the pitch of the first or second stator.

Fig. V–27

The second stator exit traverse data was circumferentially averaged over the second stator pitch and it was compared with the second stator inlet profile (measured in the rotating frame) and with the turbine inlet profile in Fig. V–27. There was a continued mixing toward a uniform condition. The changes were mainly near the hub. The issue of inlet non–axisymmetry, however, complicates this comparison.

Fig. V–28

As a summary of the profile attenuation process across the three rows of turbine airfoils is given in Fig. V–28. Four profiles were presented: (1) the averaged inlet profile, (2) the rotor leading edge rake profile, (3) the circumferential average of the rotor exit traverse data acquired in the rotating frame of reference, and (4) the circumferential average of the stator exit traverse data.

Fig. V–29

The airfoil and hub end wall concentration distributions were combined into a single illustration, with the correct axial spacings, in Fig. V–29. This figure, along with Fig. V–28 provided a clear picture of the profile attenuation process across the three airfoil rows in the turbine.

The salient features of the trace gas concentration data were (1) the reduction in the profile maximum, (2) the increase in the hub and tip minima, and (3) the strong impact of the rotor in the profile attenuation process. Another important (and expected) feature of these results was that both from above and from below the local concentration was approaching the inlet area–average value of 0.57.

VI. CONCLUSIONS

The objective of this program was to examine the three–dimensional nature of the flow in a turbine with particular focus on the mechanisms affecting the mixing and attenuation of an inlet temperature profile.

The present program has advanced the state–of–the–art by providing: (1) an exhaustive aerodynamic data base for the three–dimensional flow in a large scale axial turbine, (2) an exhaustive data base documenting the mixing of a simulated combustor exit temperature profile as it passed through the turbine, and (3) an assessment of a state–of–the–art three–dimensional, time accurate, Navier–Stokes prediction of the flow in the turbine stage.

Specific observations and conclusions are as follows.

Aerodynamics Measurements

- Surface flow visualization indicated that hub and tip secondary flows were the main cause of three dimensionality in the stators (Figs. V–1 through V–3). Traverse results aft of the stators showed that radial transport in the wakes was also a strong contributor (Figs. V–8i and V–10h).
- Surface flow visualization indicated that hub and tip secondary flows, as well as the relative eddy and tip leakage, were the main causes of three dimensionality for the rotor (Figs. V–1 through V–2). Traverse results aft of the rotor showed that radial transport in the wakes was relatively weak due to the low level of absolute swirl (Fig. V–9g).
- The pressure distributions on the first stator were only weakly influenced by the three dimensionality of the flow (Fig. V–6).
- The pressure distributions on the rotor were strongly influenced by the three dimensionality of the flow, at the hub due to secondary flow and at the tip due to leakage flow through the clearance gap (Fig. V–6).
- The second stator pressure distribution was significantly affected by radial mixing immediately upstream of the airfoil. This mixing altered its incidence (Fig. V–7a).
- In spite of the fact that the high loss fluid aft of the rotor was swept up into a single region around midspan (as in a nonrotating cascade) (Fig. V–9a), the hub and tip secondary flow vortices were still clearly present (Fig. V–9g).
- In spite of the fact that the second stator airfoil is more similar to the rotor airfoil, its wake is more similar to that of the first stator because of its high exit swirl (Figs. V–8a and V–10a versus V–9a).

- The three dimensionality of the flow over the second stator is complicated by the presence of the upstream rotor (and possible by the upstream stator) (Fig. V–10h).

Trace Gas Profile Attenuation Measurements

- The trace gas technique gave an excellent simulation of temperature in so far as the profile attenuation process was concerned. Adiabatic boundary conditions were observed exactly and measurements on the airfoil and in the flow could be made with very high accuracy.

- The horseshoe vortex was a major contributor in bringing hot core flow fluid down onto the hub and tip end walls (Figs. V–14 and V–19).

- The major source of radial mixing due to the first stator was the radial flow in its wake (Fig. V–15).

- Radial mixing continued to occur in the axial gap between the first stator and the rotor (Fig. V–17).

- Radial mixing in the rotor was dominated by the hub and tip secondary flows, the relative eddy, and the tip leakage flow (Figs. V–18 and V–19).

- In the flow incident on the second stator the temporal variations (due to the rotor) and the circumferential spatial variations (due to the first stator) were very close in magnitude (Figs. V–20 and V–21).

- The circumferential variations in trace gas concentration in the flow entering the second stator (Fig. V–21) suggested that it might be possible to reduce the second stator heat load by setting the second stator airfoil count equal to that of the first stator and by locating the airfoils in the relatively cool parts of the flow.

- The effect of the relative eddy in the rotor passage was to preferentially drive high concentration (hot) fluid toward the tip (Fig. V–22) and this was felt by the second stator (Fig. V–24).

- The radial mixing in the flow over the rotor caused a monotonic increase in the trace gas concentration along the stationary rotor tip shroud (Fig. V–23).

- The concentration gradients in the flow aft of the second stator were very weak (Fig. V–26).

- The profile attenuation process was nearly complete aft of the second stator and although all three airfoils played powerful roles, the rotor was the strongest (Fig. V–28).

Computations (Rai, 1987)

- All of the three dimensionality seen in the surface flow visualization was also evident in the computed surface stream lines (Fig. V–4).
- Downstream of the first stator the computation gave an excellent prediction of most of the flow features. It successfully predicted all the qualitative features of the flow and many of the quantitative features (Fig. V–8).
- The computation predicted the stator exit flow with sufficient accuracy that the relative total pressure of the flow over the rotor was very close to the measured value (Figs. V–6 and V–8g).
- The computation gave a good prediction of the stator and rotor pressure distributions, in spite of the differences in axial gap and rotor aspect ratio (Fig. V–6).
- The computed secondary flows on the rotor (surface streamlines) were more severe than those measured due to the low rotor aspect ratio used in the computation (Fig. V–4).

RECOMMENDATIONS

As a result of the work carried out in this program there are a number of recommendations with regard to future work that should be considered.

1. The effect of combustor generated–turbulence at the inlet of the turbine should be examined to quantify its impact on profile attenuation. Initially this was not believed to be an important parameter, however, recent work in axial compressors (Gallimore [1986], Wisler et al. [1987]) suggests that this may not be the case. A program should be carried out in which a highly turbulent flow, characteristic of that exiting a combustor, is entering the turbine. This would require an intensity in the vicinity of 10% and a length scale large enough for the turbulence to persist through the turbine.

It might be anticipated that this turbulence would not have a significant impact on the inviscid aspects of the flow (i.e., the airfoil pressure distributions). Turbulence would, however, be expected to have an impact on the viscous aspects of the aerodynamics (i.e., the wakes and secondary flows) and on the temperature profile attenuation.

2. Although the measured and preliminary computed results are in good agreement as to the general nature of the flow aft of the rotor (Fig. V–9a and Rai [1987], Fig. 28, and Madavan et al. [1989], Fig. 20), they are both very different from what one might have expected in the region close to the airfoil trailing edge based on cascade experience, i.e., two distinct low total pressure, high loss, regions. There are two secondary flow vortices present in the measured results (Fig. V–9g). These vortices were not apparent in the preliminary computed results (primarily due to the relatively coarse grid used). This fact, coupled with the large amount of mixing (profile attenuation) between the rotor inlet and exit (Fig. V–28), suggests that it would be beneficial to more thoroughly document the development of the rotor exit flow. The rotor exit data in the present work was acquired at Plane 3 which was 36% aft of the rotor trailing edge. Additional data at planes closer to the rotor trailing edge would add a great deal to the picture. These additional planes of data would also be of value for more in–depth computational assessment.

ACKNOWLEDGMENTS

The authors owe a debt of gratitude to a number of talented, patient, and committed people for the success of this program. Jerry Jaminet provided the software for the trace gas measurements and made many on–line modifications to keep the program moving. Bill Tierney breathed life back into a traverse system that had been dormant and he kept it working faithfully. Ray Valliere acquired most of the data and on numerous occasions he demonstrated his formidable trouble–shooting skills. Finally, Lisa Vaughn and Diane Rodimon spent many long weeks reducing the data and generating the figures in this report. We are privileged to have each one of these people as a coworker.

The authors also need to acknowledge a special debt of gratitude to Dr. Man Mohan Rai and his co–workers at the NASA Ames Research Center. We are indebted to them, not only for providing us with computational and graphical results, some of which are included in this report, but also for numerous discussions and collaborations over the years.

REFERENCES

(* These works utilize the UTRC/LSRR Turbine Model)

* Adamczyk, J. J., Celestina, M. L., Beach, T. A., and Barnett, M., 1989, "Simulation of 3–D Viscous Flow Within a Multi–Stage Turbine," to be presented at the 1989 ASME Gas Turbine Conference.

Adkins, G. G. Jr. and Smith, L. H. Jr., 1982, "Spanwise Mixing in Axial–Flow Turbomachines," ASME Journal of Engineering for Power, Vol. 104, 1982, pp. 97–110.

Baldwin, B. S. and Lomax, H., 1978, "Thin Layer Approximation and Algebraic Model for Separated Turbulent Flow," AIAA paper number AIAA–78–257.

* Blair, M. F., Dring, R. P., and Joslyn, H. D., 1989a, "The Effects of Turbulence and Stator/Rotor Interactions on Turbine Heat Transfer, Part – I, Design Operation Conditions," ASME paper number 88–GT–125, Trans. ASME, Journal of Turbomachinery, Vol. 111, No. 1, January 1989, pp. 87–96.

* Blair, M. F., Dring, R. P., and Joslyn, H. D., 1989b, "The Effects of Turbulence and Stator/Rotor Interactions on Turbine Heat Transfer, Part – II, Effects of Reynolds Number and Incidence," ASME paper number 88–GT–5, Trans. ASME, Journal of Turbomachinery, Vol. 111, No. 1, January 1989, pp. 97 – 103.

* Butler, T. P., Sharma, O. P., Joslyn, H. D., and Dring, R. P., 1986, "Redistribution of an Inlet Temperature Distortion in an Axial Flow Turbine Stage," AIAA paper number AIAA–86–1468, Journal of Propulsion and Power, Vol. 5, No. 1, Jan.–Feb., 1989, pp. 64–71.

Carter, J. E., Edwards, D. E., and Werle, M. J., 1982, "Coordinate Transformation for Laminar and Turbulent Boundary Layers," AIAA Journal, Vol. 20, No. 2, February 1982, pp. 282–284.

Caspar, J. R., Hobbs, D. E., and Davis, R. L., 1980, "Calculation of Two–Dimensional Potential Cascade Flow Using Finite Area Methods," AIAA Journal, Vol. 18, January 1980, pp. 103–109.

Cebeci, T., and Smith, A. M. O., 1974, "Analysis of Turbulent Boundary Layers," Academic Press.

* Dring, R. P., Blair, M. F., and Joslyn, H. D., 1980, "Experimental Investigation of Film Cooling on a Turbine Rotor Blade," Trans. ASME, Journal of Engineering for Power, Vol. 102, No. 1, January 1980, pp. 81–87.

* Dring, R. P., Blair, M. F., and Joslyn, H. D., 1987, "Experimental Investigation of Turbine Rotor Heat Transfer," NASA–MSFC, Contract NAS8–37351, September 1987.

* Dring, R. P., Blair, M. F., Joslyn, H. D., Power, G. D., and Verdon, J. M., 1988, "The Effects of Inlet Turbulence and Rotor/Stator Interactions on the Aerodynamics and Heat Transfer of a Large–Scale Rotating Turbine Model," Vol. I, Final Report, NASA Contractor Report 4079, May 1988.

* Dring, R. P. and Joslyn, H. D., 1981, "Measurement of Turbine Rotor Blade Flows," Trans. ASME, Journal of Engineering for Power, Vol. 103, No. 2, April 1981, pp. 400–405.

* Dring, R. P., and Joslyn, H. D., 1983, "The Relative Eddy in Axial Turbine Rotor Passages," ASME paper number 83–GT–22.

* Dring, R. P., Joslyn, H. D., Hardin, L. W., and Wagner, J. H., 1981, "Turbine Rotor–Stator Interaction," Trans. ASME Journal of Engineering for Power, Vol. 106, No. 4, October 1981, pp. 729–742.

Dring, R.P. and Oates, G.C., 1989a, "Through Flow Theory for Nonaxisymmetric Turbomachinery Flow, Part I – Formulation," accepted for presentation at the 1989 ASME Gas Turbine Conference and for publication in the ASME Journal of Turbomachinery.

Dring, R.P. and Oates, G.C., 1989b, "Through Flow Theory for Nonaxisymmetric Turbomachinery Flow, Part II – Assessment," accepted for presentation at the 1989 ASME Gas Turbine Conference and for publication in the ASME Journal of Turbomachinery.

Eckert, E. R. G., and Goldstein, R. J., 1976, "Measurement Methods in Heat Transfer," 2nd Edition, Hemisphere Publishing Corp., Washington, D.C.

Edwards, D. E., Carter, J. E., and Werle, M. J., 1981, "Analysis of the Boundary Layer Equations Including a Coordinate Transformation — The ABLE Code," United Technologies Research Center report number UTRC–81–30.

Gallimore, S. J., and Cumpsty, N. A., 1986, "Spanwise Mixing in Multistage Axial Flow Compressors: Part 1 – Experimental Investigation," ASME Journal of Turbomachinery, Vol. 108, 1986, pp. 2–9.

Gallimore, S. J., 1986, "Spanwise Mixing in Multistage Axial Flow Compressors: Part 2 – Throughflow Calculations Including Mixing," ASME Journal of Turbomachinery, Vol. 108, 1986, pp. 10–16.

Harthorne, W. R., 1974, "Secondary Vorticity in Stratified Compressible Fluids in Rotating Systems," CUED/A–Turbo/TR 63, University of Cambridge, England.

Hung, C. M. and Buning, P. G., 1985, "Simulation of Blunt–Fin–Induced Shock–Wave and Turbulent–Layer Interaction," Journal of Fluid Mechanics, Vol. 154, pp. 163–185.

* Joslyn, H. D., and Dring, R. P., 1983, "Turbine Rotor Negative Incidence Stall," ASME paper number 83–GT–23.

* Joslyn, H. D., and Dring, R. P., 1988, "A Trace Gas Technique to Study Mixing in a Turbine Stage," ASME Journal of Turbomachinery, Vol. 110, No. 1, January 1988, pp. 38–43.

* Joslyn, H. D., Dring, R. P., and Sharma, O. P., 1983, "Unsteady Three–Dimensional Turbine Aerodynamics," Trans. ASME, Journal of Engineering for Power, Vol. 105, April 1983, pp. 322–331.

* Madavan, N. K., Rai, M. M., and Gavali, S., 1989, "Grid Refinement Studies of Turbine Rotor–Stator Interaction," AIAA paper number AIAA–89–0325.

McDonald, H., and Kreskovsky, J. P., 1974, "Effect of Free–Stream Turbulence on the Turbulent Boundary Layer," Internalional Journal of Heat and Mass Transfer, Vol. 17, pp . 705 – 716.

Moore, J., and Ransmayr, A., 1984, "Flow in a Turbine Cascade, Part I: Losses and Leading Edge Effects," Trans. ASME, Journal of Engineering for Gas Turbines and Power, Vol. 106, No. 2, April 1984, pp. 400–408.

Moore, J., and Adhye, R. Y., 1985, "Secondary Flows and Losses Downstream of a Turbine Cascade," Trans. ASME, Journal of Engineering for Gas Turbines and Power, Vol. 107, No. 4, October 1985, pp. 961 – 968.

Munk, M., and Prim, R. C., 1947, "On the Multiplicity of Steady Gas Flows Having the Same Streamline Pattern," Proceedings of the National Academy of Sciences, U. S., Vol. 33.

Pederson, D. R., Eckert, E. R. G., and Goldstein, R. J., 1977, "Film Cooling with Large Density Differences Between the Mainstream and the Secondary Fluid Measured by the Heat–Mass Transfer Analogy," Trans. ASME Journal of Heat Transfer, Vol. 99, November 1977.

* Rai, M. M., 1987, "Unsteady Three–Dimensional Navier–Stokes Simulations of Turbine Rotor–Stator Interaction Including Tip Effects," AIAA paper number AIAA–87–2058, presented at the Joint Propulsion Conference in San Diego, Cal., June 1987.

* Rai, M. M., and Dring, R. P., 1987, "Navier–Stokes Analysis of the Redistribution of Inlet Temperature Distortions in a Turbine," AIAA paper number AIAA–87–2146, to be published in the AIAA Journal of Propulsion and Power.

* Rai, M. M., and Madavan, N. K., 1988, "Multi–Airfoil Navier–Stokes Simulations of Turbine Rotor–Stator Interaction," AIAA paper number AIAA–88–0361, AIAA 26th Aerospace Sciences Meeting, Reno, Nevada, January 11–14, 1988.

Rai, M. M., 1989a, Private communication regarding a turbine stage calculation at NASA/Ames with the same rotor aspect ratio and tip clearance as in the experiment. January 12, 1989.

Rai, M. M., 1989b, Private communication regarding a two–dimensional calculation with a refined grid for the stator midspan section. January 18, 1989.

Reynolds, A. J., 1976, "The Variation of Turbulent Prandtl and Schmidt Numbers in Wakes and Jets," International Journal of Heat and Mass Transfer, Vol. 19, pp. 757–764.

* Roback, R. R., Dring, R. P., and Joslyn, H. D., 1988, "Turbine Heat Transfer Research, Hot Streaks and Phantom Cooling," AFWAL contract number F33615–88–C–2829.

* Sharma, O. P., Butler, T. L., Joslyn, H. D., and Dring, R. P., 1985, "Three–Dimensional Unsteady Flow in an Axial Flow Turbine," AIAA Journal of Propulsion and Power, Vol. 1, No. 1, Jan. – Feb. 1985, pp .29–38.

* Sharma, O. P., Renaud, E., Butler, T. L., Milsaps, K., Dring, R. P., and Joslyn, H. D., 1988, "Rotor–Stator Interaction in Multi–Stage Axial–Turbines," AIAA paper number AIAA–88–3013.

Stabe, R. G., Whitney, W. J., and Moffitt, T. P., 1984, "Performance of a High Work Low Aspect Ratio Turbine Tested with a Realistic Inlet Radial Temperature Profile," AIAA paper number AIAA 84–1161, June 1984.

Stewart, W. L., 1959, "Analysis of Two–Dimensional Flow Loss Charactersitics Downstream of Turbomachine Blade Rows in Terms of Basic Boundary Layer Characteristics," NACA–TN–3515, July 1959.

Wisler, D. C., Bauer, R. C., and Okiishi, T. H., 1987, "Secondary Flow, Turbulent Diffusion, and Mixing in Axial–Flow Compressors," Trans. ASME Journal of Turbomachinery, Vol. 109, No. 4, October 1987, pp. 455–482.

LIST OF SYMBOLS

Symbols

B_x	Airfoil axial chord
C	Absolute flow speed
C_t	Absolute tangential flow speed
C_x	Axial flow speed
(C_x/U_m)	Flow coefficient
CP	Pressure coefficient, $CP = (PTOA - P)/Q_{U_m}$
M	Mach number
PS	Static pressure
PTABS	Absolute total pressure
PTOA	Turbine inlet absolute total pressure
PTREL	Relative total pressure
PTROT	Rotary total pressure, $PTROT = PTREL - Q_U$
Q_U	Dynamic pressure based on U
Q_{U_m}	Dynamic pressure based on U_m
U	Rotor wheel speed
U_m	Rotor wheel speed at midspan
W	Relative flow speed
W_t	Relative tangential flow speed
x	Axial distance
y	Tangential distance
α	Absolute flow direction (from axial)
β	Relative flow direction (from axial)
ρ	Density
τ	Airfoil pitch

LIST OF SYMBOLS (Concluded)

Superscripts

–a, AA	Circumferential area average
–m, MA	Circumferential mass average

Subscripts

t	Tangential
x	Axial

LIST OF TABLES

LIST OF FIGURES

LIST OF FIGURES (Continued)

LIST OF FIGURES (Concluded)

TABLE 1a
AIRFOIL GEOMETRY

AIRFOIL: FIRST STATOR (HUB)
PITCH (ins.): 6.88865

	LEADING EDGE	TRAILING EDGE
RADIUS (ins.)	0.44485	0.10988
METAL ANGLE (degr.)	90.00395	22.44246
WEDGE ANGLE (degr.)	31.79000	6.85000

	X(ins.)	Y_L(ins.)	Y_U(ins.)
1	0.00000	5.98844	5.98844
2	0.05932	5.76650	6.21038
3	0.11864	5.68598	6.29089
4	0.17796	5.63254	6.34433
5	0.23728	5.59498	6.38189
6	0.29660	5.56902	6.40786
7	0.35592	5.55114	6.42556
8	0.41524	5.53364	6.44182
9	0.47456	5.51555	6.45743
10	0.53388	5.49688	6.47239
11	0.59320	5.47760	6.48668
12	0.74150	5.42681	6.51919
13	0.88980	5.37219	6.54678
14	1.03810	5.31366	6.56894
15	1.18640	5.25111	6.58508
16	1.33470	5.18440	6.59454
17	1.48300	5.11341	6.59667
18	1.63130	5.03800	6.59063
19	1.77960	4.95798	6.57559
20	1.92790	4.87318	6.55065
21	2.07620	4.78339	6.51481
22	2.22450	4.68839	6.46704
23	2.37280	4.58791	6.40627
24	2.52110	4.48160	6.33143
25	2.66940	4.36922	6.24143
26	2.81770	4.25033	6.13530
27	2.96600	4.12450	6.01210
28	3.11430	3.99119	5.87111
29	3.26260	3.84973	5.71175
30	3.41090	3.69938	5.53366
31	3.55920	3.53930	5.33677
32	3.70750	3.36863	5.12118
33	3.85580	3.18656	4.88723
34	4.00410	2.99229	4.63534
35	4.15240	2.78525	4.36603
36	4.30070	2.56517	4.07986
37	4.44900	2.33245	3.77749
38	4.59730	2.08792	3.45958
39	4.74560	1.83271	3.12684
40	4.89390	1.56797	2.78000
41	5.04220	1.29464	2.41981
42	5.19050	1.01365	2.04697
43	5.33880	0.72592	1.66229
44	5.39812	0.60905	1.50524
45	5.45744	0.49120	1.34645
46	5.51676	0.37243	1.18596
47	5.57608	0.25271	1.02380
48	5.63540	0.13213	0.86004
49	5.69472	0.01077	0.69471
50	5.75404	-0.08624	0.52783
51	5.81336	-0.10952	0.35947
52	5.87268	-0.09755	0.18966
53	5.93200	0.00001	0.00001

TABLE 1b
AIRFOIL GEOMETRY

AIRFOIL: FIRST STATOR (MIDSPAN)
PITCH (ins.): 7.71118

	LEADING EDGE	TRAILING EDGE
RADIUS (ins.)	0.44484	0.10987
METAL ANGLE (degr.)	90.00000	21.42000
WEDGE ANGLE (degr.)	31.80000	6.84000

	X(ins.)	Y_L(ins.)	Y_U(ins.)
1	0.00000	6.80766	6.80766
2	0.05932	6.44830	7.15365
3	0.11864	6.43405	7.17319
4	0.17796	6.41912	7.19210
5	0.23728	6.40354	7.21034
6	0.29660	6.38729	7.22791
7	0.35592	6.37035	7.24476
8	0.41524	6.35273	7.26089
9	0.47456	6.33441	7.27624
10	0.53388	6.31540	7.29080
11	0.59320	6.29568	7.30453
12	0.74150	6.24325	7.33502
13	0.88980	6.18623	7.35957
14	1.03810	6.12447	7.37758
15	1.18640	6.05781	7.38835
16	1.33470	5.98603	7.39114
17	1.48300	5.90896	7.38513
18	1.63130	5.82633	7.36940
19	1.77960	5.73787	7.34300
20	1.92790	5.64326	7.30490
21	2.07620	5.54212	7.25403
22	2.22450	5.43404	7.18927
23	2.37280	5.31852	7.10949
24	2.52110	5.19498	7.01363
25	2.66940	5.06273	6.90066
26	2.81770	4.92096	6.76967
27	2.96600	4.76873	6.61989
28	3.11430	4.60490	6.45078
29	3.26260	4.42825	6.26202
30	3.41090	4.23771	6.05354
31	3.55920	4.03254	5.82550
32	3.70750	3.81279	5.57826
33	3.85580	3.57948	5.31230
34	4.00410	3.33397	5.02816
35	4.15240	3.07798	4.72650
36	4.30070	2.81269	4.40803
37	4.44900	2.53937	4.07350
38	4.59730	2.25873	3.72369
39	4.74560	1.97172	3.35942
40	4.89390	1.67884	2.98147
41	5.04220	1.38062	2.59066
42	5.19050	1.07737	2.18773
43	5.33880	0.76951	1.77352
44	5.39812	0.64517	1.60482
45	5.45744	0.52020	1.43448
46	5.51676	0.39451	1.26252
47	5.57608	0.26816	1.08901
48	5.63540	0.14117	0.91397
49	5.69472	0.01364	0.73745
50	5.75404	-0.11456	0.55950
51	5.81336	-0.24329	0.38014
52	5.87268	-0.37263	0.19943
53	5.93200	0.00000	0.00000

TABLE 1c

AIRFOIL GEOMETRY

AIRFOIL: FIRST STATOR (TIP)
PITCH (ins.): 8.53371

	LEADING EDGE	TRAILING EDGE
RADIUS (ins.)	0.44487	0.10986
METAL ANGLE (degr.)	90.00401	20.25751
WEDGE ANGLE (degr.)	30.79000	6.79000

	X(ins.)	Y_L(ins.)	Y_U(ins.)
1	0.00000	7.57702	7.57702
2	0.05932	7.35507	7.79897
3	0.11864	7.27456	7.87949
4	0.17796	7.22112	7.93293
5	0.23728	7.18355	7.97049
6	0.29660	7.15759	7.99646
7	0.35592	7.13967	8.01409
8	0.41524	7.12193	8.02987
9	0.47456	7.10338	8.04449
10	0.53388	7.08402	8.05803
11	0.59320	7.06383	8.07044
12	0.74150	7.00967	8.09615
13	0.88980	6.95010	8.11406
14	1.03810	6.88487	8.12374
15	1.18640	6.81377	8.12465
16	1.33470	6.73650	8.11627
17	1.48300	6.65274	8.09803
18	1.63130	6.56207	8.06935
19	1.77960	6.46407	8.02955
20	1.92790	6.35817	7.97793
21	2.07620	6.24376	7.91381
22	2.22450	6.12004	7.83635
23	2.37280	5.98609	7.74477
24	2.52110	5.84072	7.63818
25	2.66940	5.68263	7.51566
26	2.81770	5.51023	7.37624
27	2.96600	5.32200	7.21892
28	3.11430	5.11693	7.04264
29	3.26260	4.89526	6.84631
30	3.41090	4.65850	6.62883
31	3.55920	4.40859	6.38910
32	3.70750	4.14741	6.12648
33	3.85580	3.87650	5.84072
34	4.00410	3.59714	5.53208
35	4.15240	3.31031	5.20125
36	4.30070	3.01688	4.84935
37	4.44900	2.71730	4.47775
38	4.59730	2.41223	4.08802
39	4.74560	2.10214	3.68183
40	4.89390	1.78726	3.26080
41	5.04220	1.46798	2.82654
42	5.19050	1.14458	2.38047
43	5.33880	0.81723	1.92403
44	5.39812	0.68529	1.73880
45	5.45744	0.55272	1.55219
46	5.51676	0.41958	1.36422
47	5.57608	0.28587	1.17502
48	5.63540	0.15177	0.98458
49	5.69472	0.01698	0.79299
50	5.75404	-0.08620	0.60033
51	5.81336	-0.10950	0.40661
52	5.87268	-0.09754	0.21192
53	5.93200	0.00001	0.00001

TABLE 2a

AIRFOIL GEOMETRY

AIRFOIL: FIRST ROTOR (HUB)
PITCH (ins.): 5.41251

	LEADING EDGE	TRAILING EDGE
RADIUS (ins.)	0.34867	0.19000
METAL ANGLE (degr.)	39.56323	25.97078
WEDGE ANGLE (degr.)	31.19000	5.31000

	X(ins.)	Y_L(ins.)	Y_U(ins.)
1	0.00000	2.86604	2.86604
2	0.06341	2.66555	3.08102
3	0.12682	2.59706	3.21151
4	0.19023	2.55545	3.33187
5	0.25364	2.53057	3.44343
6	0.31705	2.51881	3.54722
7	0.38046	2.51882	3.64406
8	0.44387	2.53062	3.73464
9	0.50728	2.55553	3.81950
10	0.57069	2.59558	3.89912
11	0.63410	2.63747	3.97388
12	0.79262	2.73147	4.14166
13	0.95115	2.81137	4.28528
14	1.10967	2.87832	4.40773
15	1.26820	2.93322	4.51126
16	1.42672	2.97676	4.59755
17	1.58525	3.00948	4.66791
18	1.74377	3.03180	4.72339
19	1.90230	3.04408	4.76477
20	2.06082	3.04653	4.79267
21	2.21935	3.03939	4.80757
22	2.37787	3.02278	4.80981
23	2.53640	2.99681	4.79963
24	2.69492	2.96157	4.77715
25	2.85345	2.91708	4.74242
26	3.01197	2.86339	4.69537
27	3.17050	2.80050	4.63584
28	3.32902	2.72831	4.56359
29	3.48755	2.64670	4.47823
30	3.64607	2.55547	4.37924
31	3.80460	2.45445	4.26599
32	3.96312	2.34348	4.13761
33	4.12165	2.22234	3.99304
34	4.28017	2.09081	3.83080
35	4.43870	1.94860	3.64903
36	4.59722	1.79535	3.44572
37	4.75575	1.63070	3.21968
38	4.91427	1.45405	2.97070
39	5.07280	1.26487	2.69996
40	5.23132	1.06245	2.40938
41	5.38985	0.84595	2.10143
42	5.54837	0.61435	1.77875
43	5.70690	0.36649	1.44378
44	5.77031	0.26245	1.30685
45	5.83372	0.15541	1.16841
46	5.89713	0.04543	1.02861
47	5.96054	-0.06777	0.88753
48	6.02395	-0.16117	0.74527
49	6.08736	-0.19892	0.60194
50	6.15077	-0.20989	0.45759
51	6.21418	-0.19908	0.31233
52	6.27759	-0.16158	0.16622
53	6.34100	-0.01989	-0.01989

TABLE 2b

AIRFOIL GEOMETRY

AIRFOIL: FIRST ROTOR (MIDSPAN)
PITCH (ins.): 6.05879

	LEADING EDGE	TRAILING EDGE
RADIUS (ins.)	0.34872	0.19000
METAL ANGLE (degr.)	42.18646	25.97093
WEDGE ANGLE (degr.)	31.24000	5.31000

	X(ins.)	Y_L(ins.)	Y_U(ins.)
1	0.00000	3.41970	3.41970
2	0.06341	3.21919	3.62774
3	0.12682	3.15069	3.74347
4	0.19023	3.10908	3.84906
5	0.25364	3.08419	3.94593
6	0.31705	3.07242	4.03518
7	0.38046	3.07243	4.11769
8	0.44387	3.08422	4.19414
9	0.50728	3.10912	4.26511
10	0.57069	3.14694	4.33106
11	0.63410	3.18401	4.39238
12	0.79262	3.26583	4.52752
13	0.95115	3.33349	4.63984
14	1.10967	3.38822	4.73220
15	1.26820	3.43094	4.80674
16	1.42672	3.46228	4.86506
17	1.58525	3.48271	4.90837
18	1.74377	3.49248	4.93760
19	1.90230	3.49176	4.95347
20	2.06082	3.48053	4.95652
21	2.21935	3.45868	4.94712
22	2.37787	3.42596	4.92555
23	2.53640	3.38201	4.89193
24	2.69492	3.32633	4.84632
25	2.85345	3.25830	4.78863
26	3.01197	3.17735	4.71868
27	3.17050	3.08283	4.63616
28	3.32902	2.97433	4.54063
29	3.48755	2.85162	4.43151
30	3.64607	2.71488	4.30799
31	3.80460	2.56463	4.16905
32	3.96312	2.40136	4.01334
33	4.12165	2.22577	3.83912
34	4.28017	2.03852	3.64406
35	4.43870	1.84022	3.42595
36	4.59722	1.63139	3.18387
37	4.75575	1.41252	2.91861
38	4.91427	1.18402	2.63221
39	5.07280	0.94623	2.32774
40	5.23132	0.69955	2.00832
41	5.38985	0.44403	1.67680
42	5.54837	0.18008	1.33571
43	5.70690	-0.09214	0.98699
44	5.77031	-0.20337	0.84573
45	5.83372	-0.31578	0.70359
46	5.89713	-0.42949	0.56065
47	5.96054	-0.54448	0.41698
48	6.02395	-0.63800	0.27261
49	6.08736	-0.67575	0.12765
50	6.15077	-0.68673	-0.01791
51	6.21418	-0.67591	-0.16397
52	6.27759	-0.63841	-0.31052
53	6.34100	-0.49672	-0.49672

TABLE 2c

AIRFOIL GEOMETRY

AIRFOIL: FIRST ROTOR (TIP)
PITCH (ins.): 6.70506

	LEADING EDGE	TRAILING EDGE
RADIUS (ins.)	0.34881	0.19000
METAL ANGLE (degr.)	46.66805	25.96767
WEDGE ANGLE (degr.)	31.26000	5.31000

	X(ins.)	Y_L(ins.)	Y_U(ins.)
1	0.00000	3.97348	3.97348
2	0.06341	3.77294	4.17548
3	0.12682	3.70443	4.27381
4	0.19023	3.66280	4.36353
5	0.25364	3.63790	4.44573
6	0.31705	3.62612	4.52127
7	0.38046	3.62611	4.59084
8	0.44387	3.63787	4.65499
9	0.50728	3.66275	4.71419
10	0.57069	3.69488	4.76883
11	0.63410	3.72462	4.81924
12	0.79262	3.78887	4.92848
13	0.95115	3.83974	5.01637
14	1.10967	3.87814	5.08539
15	1.26820	3.90472	5.13737
16	1.42672	3.91989	5.17369
17	1.58525	3.92388	5.19537
18	1.74377	3.91674	5.20321
19	1.90230	3.89838	5.19778
20	2.06082	3.86851	5.17950
21	2.21935	3.82665	5.14862
22	2.37787	3.77210	5.10529
23	2.53640	3.70385	5.04954
24	2.69492	3.62049	4.98122
25	2.85345	3.52015	4.90012
26	3.01197	3.40033	4.80585
27	3.17050	3.25903	4.69788
28	3.32902	3.09581	4.57543
29	3.48755	2.91352	4.43757
30	3.64607	2.71577	4.28296
31	3.80460	2.50562	4.10990
32	3.96312	2.28505	3.91608
33	4.12165	2.05587	3.69853
34	4.28017	1.81890	3.45544
35	4.43870	1.57520	3.18730
36	4.59722	1.32521	2.89675
37	4.75575	1.06966	2.58780
38	4.91427	0.80884	2.26420
39	5.07280	0.54319	1.92951
40	5.23132	0.27306	1.58629
41	5.38985	-0.00136	1.23664
42	5.54837	-0.27975	0.88207
43	5.70690	-0.56201	0.52368
44	5.77031	-0.67597	0.37945
45	5.83372	-0.79046	0.23478
46	5.89713	-0.90562	0.08974
47	5.96054	-1.02119	-0.05569
48	6.02395	-1.11481	-0.20147
49	6.08736	-1.15257	-0.34753
50	6.15077	-1.16355	-0.49387
51	6.21418	-1.15274	-0.64045
52	6.27759	-1.11524	-0.78728
53	6.34100	-0.97355	-0.97355

TABLE 3a

AIRFOIL GEOMETRY

AIRFOIL: SECOND STATOR (HUB)
PITCH (ins.): 5.41251

	LEADING EDGE	TRAILING EDGE
RADIUS (ins.)	0.34999	0.19000
METAL ANGLE (degr.)	29.91000	24.98619
WEDGE ANGLE (degr.)	41.01068	8.91000

	X(ins.)	Y_L(ins.)	Y_U(ins.)
1	0.00000	3.68263	3.68263
2	0.06452	3.48015	3.89472
3	0.12904	3.41120	4.01869
4	0.19356	3.36955	4.13494
5	0.25808	3.34493	4.24410
6	0.32260	3.33372	4.34672
7	0.38712	3.33462	4.44324
8	0.45164	3.34773	4.53408
9	0.51616	3.37461	4.61958
10	0.58068	3.41583	4.70006
11	0.64520	3.45739	4.77578
12	0.80650	3.55269	4.94580
13	0.96780	3.63560	5.09069
14	1.12910	3.70599	5.21287
15	1.29040	3.76376	5.31424
16	1.45170	3.80880	5.39634
17	1.61300	3.84106	5.46037
18	1.77430	3.86048	5.50735
19	1.93560	3.86704	5.53806
20	2.09690	3.86072	5.55317
21	2.25820	3.84153	5.55319
22	2.41950	3.80950	5.53852
23	2.58080	3.76468	5.50948
24	2.74210	3.70714	5.46629
25	2.90340	3.63698	5.40908
26	3.06470	3.55430	5.33790
27	3.22600	3.45921	5.25273
28	3.38730	3.35188	5.15348
29	3.54860	3.23245	5.03995
30	3.70990	3.10111	4.91189
31	3.87120	2.95802	4.76892
32	4.03250	2.80339	4.61058
33	4.19380	2.63745	4.43628
34	4.35510	2.46037	4.24527
35	4.51640	2.27244	4.03662
36	4.67770	2.07384	3.80928
37	4.83900	1.86483	3.56222
38	5.00030	1.64569	3.29479
39	5.16160	1.41663	3.00662
40	5.32290	1.17789	2.69784
41	5.48420	0.92975	2.36890
42	5.64550	0.67246	2.02068
43	5.80680	0.40629	1.65431
44	5.87132	0.29738	1.50296
45	5.93584	0.18710	1.34900
46	6.00036	0.07548	1.19252
47	6.06488	-0.03748	1.03361
48	6.12940	-0.13608	0.87238
49	6.19392	-0.17738	0.70890
50	6.25844	-0.18997	0.54327
51	6.32296	-0.17996	0.37560
52	6.38748	-0.14267	0.20595
53	6.45200	0.00000	0.00000

TABLE 3b

AIRFOIL GEOMETRY

AIRFOIL: SECOND STATOR (MIDSPAN)
PITCH (ins.): 6.05879

	LEADING EDGE	TRAILING EDGE
RADIUS (ins.)	0.34999	0.19000
METAL ANGLE (degr.)	45.66800	25.00000
WEDGE ANGLE (degr.)	27.50000	6.50000

	X(ins.)	Y_L(ins.)	Y_U(ins.)
1	0.00000	4.10291	4.10291
2	0.06452	3.47786	4.30650
3	0.12904	3.52885	4.40610
4	0.19356	3.57793	4.50013
5	0.25808	3.62510	4.58895
6	0.32260	3.67035	4.67285
7	0.38712	3.71368	4.75210
8	0.45164	3.75508	4.82695
9	0.51616	3.79454	4.89760
10	0.58068	3.83206	4.96425
11	0.64520	3.86762	5.02707
12	0.80650	3.94796	5.16834
13	0.96780	4.01599	5.28865
14	1.12910	4.07162	5.38963
15	1.29040	4.11482	5.47259
16	1.45170	4.14552	5.53859
17	1.61300	4.16371	5.58849
18	1.77430	4.16934	5.62296
19	1.93560	4.16244	5.64258
20	2.09690	4.14298	5.64778
21	2.25820	4.11101	5.63888
22	2.41950	4.06655	5.61615
23	2.58080	4.00965	5.57973
24	2.74210	3.94037	5.52972
25	2.90340	3.85879	5.46611
26	3.06470	3.76498	5.38882
27	3.22600	3.65906	5.29771
28	3.38730	3.54111	5.19255
29	3.54860	3.41127	5.07300
30	3.70990	3.26967	4.93863
31	3.87120	3.11644	4.78891
32	4.03250	2.95172	4.62316
33	4.19380	2.77568	4.44053
34	4.35510	2.58849	4.24001
35	4.51640	2.39030	4.02052
36	4.67770	2.18130	3.78134
37	4.83900	1.96166	3.52218
38	5.00030	1.73160	3.24330
39	5.16160	1.49128	2.94535
40	5.32290	1.24090	2.62941
41	5.48420	0.98064	2.29682
42	5.64550	0.71074	1.94914
43	5.80680	0.43141	1.58790
44	5.87132	0.31707	1.43996
45	5.93584	0.20126	1.29018
46	6.00036	0.08400	1.13867
47	6.06488	-0.03471	0.98552
48	6.12940	-0.15484	0.83080
49	6.19392	-0.27639	0.67459
50	6.25844	-0.39934	0.51699
51	6.32296	-0.52368	0.35805
52	6.38748	-0.64939	0.19786
53	6.45200	0.00000	0.00000

TABLE 3c
AIRFOIL GEOMETRY

AIRFOIL: SECOND STATOR (TIP)
PITCH (ins.): 6.70506

	LEADING EDGE	TRAILING EDGE
RADIUS (ins.)	0.35006	0.19000
METAL ANGLE (degr.)	50.49115	24.98778
WEDGE ANGLE (degr.)	25.12000	4.09000

	X(ins.)	Y_L(ins.)	Y_U(ins.)
1	0.00000	4.53429	4.53429
2	0.06452	4.33178	4.73679
3	0.12904	4.26282	4.81836
4	0.19356	4.22116	4.89463
5	0.25808	4.19652	4.96641
6	0.32260	4.18530	5.03396
7	0.38712	4.18619	5.09751
8	0.45164	4.19929	5.15728
9	0.51616	4.22602	5.21343
10	0.58068	4.25762	5.26613
11	0.64520	4.28729	5.31552
12	0.80650	4.35297	5.42538
13	0.96780	4.40647	5.51708
14	1.12910	4.44777	5.59199
15	1.29040	4.47683	5.65117
16	1.45170	4.49364	5.69551
17	1.61300	4.49819	5.72567
18	1.77430	4.49045	5.74219
19	1.93560	4.47047	5.74550
20	2.09690	4.43822	5.73590
21	2.25820	4.39375	5.71360
22	2.41950	4.33706	5.67874
23	2.58080	4.26823	5.63135
24	2.74210	4.18728	5.57140
25	2.90340	4.09426	5.49876
26	3.06470	3.98924	5.41323
27	3.22600	3.87229	5.31449
28	3.38730	3.74348	5.20215
29	3.54860	3.60289	5.07566
30	3.70990	3.45062	4.93435
31	3.87120	3.28675	4.77738
32	4.03250	3.11139	4.60366
33	4.19380	2.92465	4.41196
34	4.35510	2.72666	4.20118
35	4.51640	2.51749	3.97077
36	4.67770	2.29731	3.72077
37	4.83900	2.06620	3.45177
38	5.00030	1.82436	3.16495
39	5.16160	1.57187	2.86176
40	5.32290	1.30889	2.54389
41	5.48420	1.03553	2.21304
42	5.64550	0.75199	1.87091
43	5.80680	0.45841	1.51902
44	5.87132	0.33818	1.37585
45	5.93584	0.21639	1.23140
46	6.00036	0.09302	1.08577
47	6.06488	-0.03190	0.93902
48	6.12940	-0.13607	0.79122
49	6.19392	-0.17738	0.64244
50	6.25844	-0.18996	0.49272
51	6.32296	-0.17995	0.34214
52	6.38748	-0.14267	0.19073
53	6.45200	0.00000	0.00000

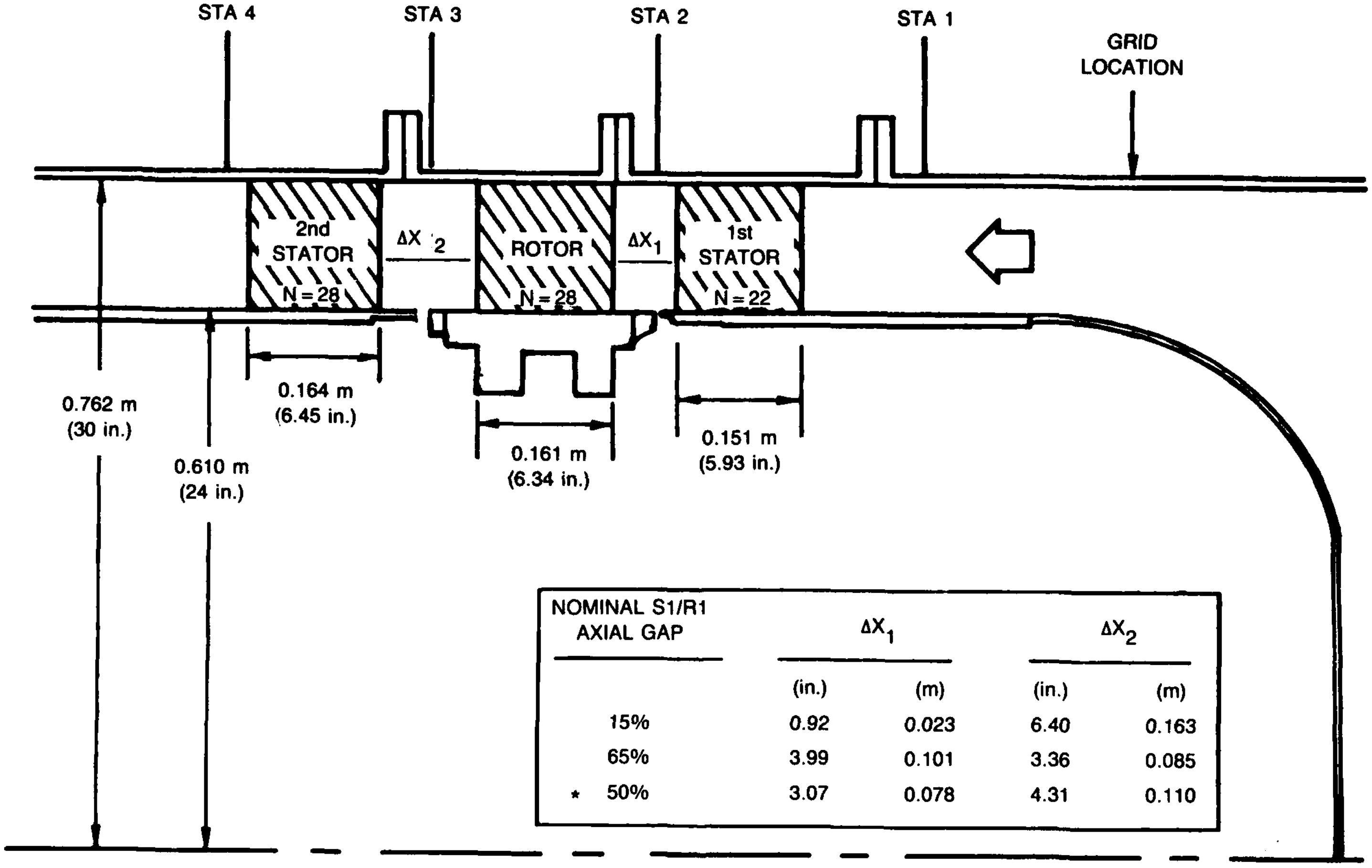

NOMINAL S1/R1 AXIAL GAP	ΔX_1		ΔX_2	
	(in.)	(m)	(in.)	(m)
15%	0.92	0.023	6.40	0.163
65%	3.99	0.101	3.36	0.085
* 50%	3.07	0.078	4.31	0.110

Fig. II-1 United Technologies Research Center Large Scale Rotating Rig (*Present Study)

86-11-38-1

(First Vane and Rotor Case Removed)

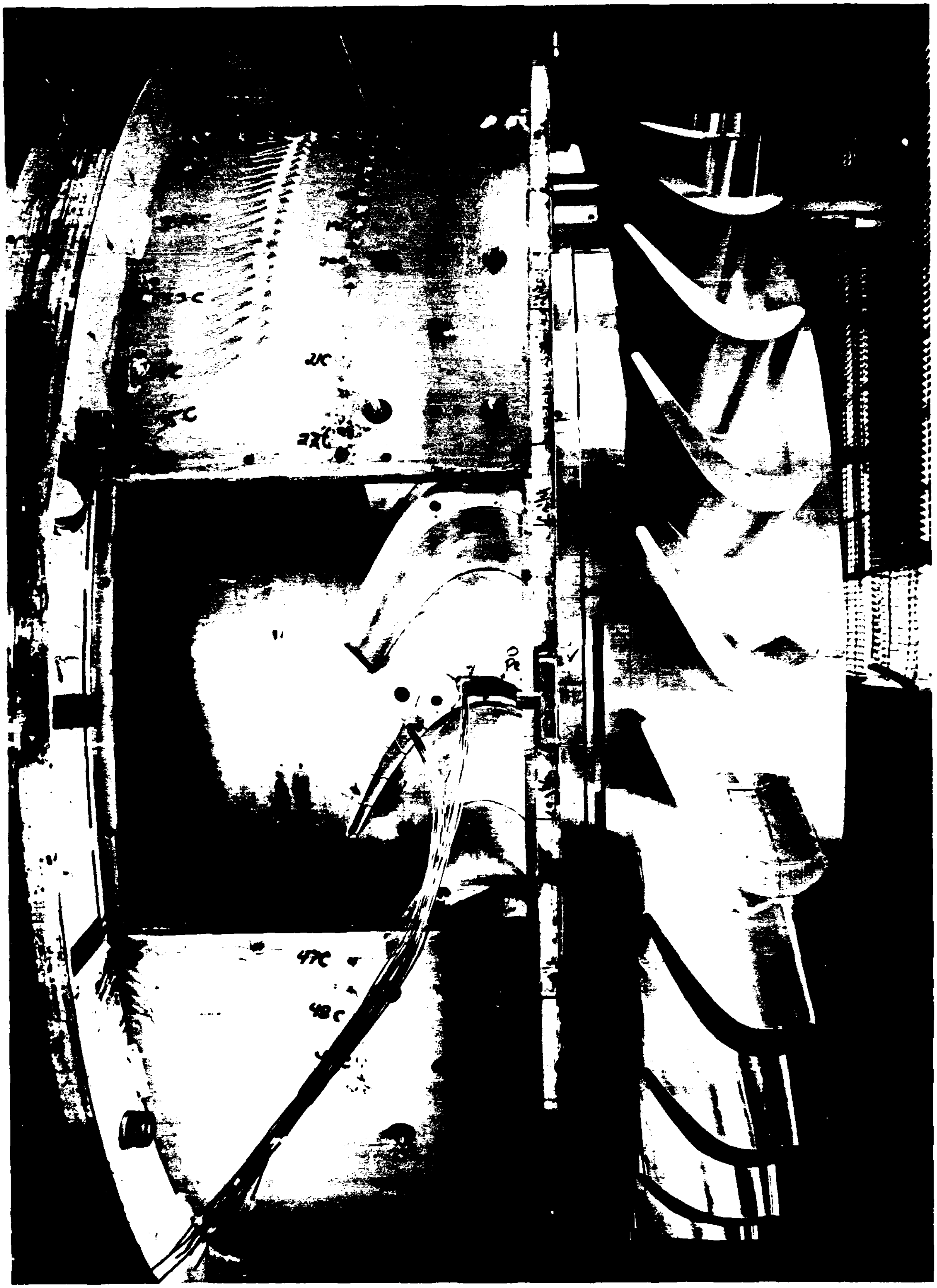

Fig. II–2 Large Scale Rotating Rig 1 1/2 Stage Turbine

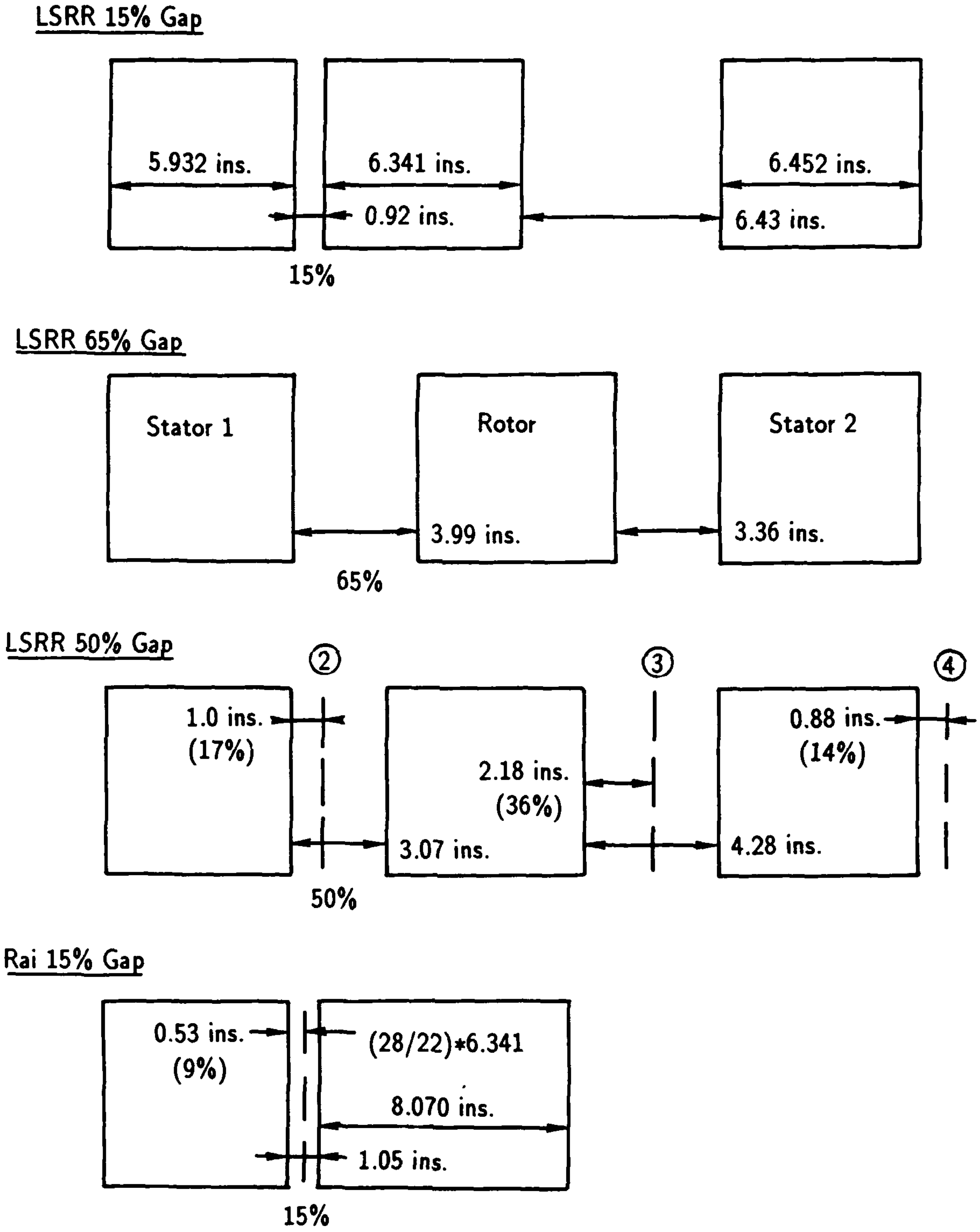

Fig. II–3 LSRR Turbine Configurations

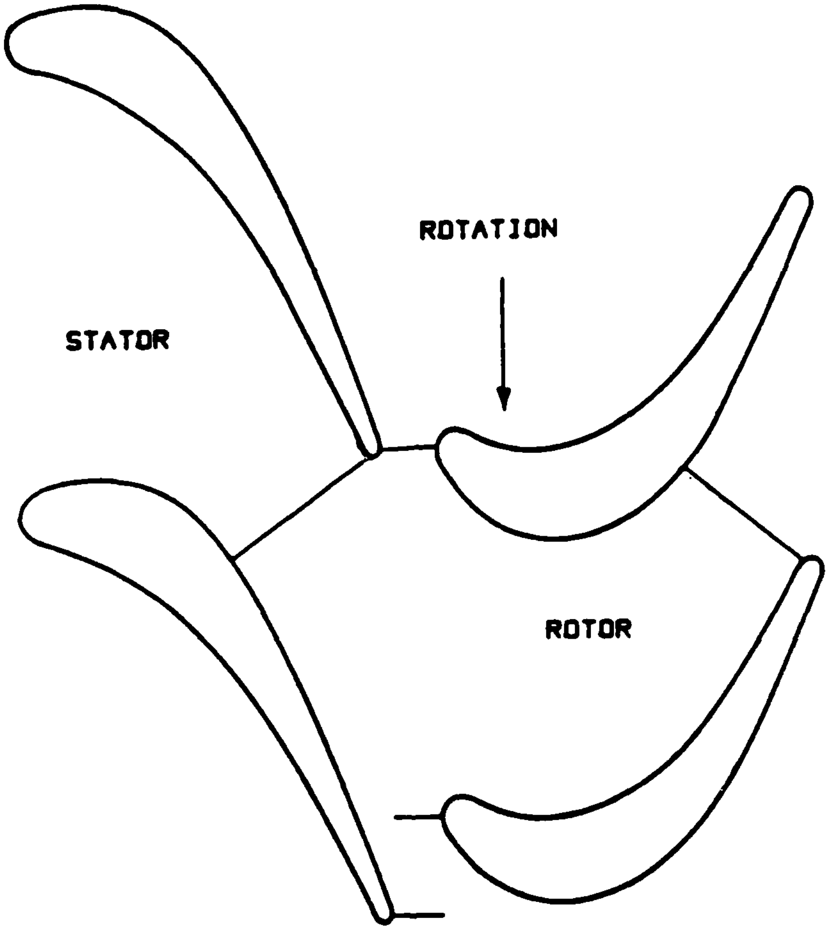

Fig. II–4 First Stator and Rotor at Midspan (15% Gap)

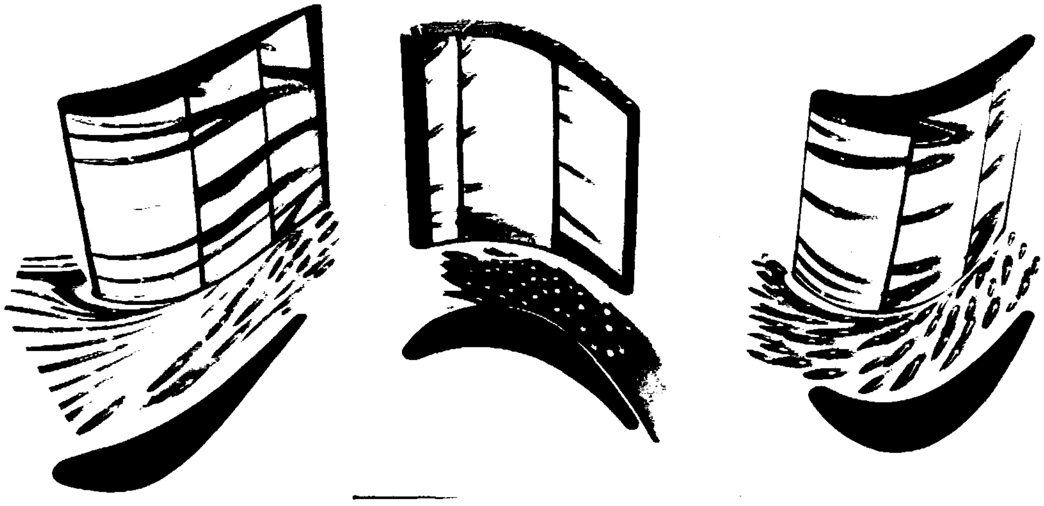

Fig. V–1 Experimental Surface Flow Visualization,
Stator Suction Surfaces and Rotor Pressure Surface

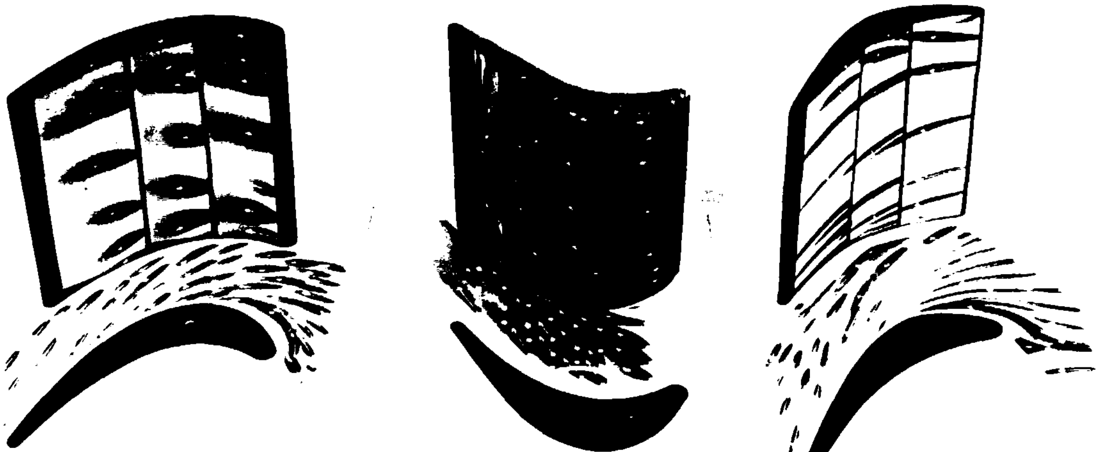

Fig. V–2 Experimental Surface Flow Visualization,
Stator Pressure Surfaces and Rotor Suction Surface

Fig. V–3 Experimental Surface Flow Visualization, Tip End Wall

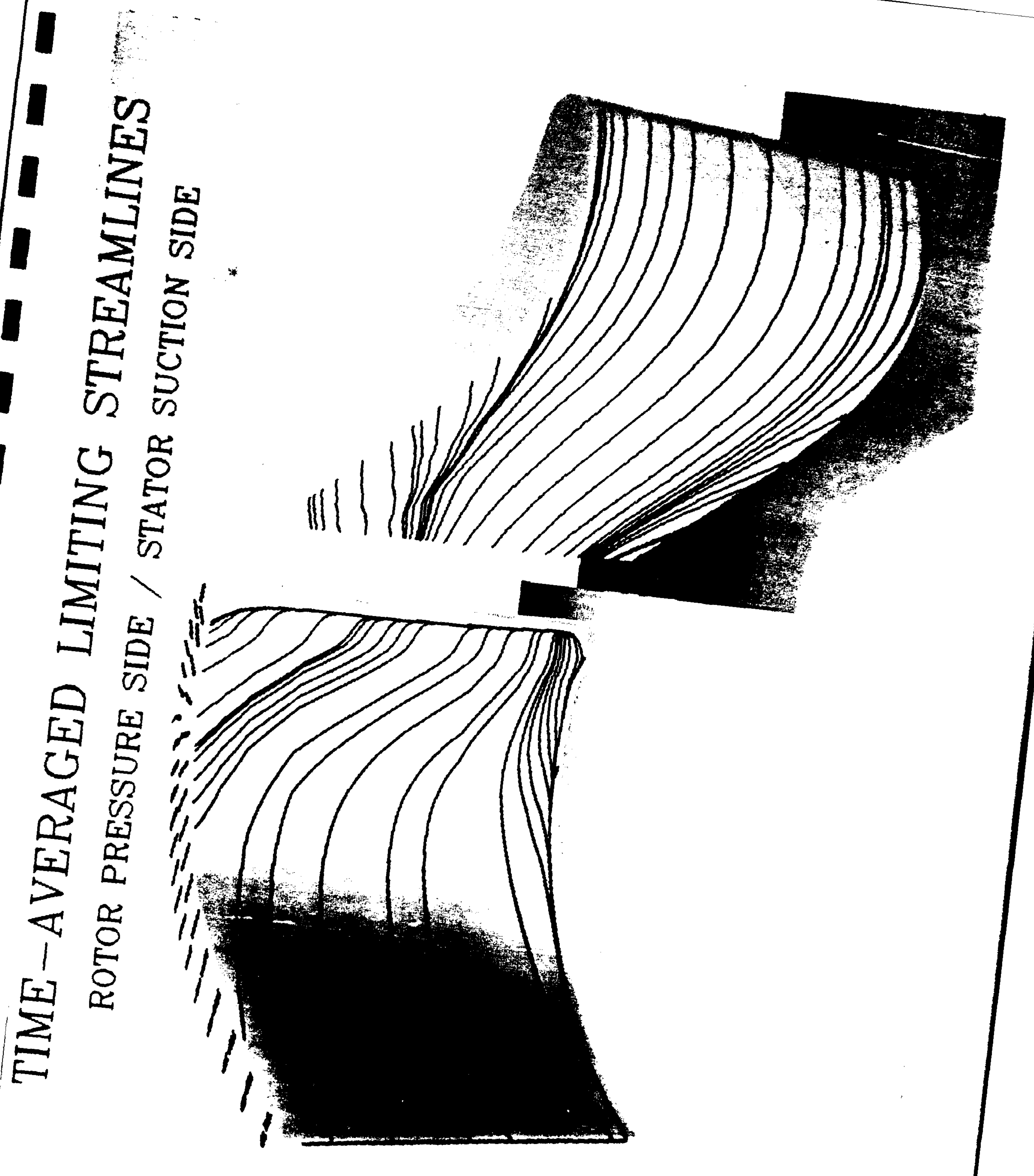

Fig. V–4a Computed First Stator and Rotor Surface Flow, Rotor Pressure Side and Stator Suction Side

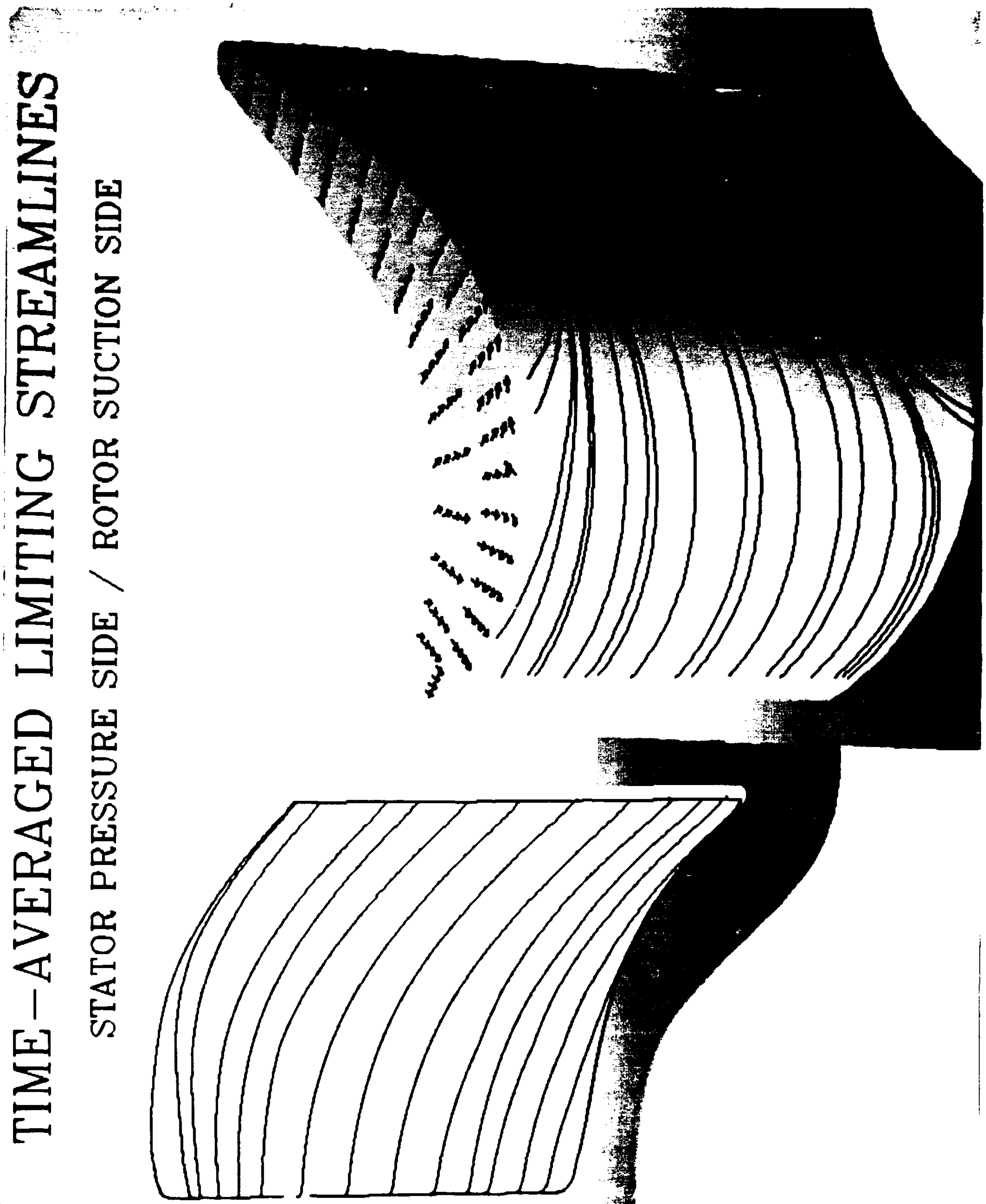

Fig. V–4b Computed First Stator and Rotor Surface Flow, Stator Pressure Side and Rotor Suction Side

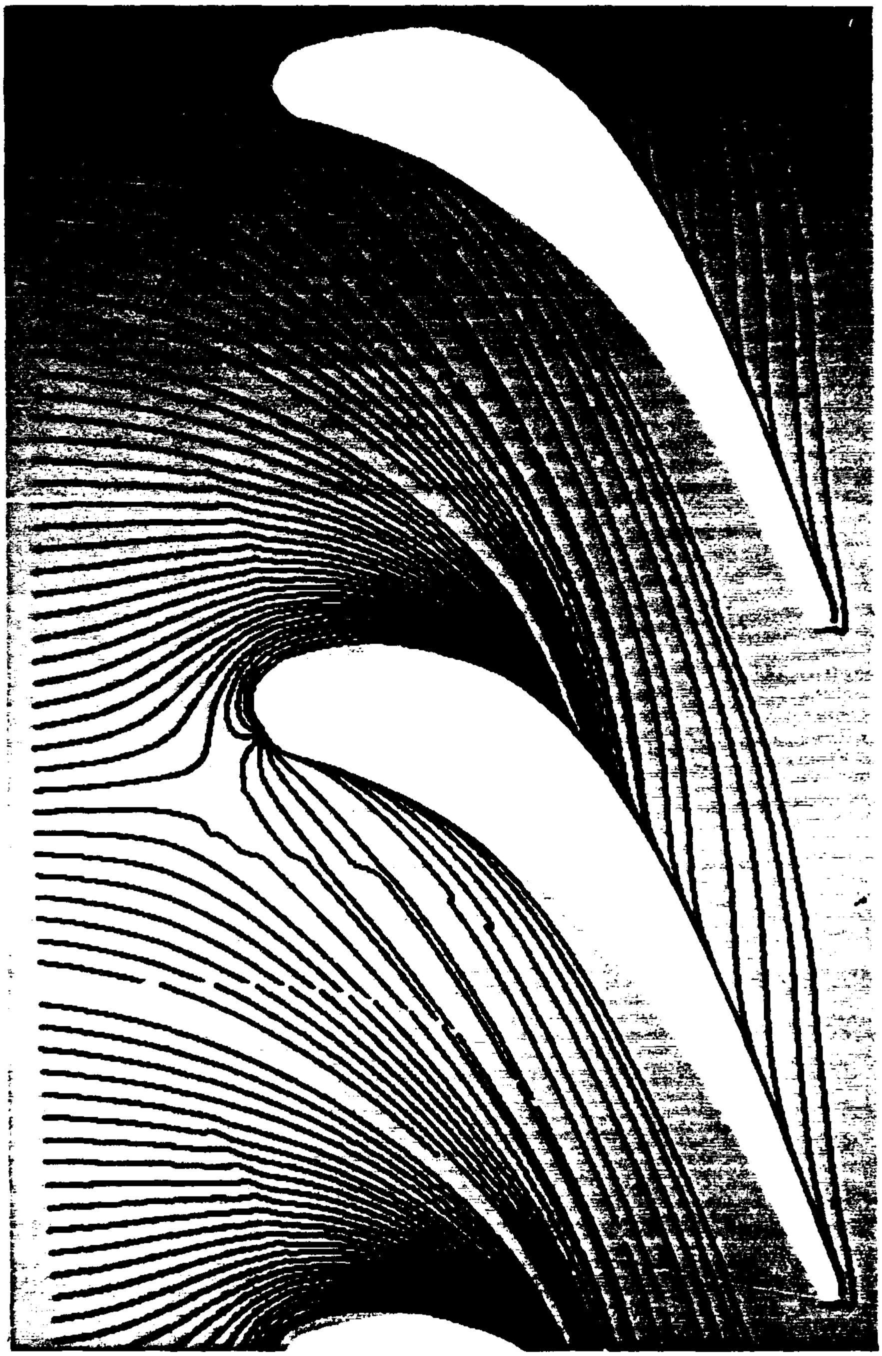

Fig. V–4c Computed First Stator and Rotor Surface Flow, Stator Hub

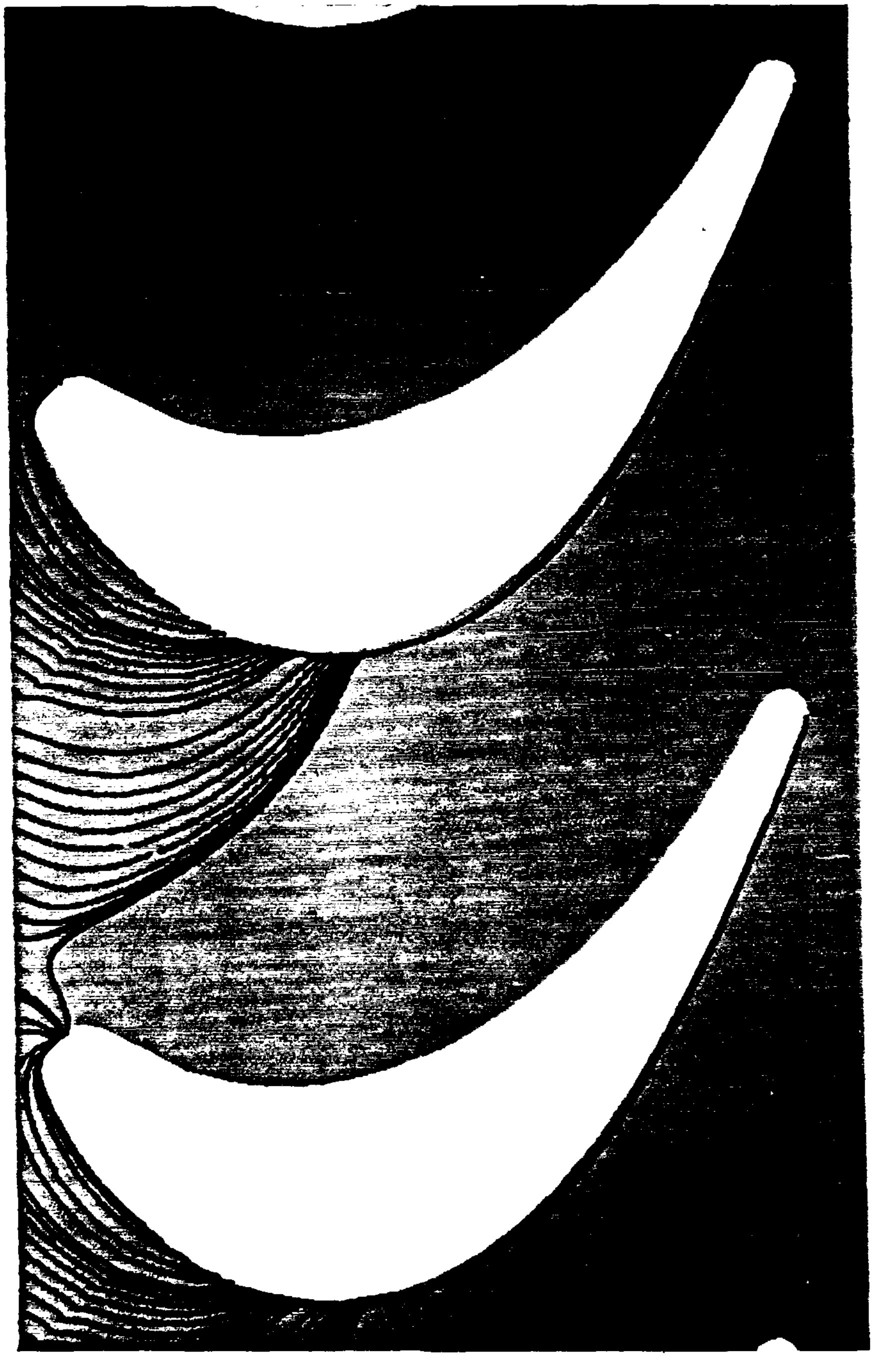

Fig. V–4d Computed First Stator and Rotor Surface Flow, Rotor Hub

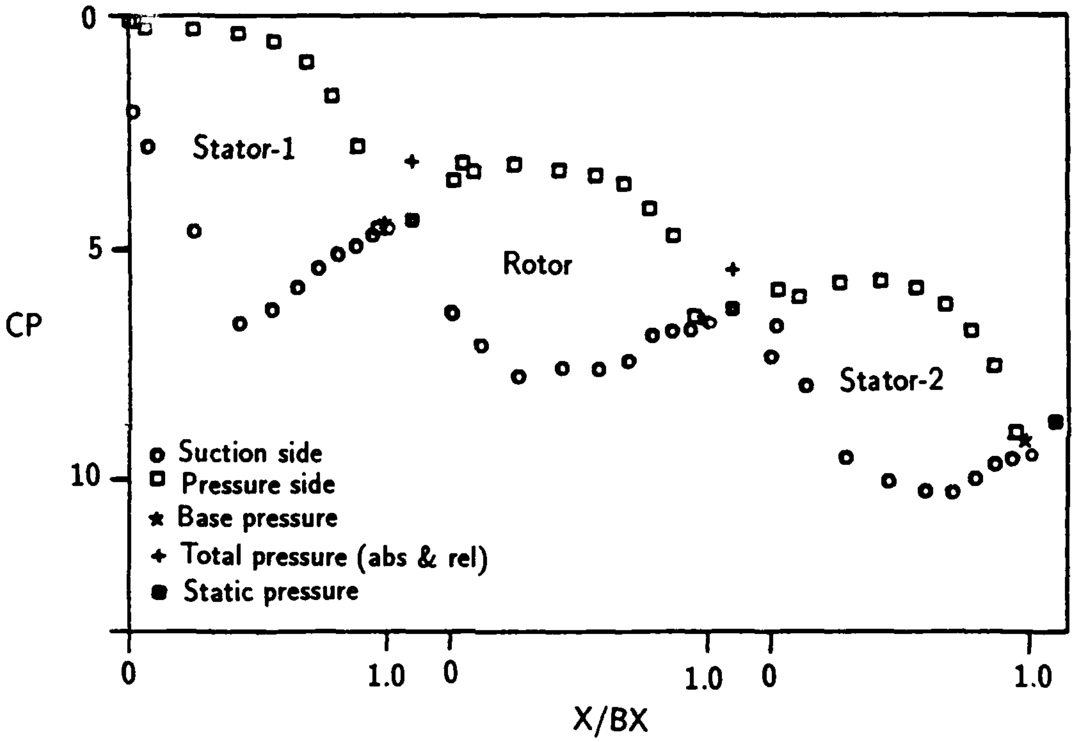

Fig. V–5 **Airfoil Midspan Pressure Distributions (axial gaps not to scale)**

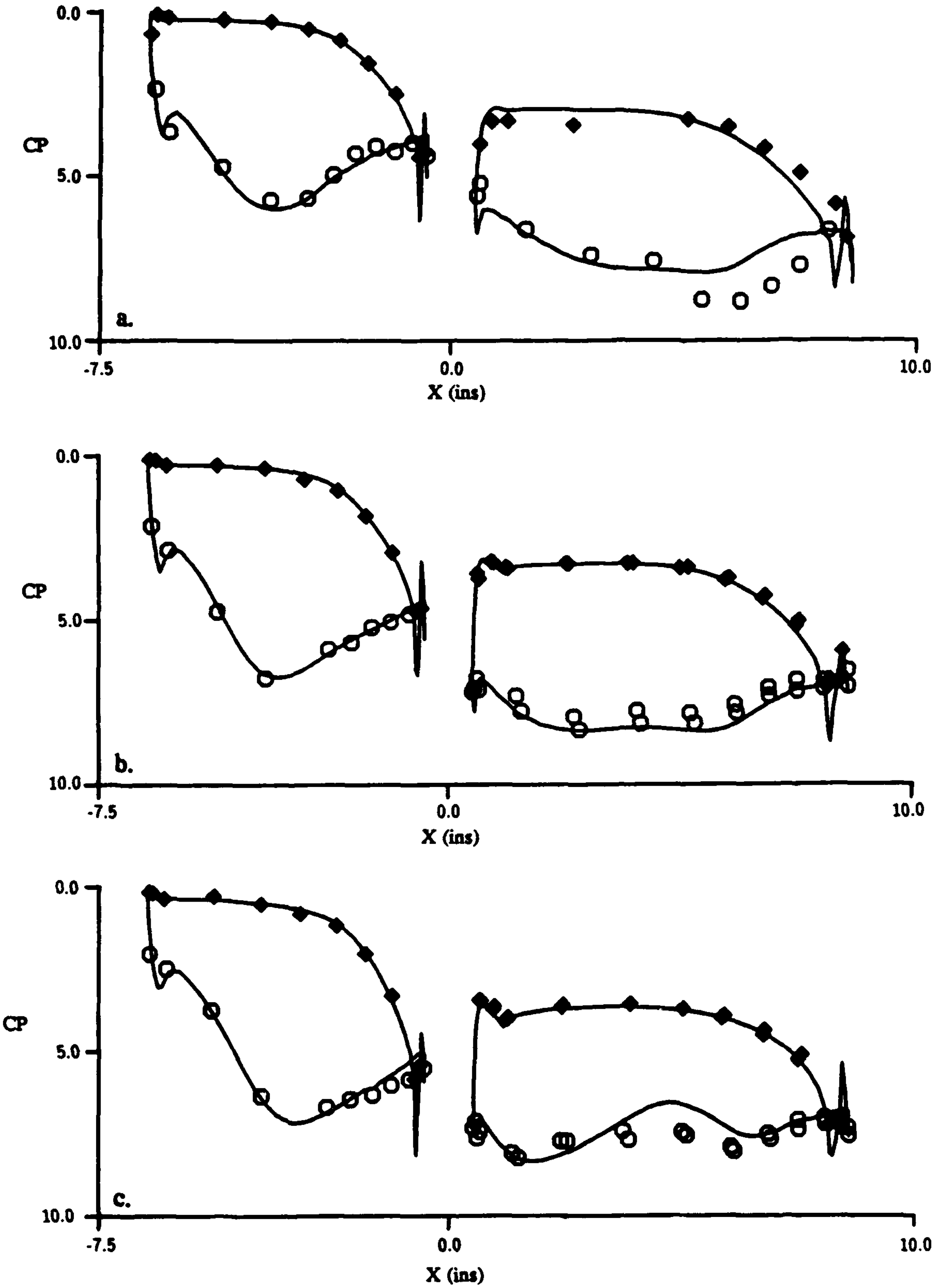

Fig. V–6 First Stator and Rotor Fullspan Pressure Distributions

a. 98% Span

b. 50% Span

c. 2% Span

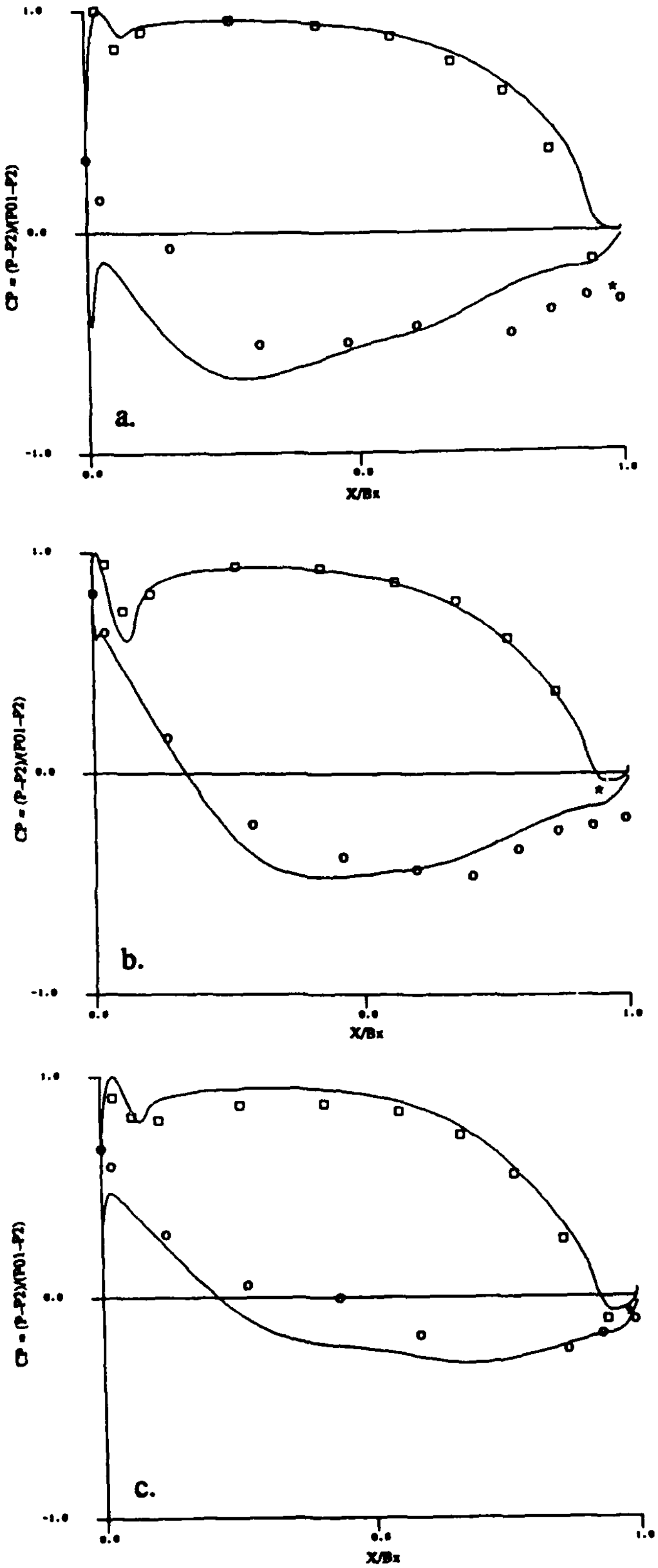

Fig. V–7 Second Stator Fullspan Pressure Distributions
a. 98% Span
b. 50% Span
c. 2% Span

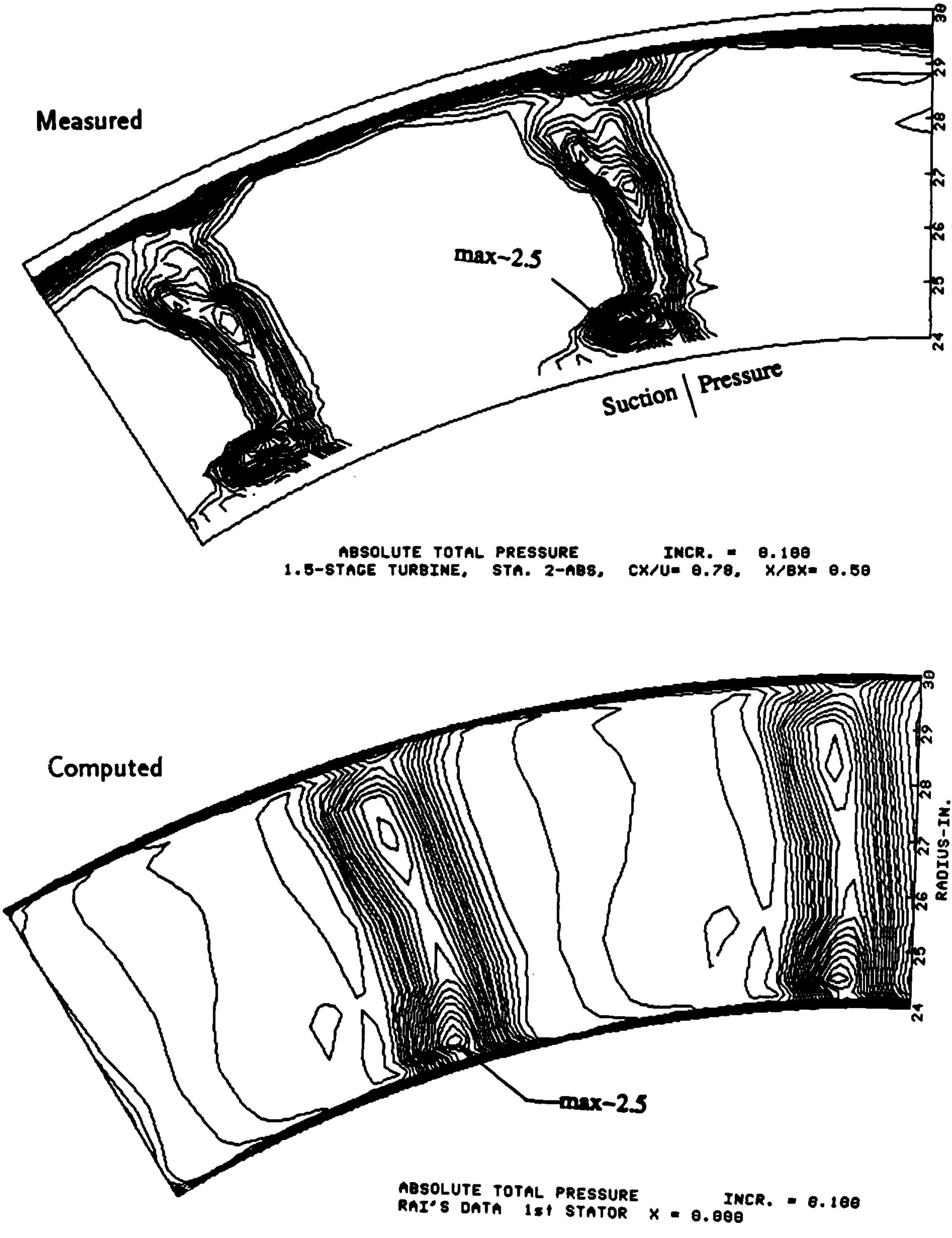

Fig. V–8a First Stator Exit Results, Plane 2–Absolute, Measured 17% aft and Computed 9% aft,
Absolute Total Pressure Contours, $\Delta CPTABS = 0.10$

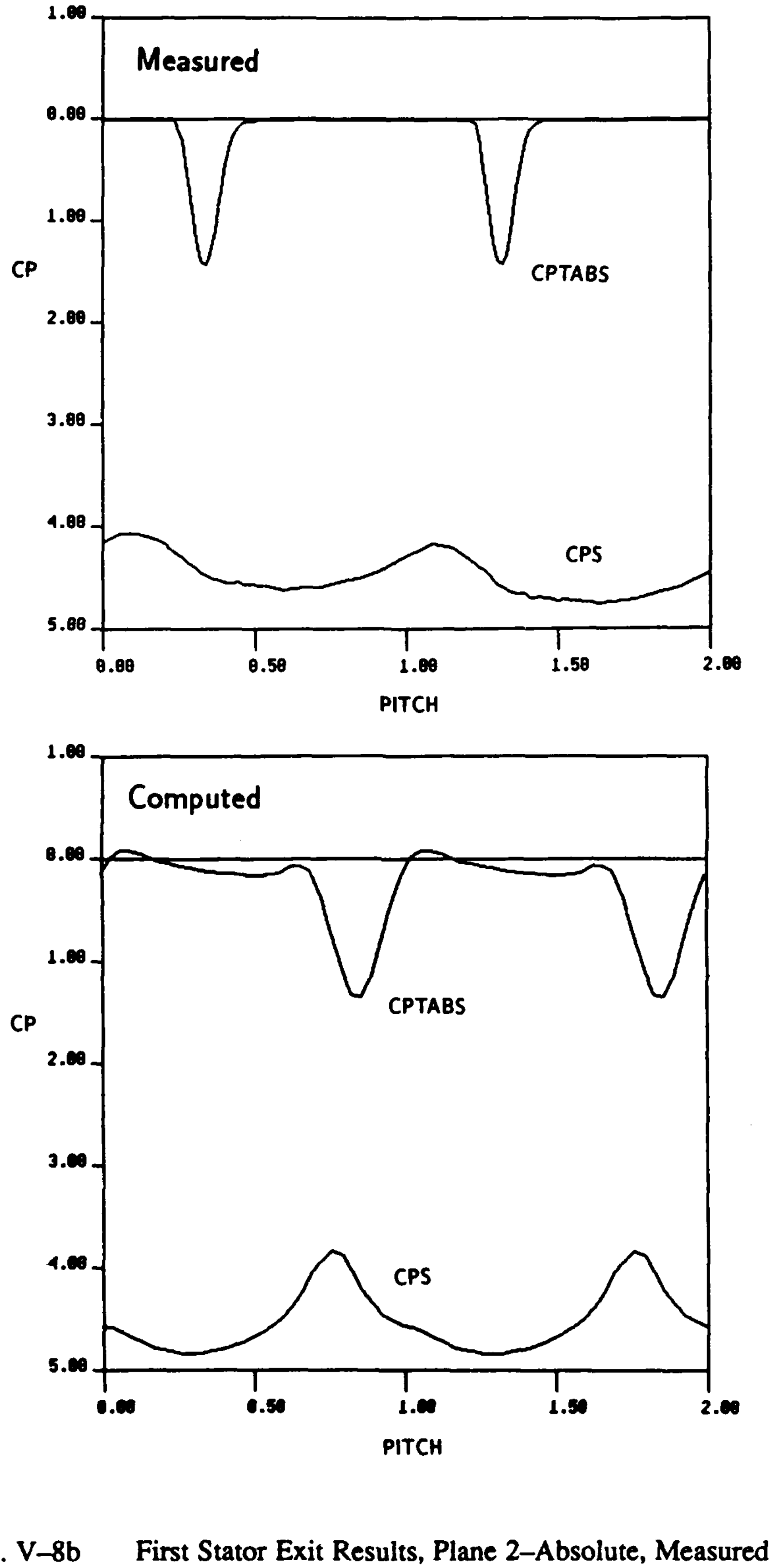

Fig. V–8b First Stator Exit Results, Plane 2–Absolute, Measured 17% aft and Computed 9% aft,
Total and Static Pressures at Midspan

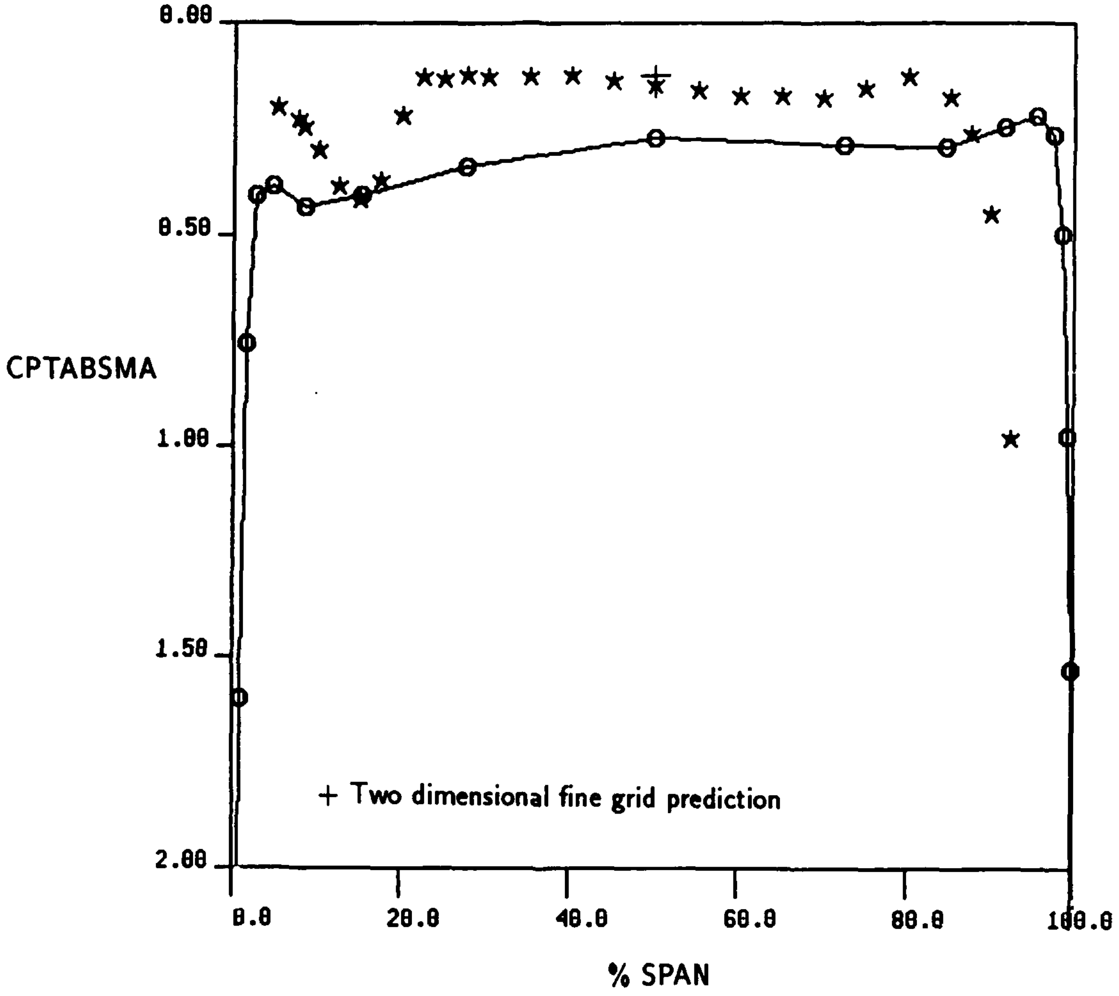

Fig. V–8c First Stator Exit Results, Plane 2–Absolute, Measured 17% aft and Computed 9% aft,
Absolute Total Pressure, Cicumferential Mass Average

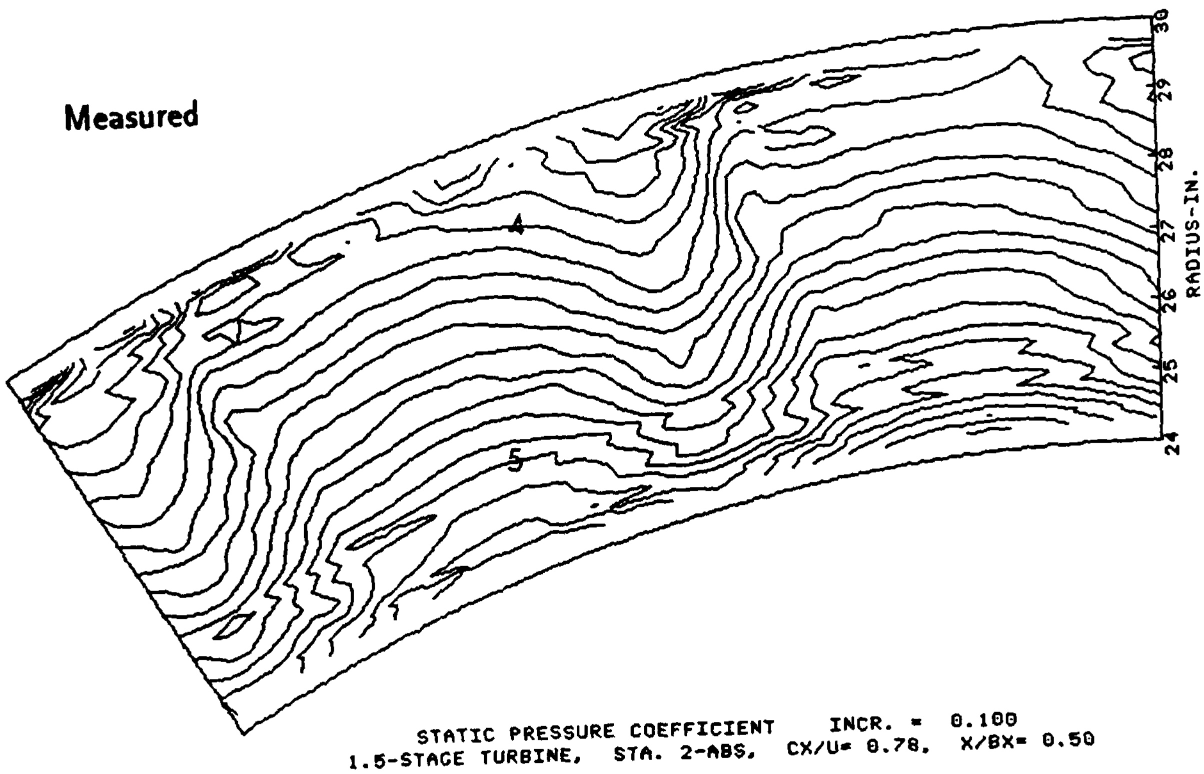

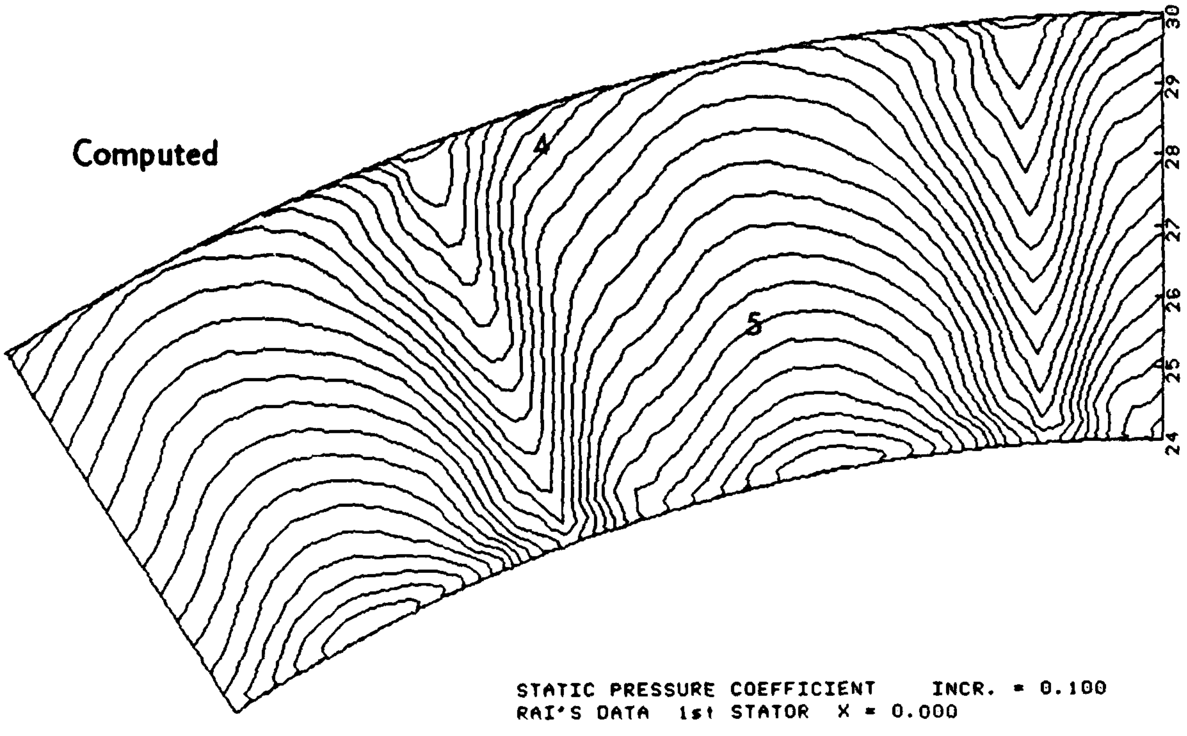

Fig. V–8d First Stator Exit Results, Plane 2–Absolute, Measured 17% aft and Computed 9% aft, Static Pressure Contours, $\Delta CPS = 0.10$

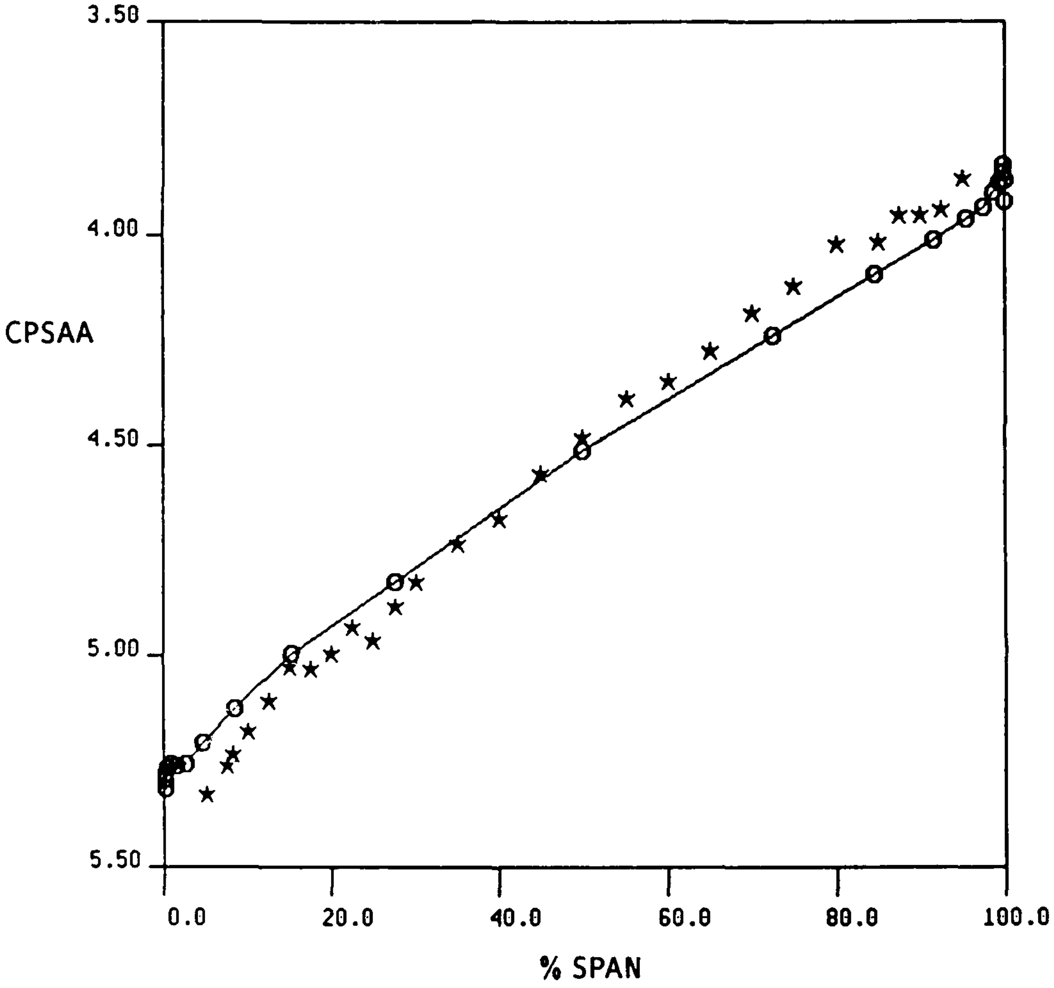

Fig. V–8e First Stator Exit Results, Plane 2–Absolute, Measured 17% aft and Computed 9% aft,
Static Pressure, Circumferential Area Average

Measured

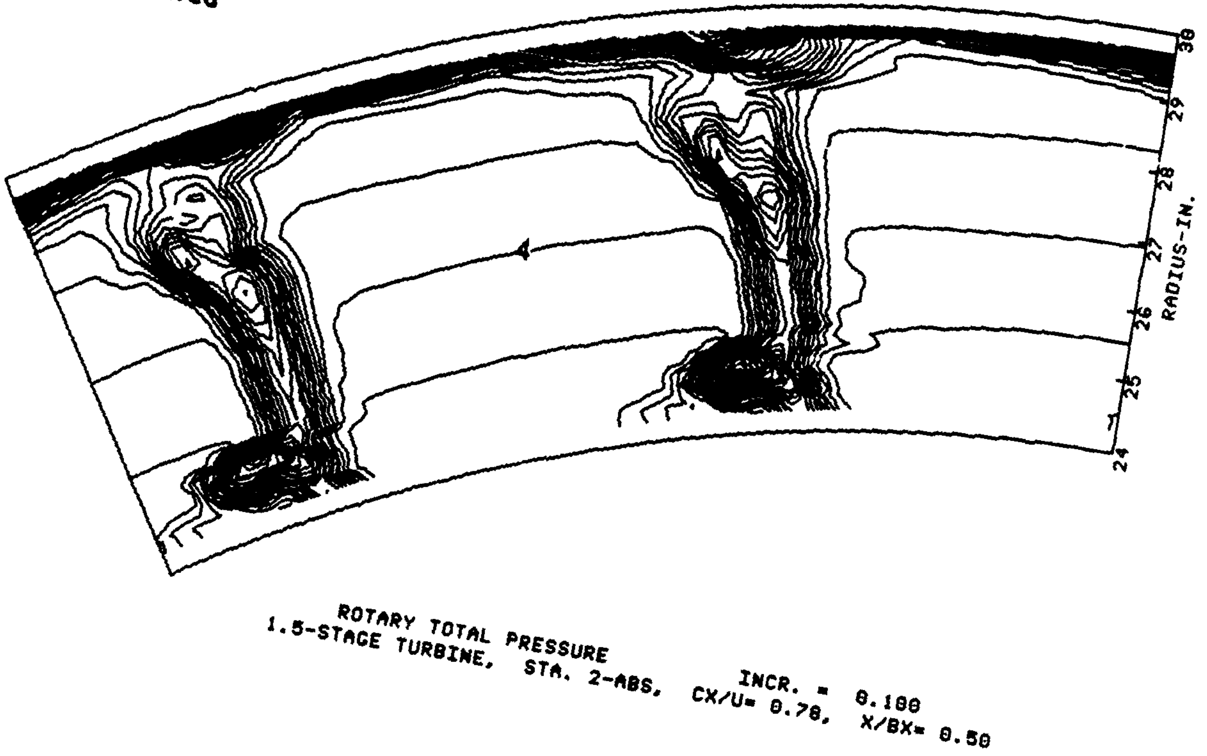

Computed

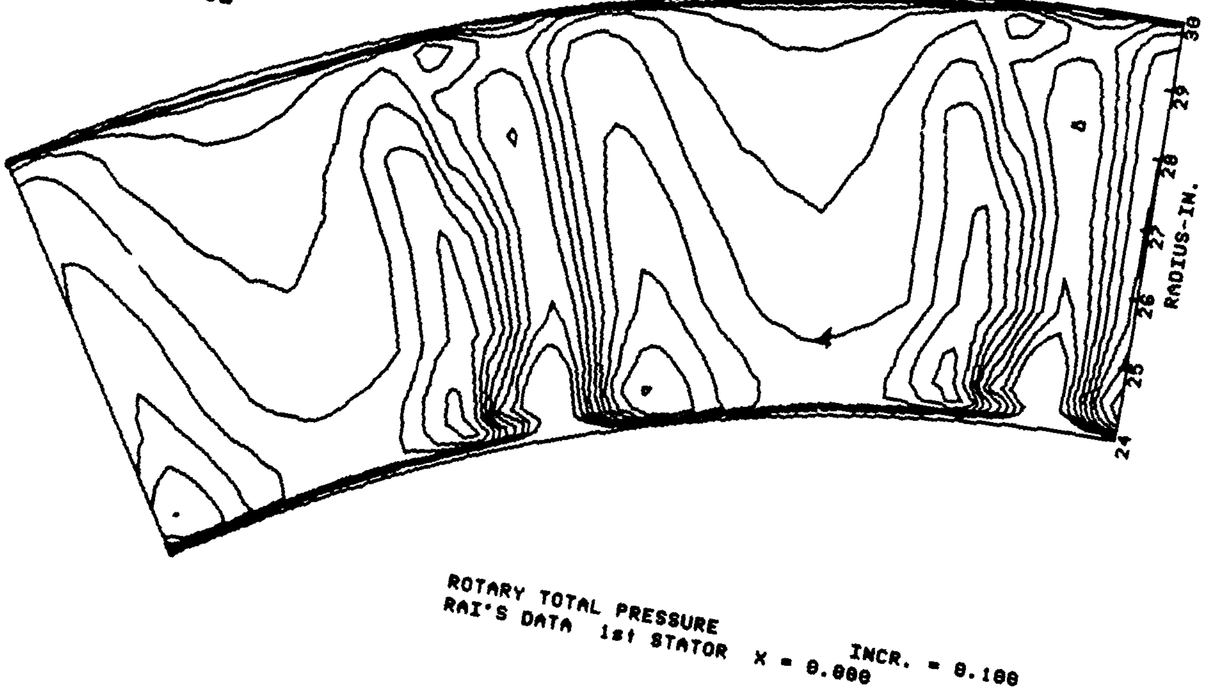

Fig. V–8f First Stator Exit Results, Plane 2–Absolute, Measured 17% aft and Computed 9% aft,
Rotary Total Pressure Contours, $\Delta CPTROT = 0.10$

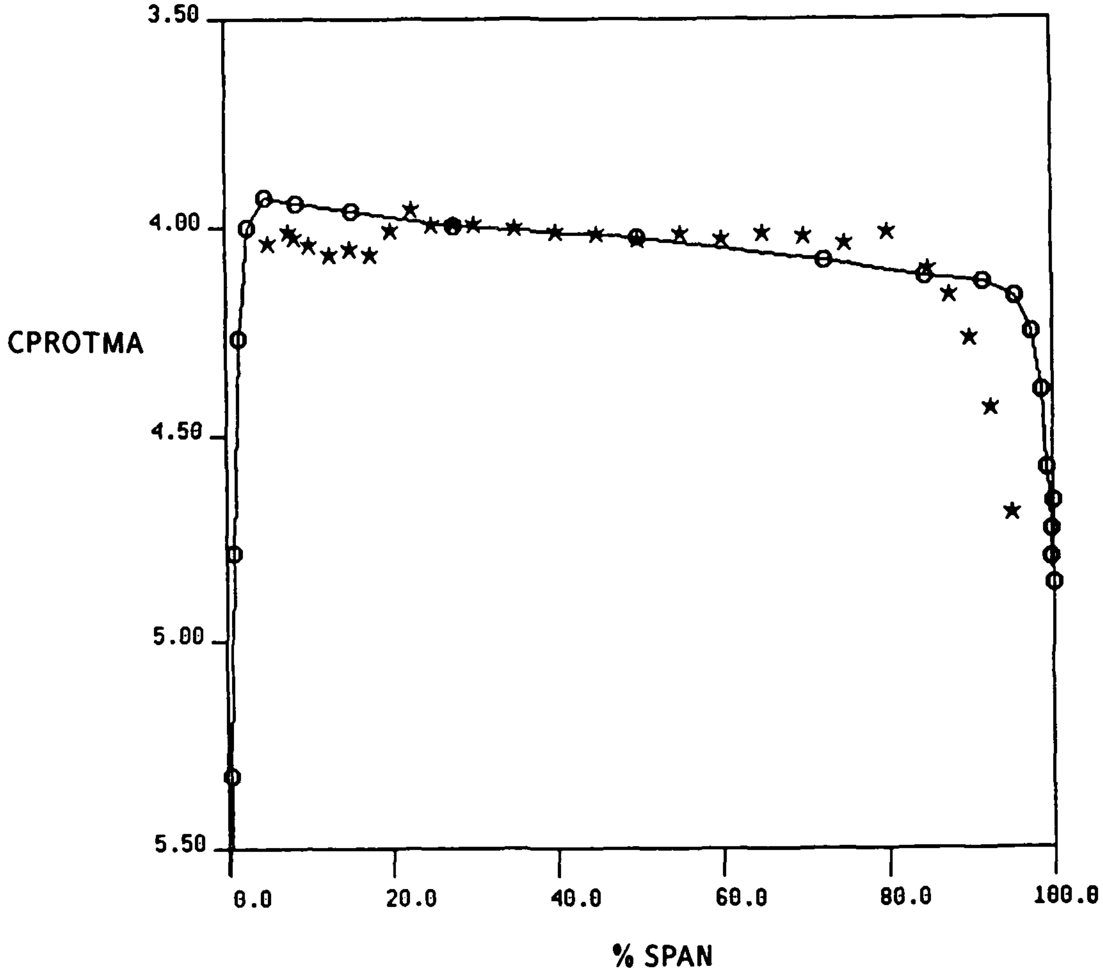

Fig. V–8g First Stator Exit Results, Plane 2–Absolute, Measured 17% aft and Computed 9% aft,
Rotary Total Pressure, Circumferential Mass Average

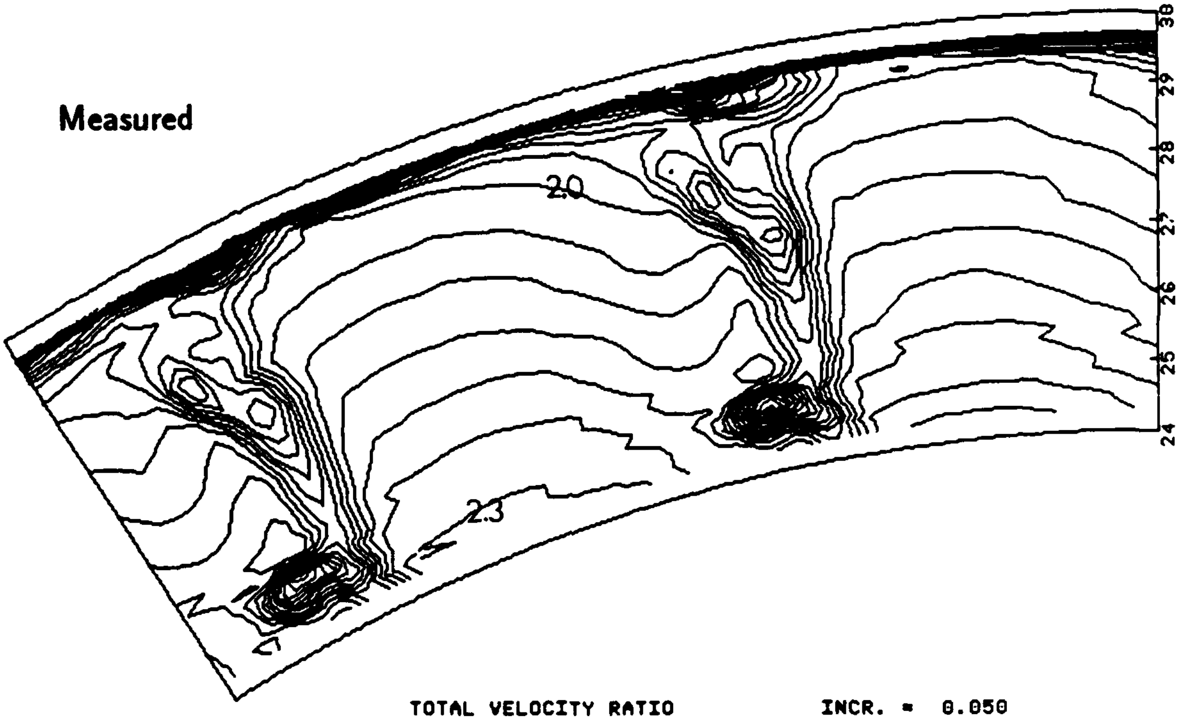

TOTAL VELOCITY RATIO INCR. = 0.050
1.5-STAGE TURBINE, STA. 2-ABS, CX/U= 0.78, X/BX= 0.50

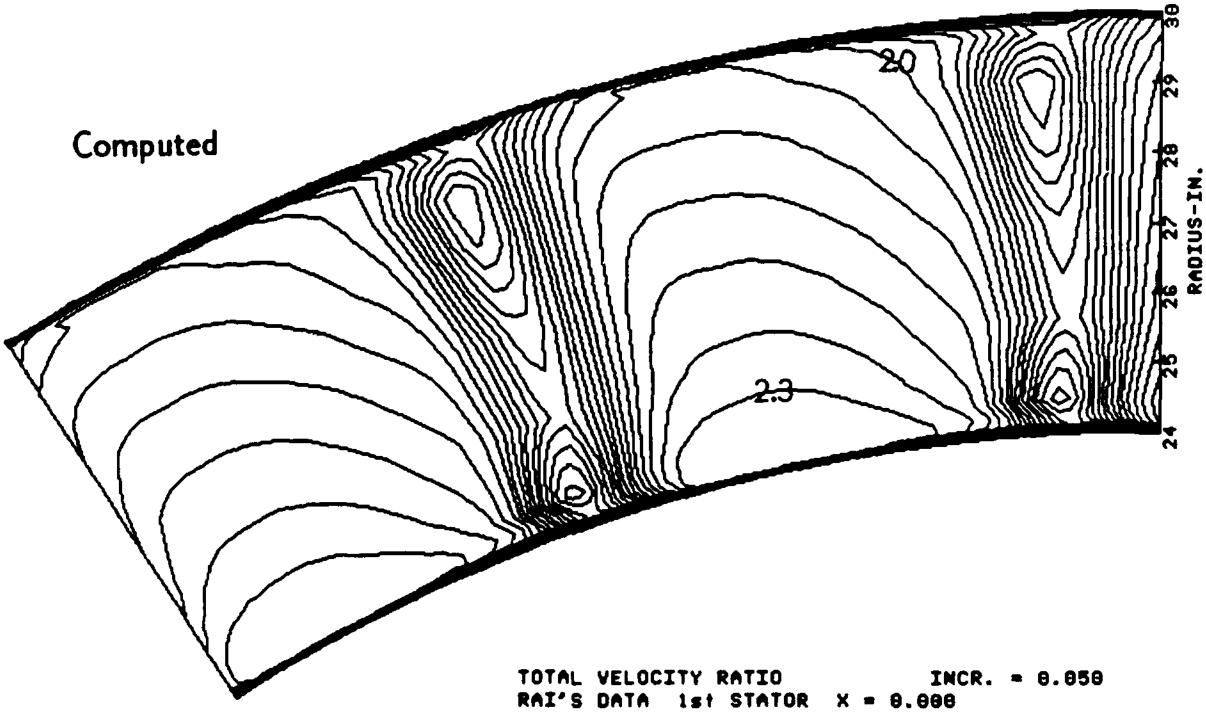

TOTAL VELOCITY RATIO INCR. = 0.050
RAI'S DATA 1st STATOR X = 0.000

Fig. V–8h First Stator Exit Results, Plane 2–Absolute, Measured 17% aft and Computed 9% aft,
Absolute Velocity Contours, $\Delta(C/U_m) = 0.05$

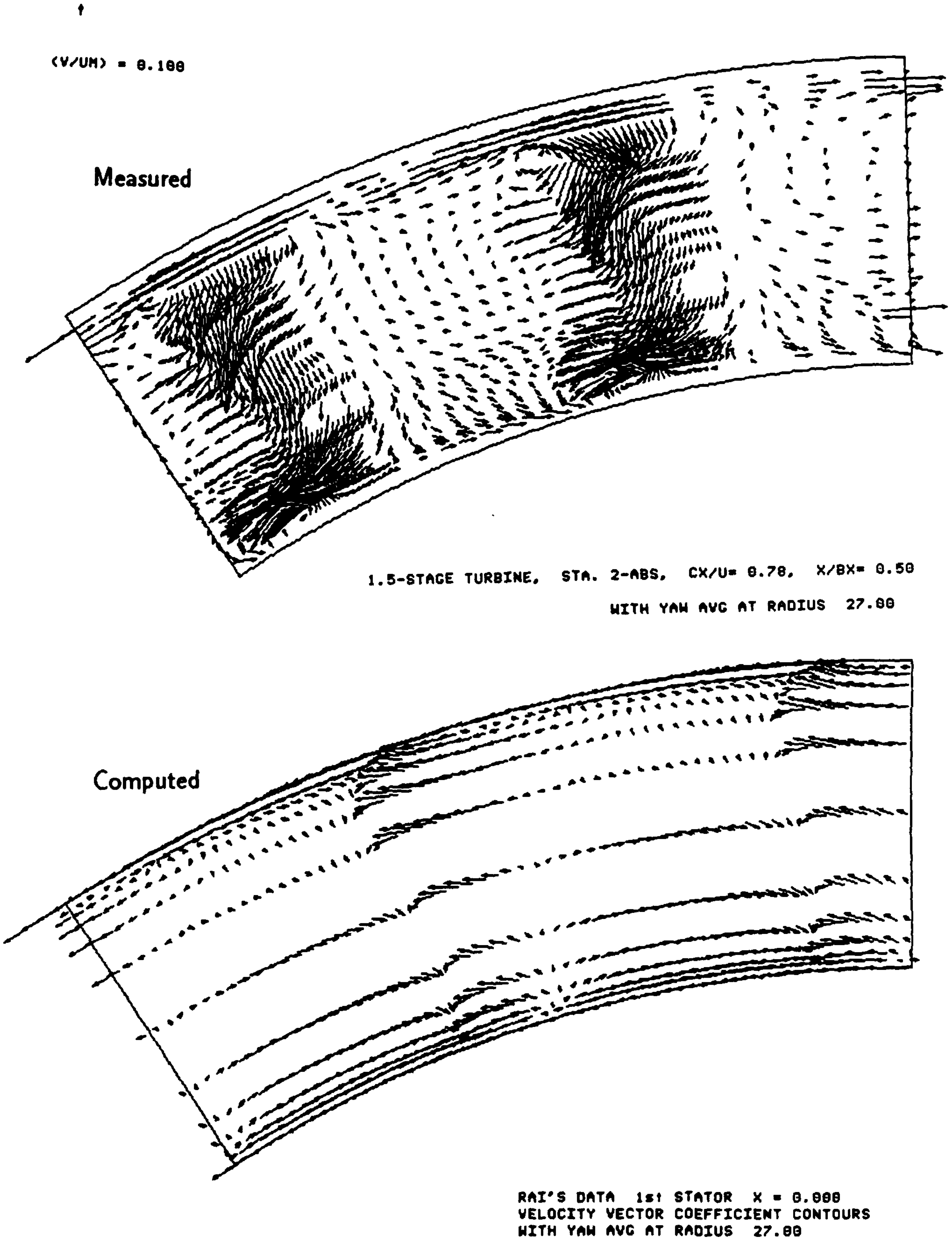

Fig. V–8i First Stator Exit Results, Plane 2–Absolute, Measured 17% aft and Computed 9% aft,
Secondary Flow with Average Yaw (Absolute) at 50% Span

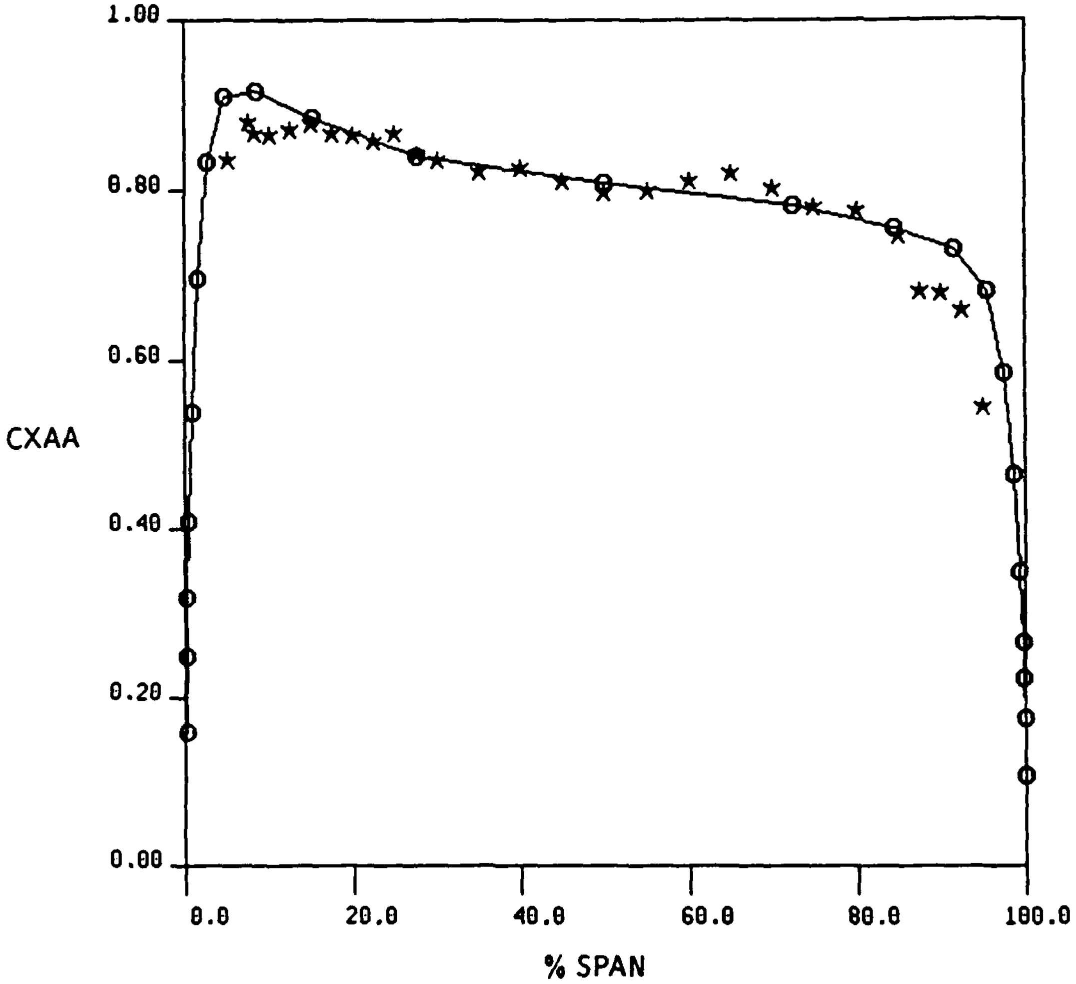

Fig. V–8j First Stator Exit Results, Plane 2–Absolute, Measured 17% aft and Computed 9% aft, Axial Velocity (C_x/U_m), Circumferential Area Average

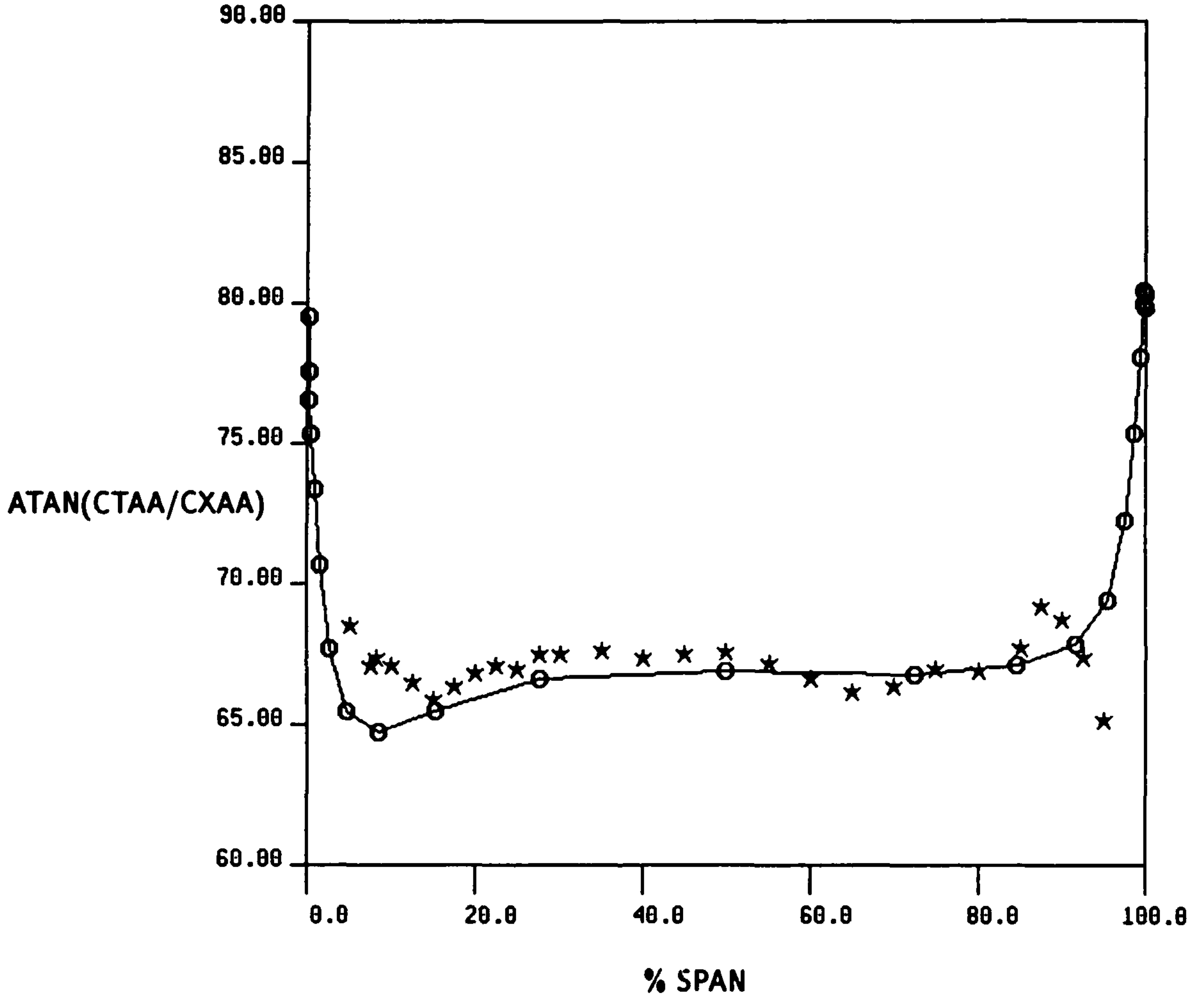

Fig. V–8k First Stator Exit Results, Plane 2–Absolute, Measured 17% aft and Computed 9% aft, Absolute Flow Angle (Arctan[CTAA/CXAA])

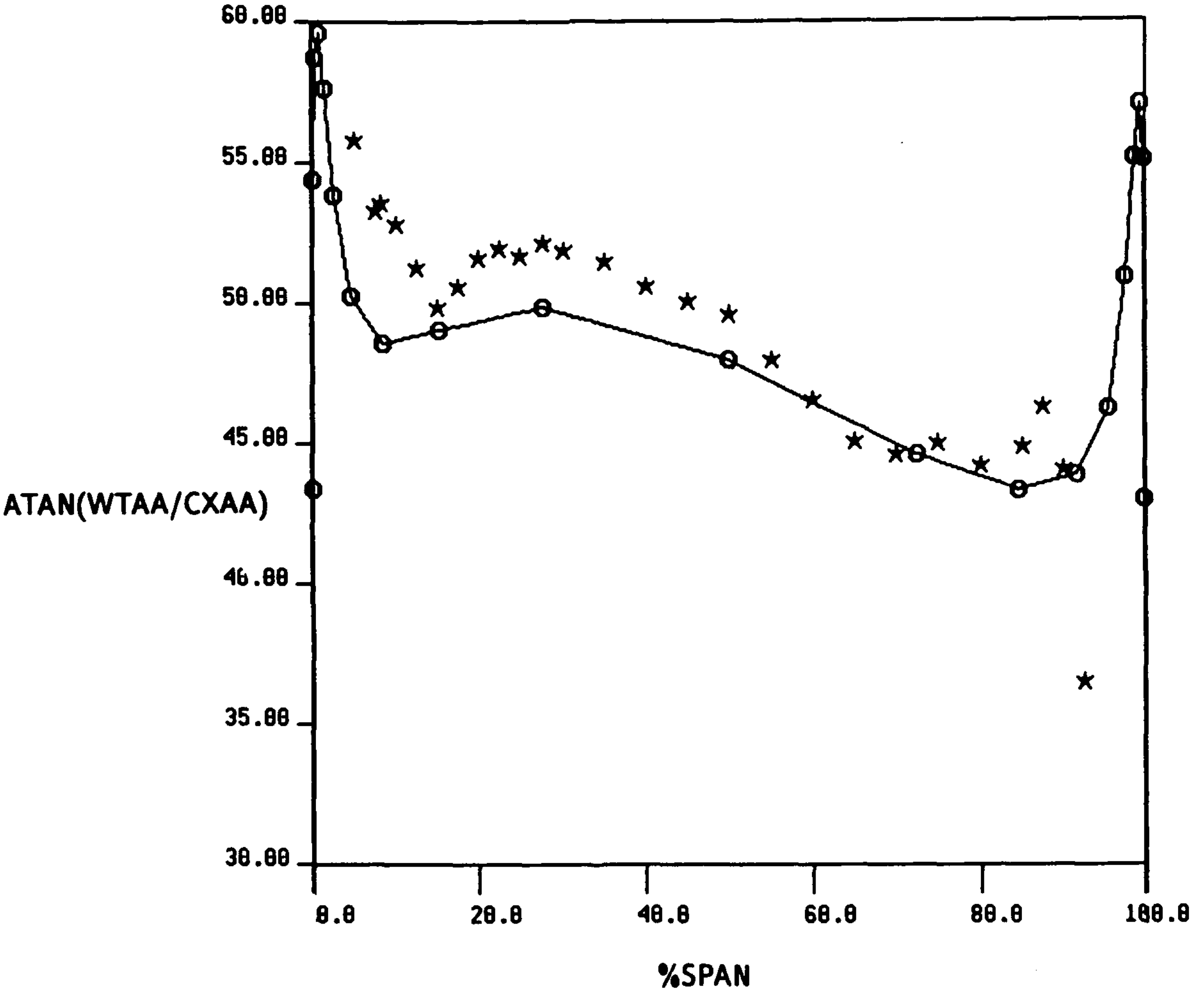

Fig. V–81 First Stator Exit Results, Plane 2–Absolute, Measured 17% aft and Computed 9% aft,
Relative Flow Angle (Arctan[WTAA/CXAA])

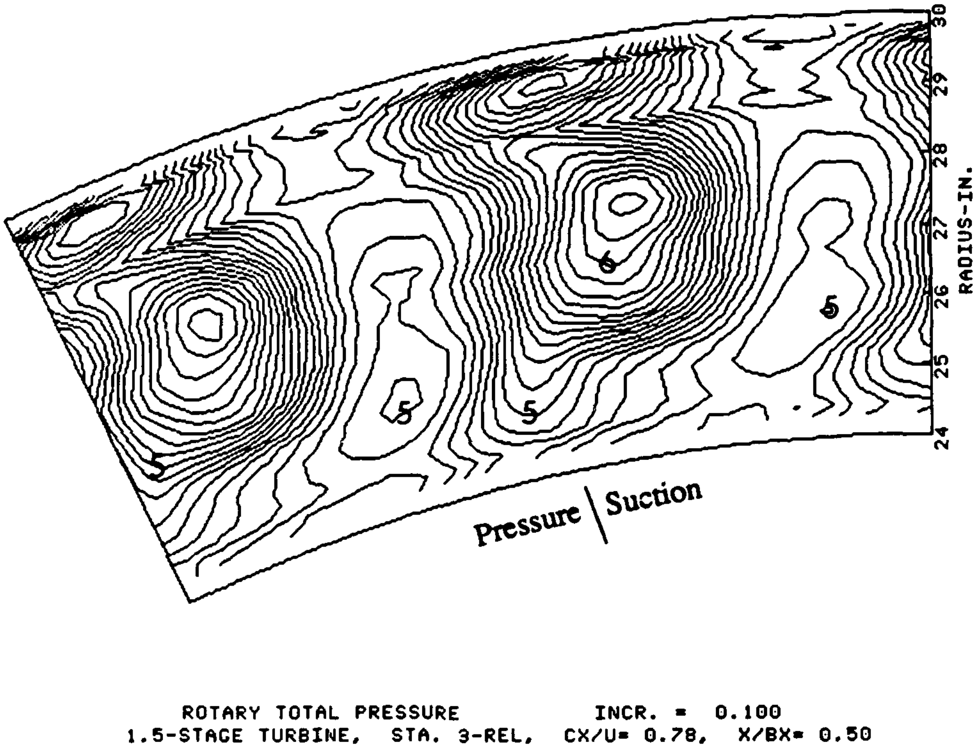

Fig. V–9a Rotor Exit Results, Plane 3–Relative, Measured 36% aft, Rotary Total Pressure Contours, $\Delta CPTROT = 0.10$

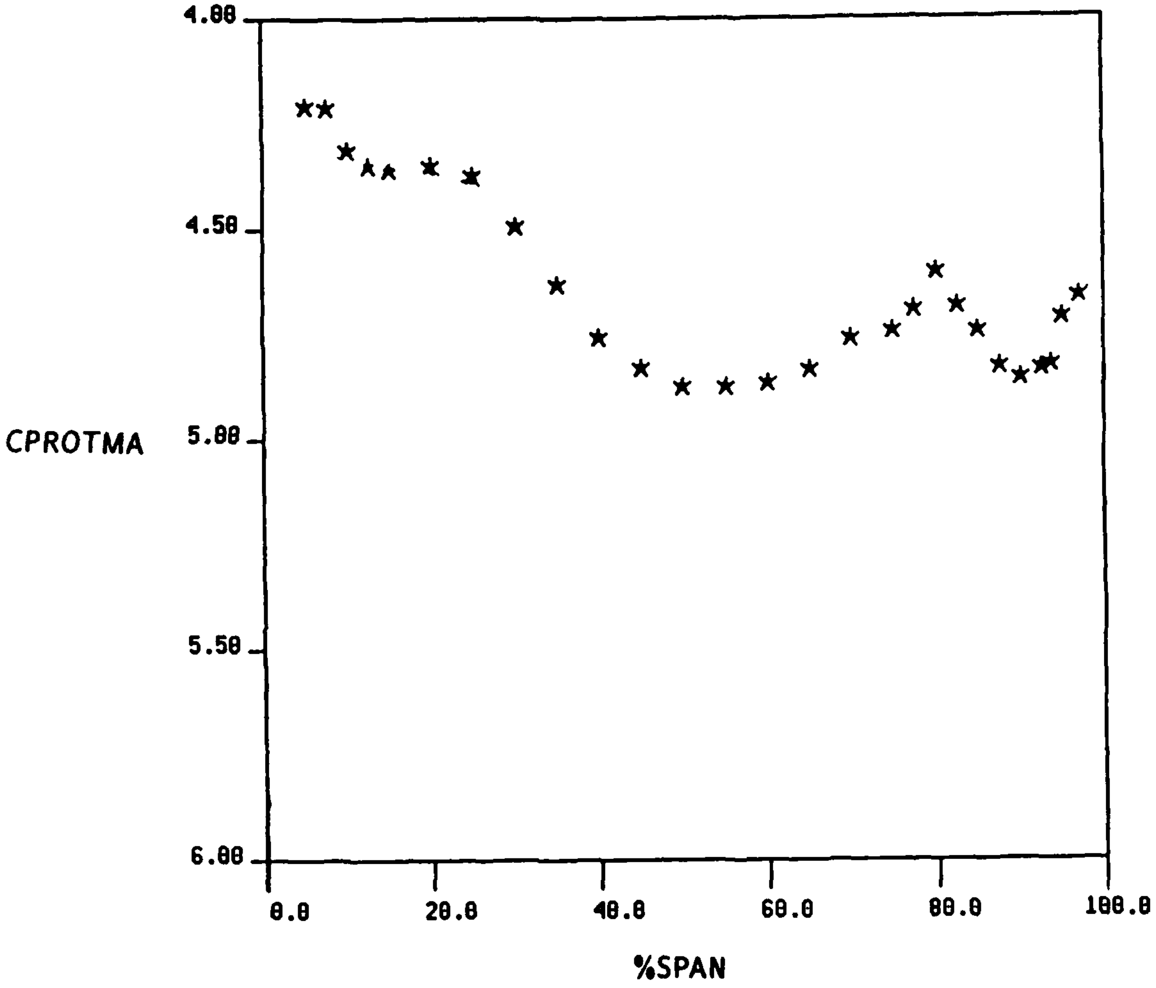

Fig. V–9b Rotor Exit Results, Plane 3–Relative, Measured 36% aft, Rotary Total Pressure, Circumferential Mass Average

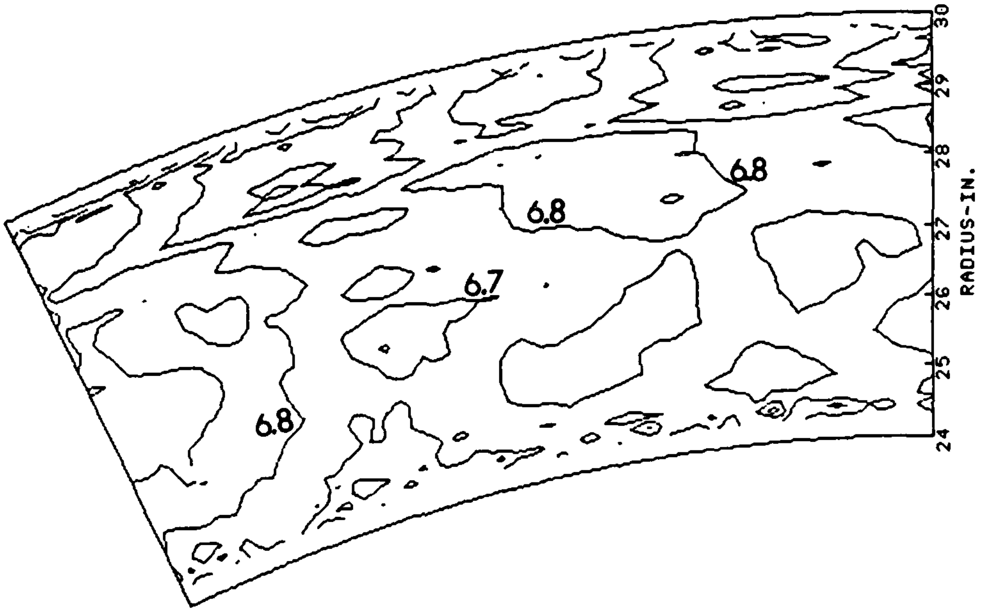

STATIC PRESSURE COEFFICIENT   INCR. = 0.100
1.5-STAGE TURBINE, STA. 3-REL, CX/U= 0.78, X/BX= 0.50

Fig. V–9c Rotor Exit Results, Plane 3–Relative, Measured 36% aft, Static Pressure Contours, $\Delta CPS = 0.10$

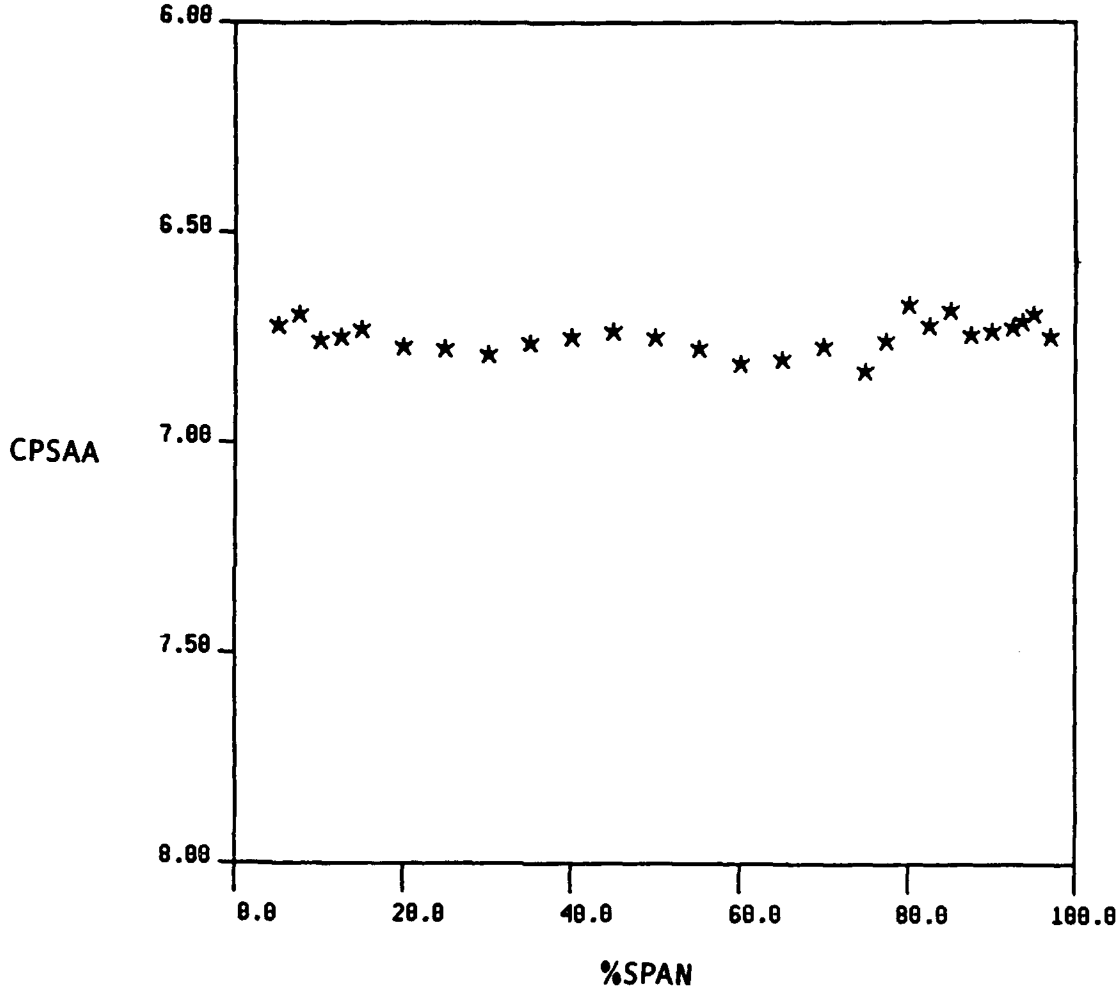

Fig. V–9d Rotor Exit Results, Plane 3–Relative, Measured 36% aft, Static Pressure, Circumferential Area Average

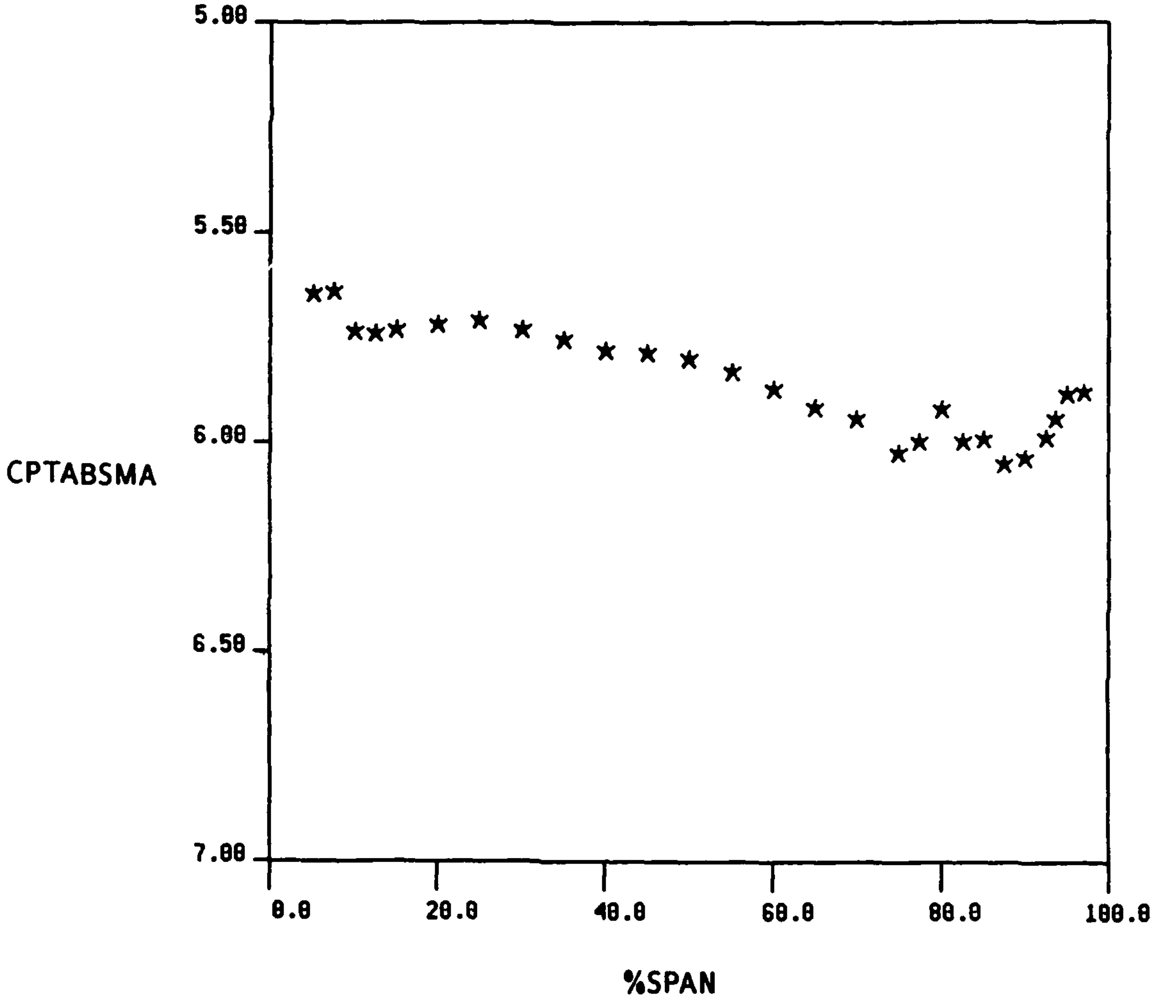

Fig. V–9e Rotor Exit Results, Plane 3–Relative, Measured 36% aft, Absolute Total Pressure, Circumferential Mass Average

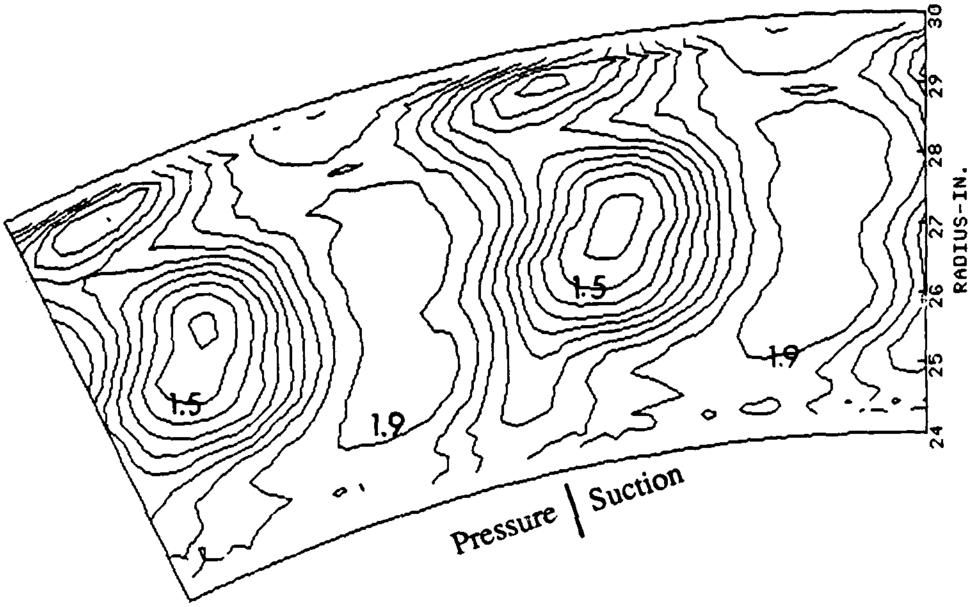

TOTAL VELOCITY RATIO INCR. = 0.050
1.5-STAGE TURBINE, STA. 3-REL, CX/U= 0.78, X/BX= 0.50

Fig. V–9f Rotor Exit Results, Plane 3–Relative, Measured 36% aft, Relative Velocity Contours, $\Delta(W/U_m) = 0.05$

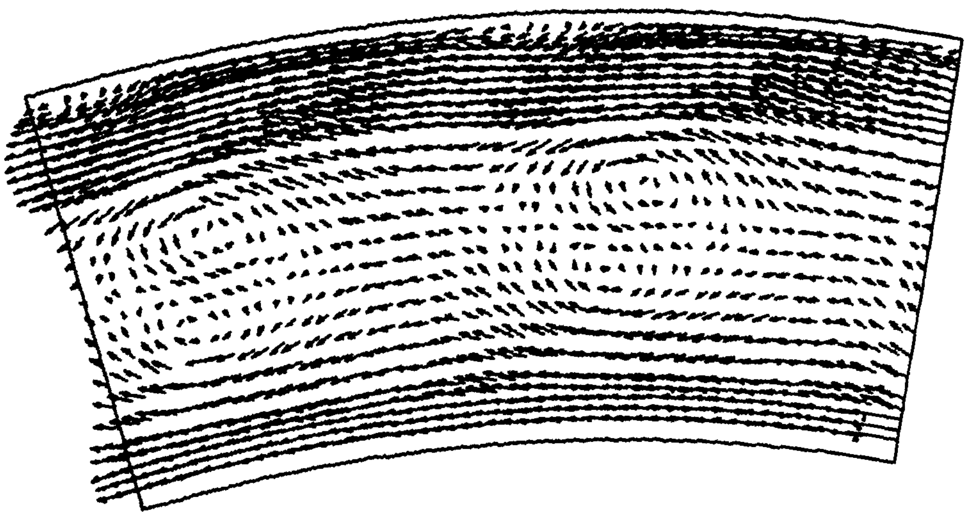

1.5-STAGE TURBINE, STA. 3-REL, CX/U= 0.78, X/BX= 0.50
WITH YAW AVG AT RADIUS 27.00

Fig. V–9g Rotor Exit Results, Plane 3–Relative, Measured 36% aft, Secondary Flow with Average Yaw (Relative) at 50% Span

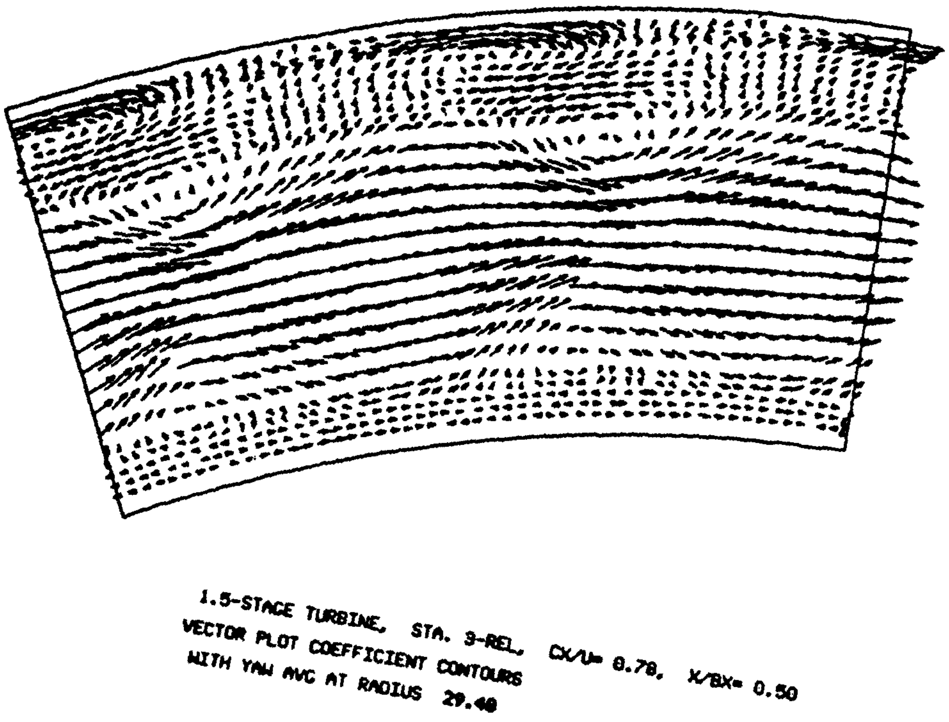

Fig. V–9h Rotor Exit Results, Plane 3–Relative, Measured 36% aft, Secondary Flow with Average Yaw (Relative) at 90% Span

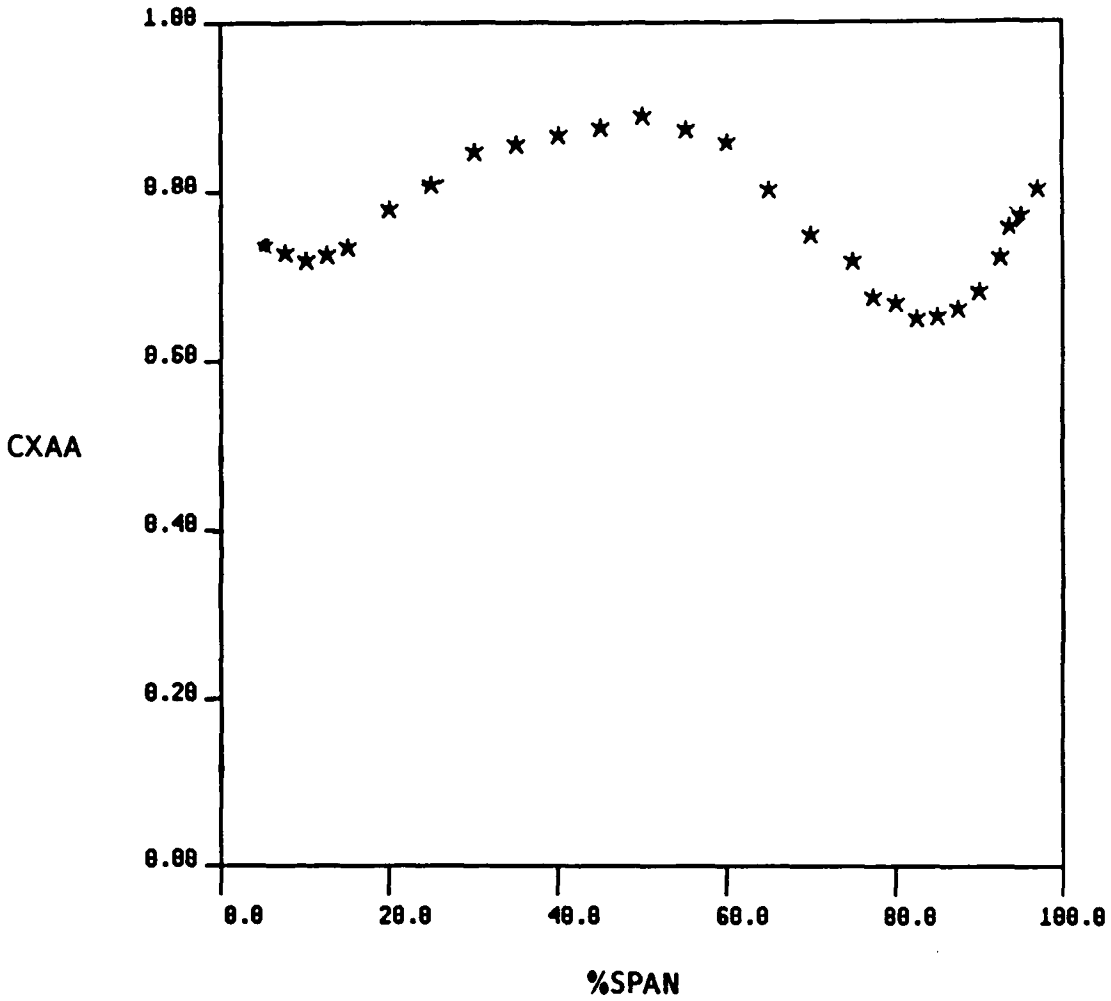

Fig. V–9i Rotor Exit Results, Plane 3–Relative, Measured 36% aft, Axial Velocity (C_x/U_m), Circumferential Area Average

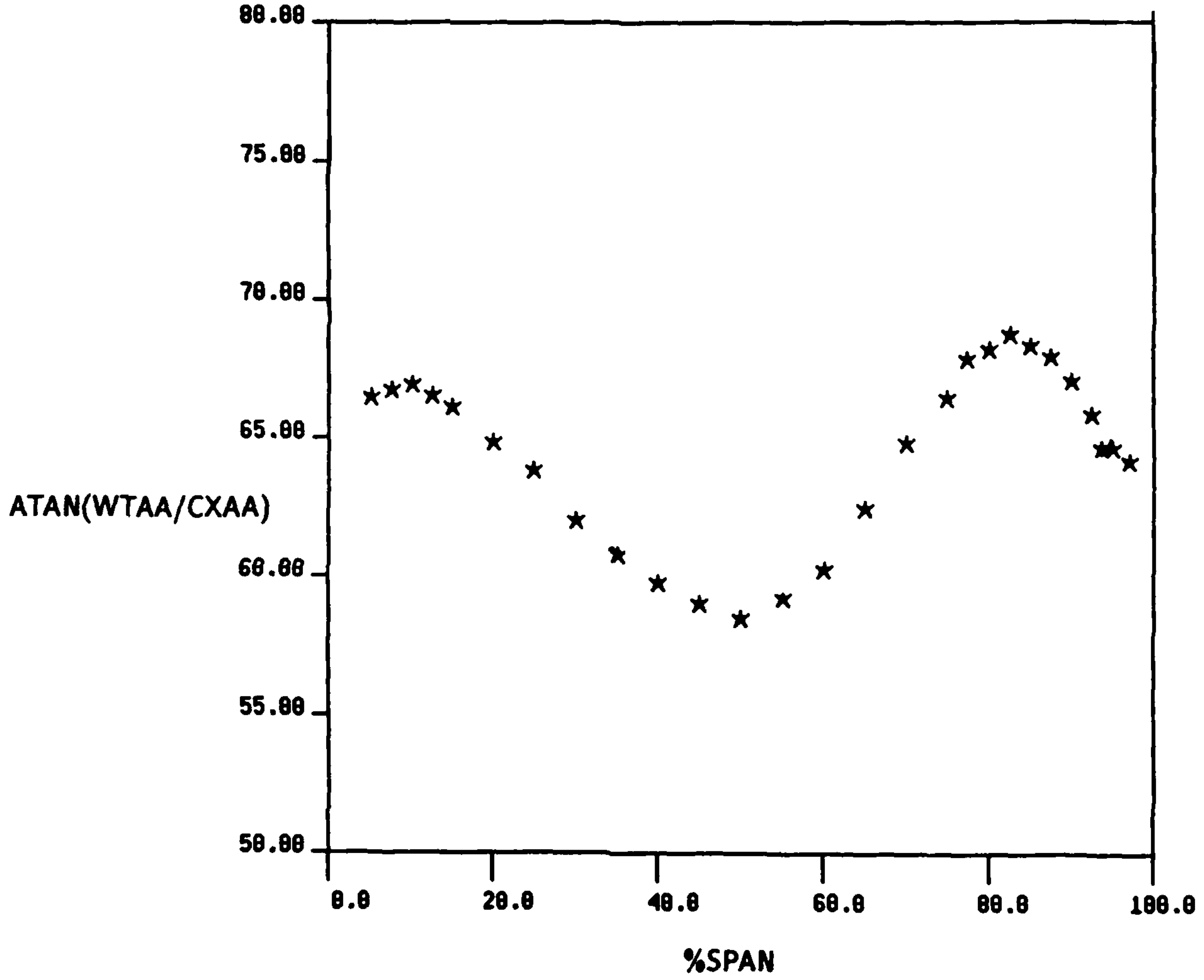

Fig. V–9j Rotor Exit Results, Plane 3–Relative, Measured 36% aft, Relative Flow Angle (Arctan[WTAA/CXAA])

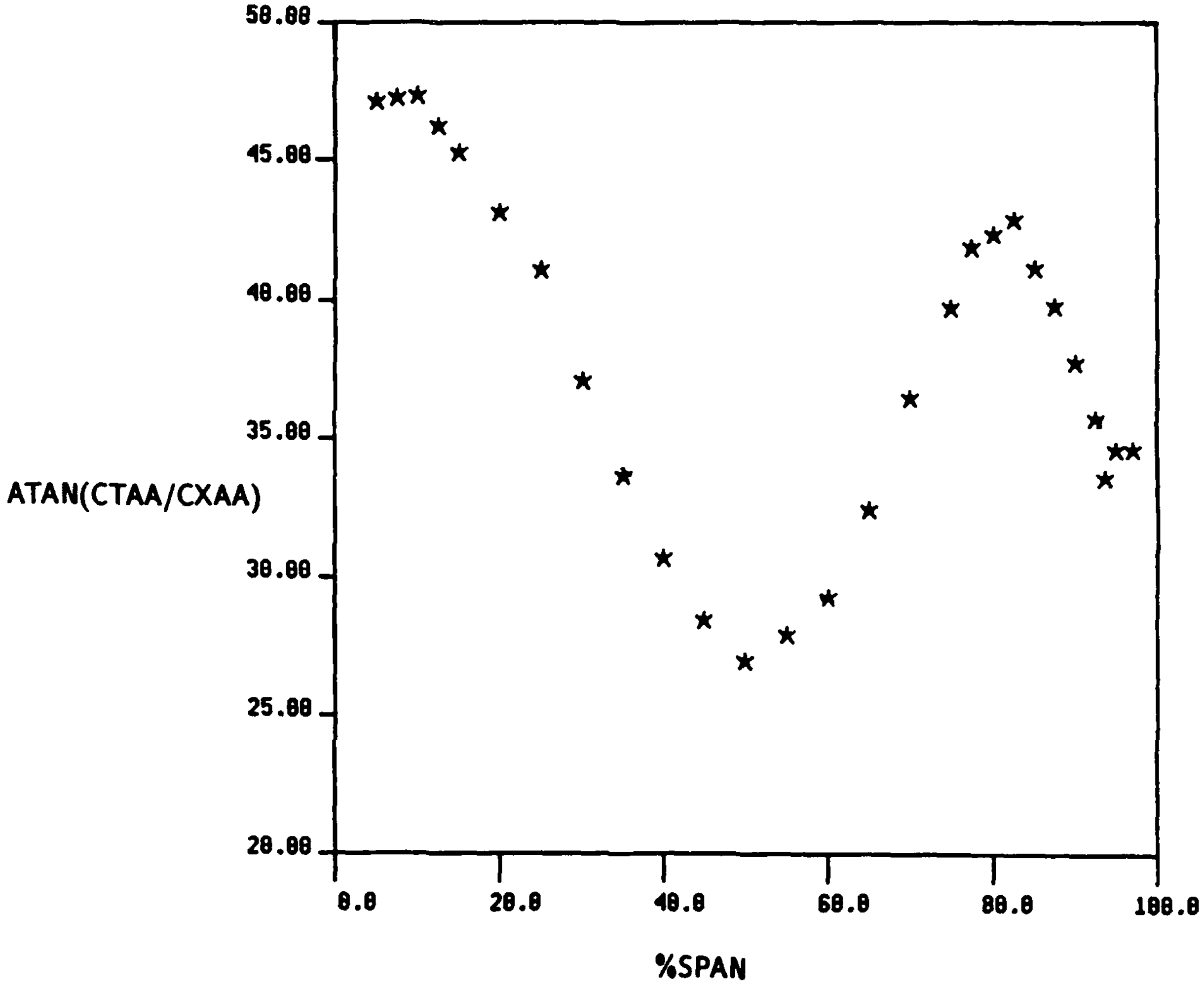

Fig. V–9k Rotor Exit Results, Plane 3–Relative, Measured 36% aft, Absolute Flow Angle (Arctan[CTAA/CXAA])

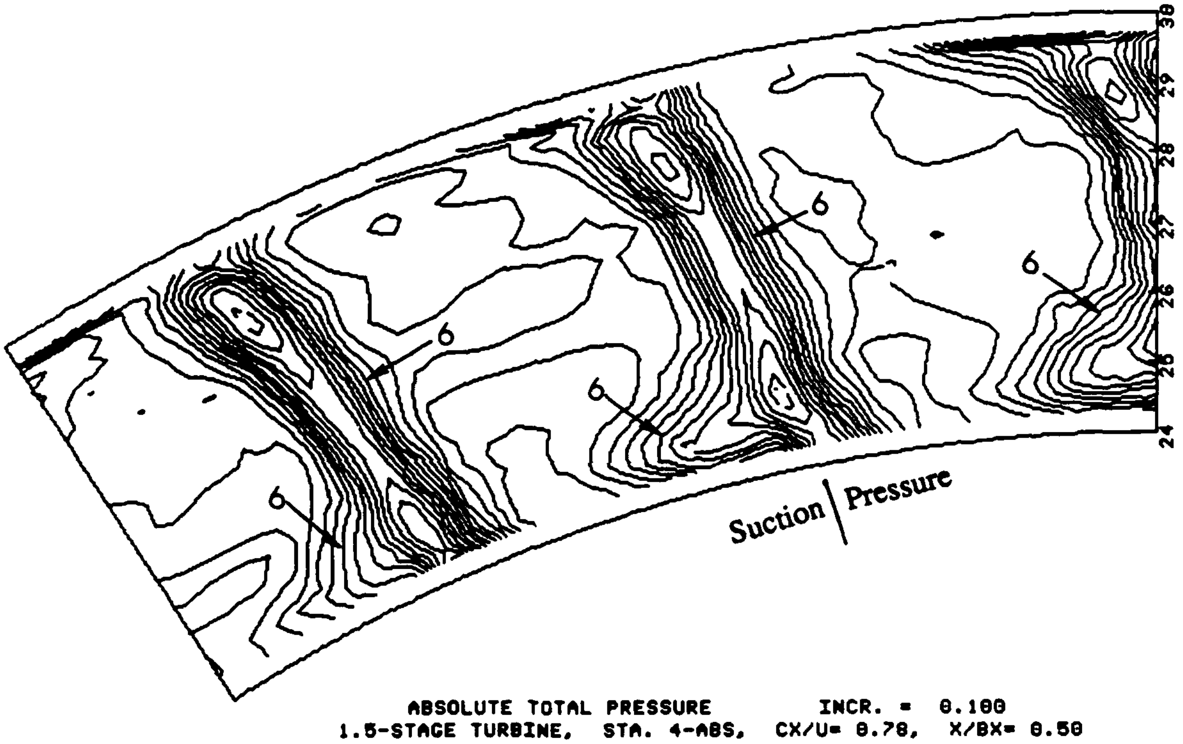

Fig. V–10a Second Stator Exit Results, Plane 4–Abs., Measured 14% aft, Absolute Total Pressure Contours, $\Delta CPTABS = 0.10$

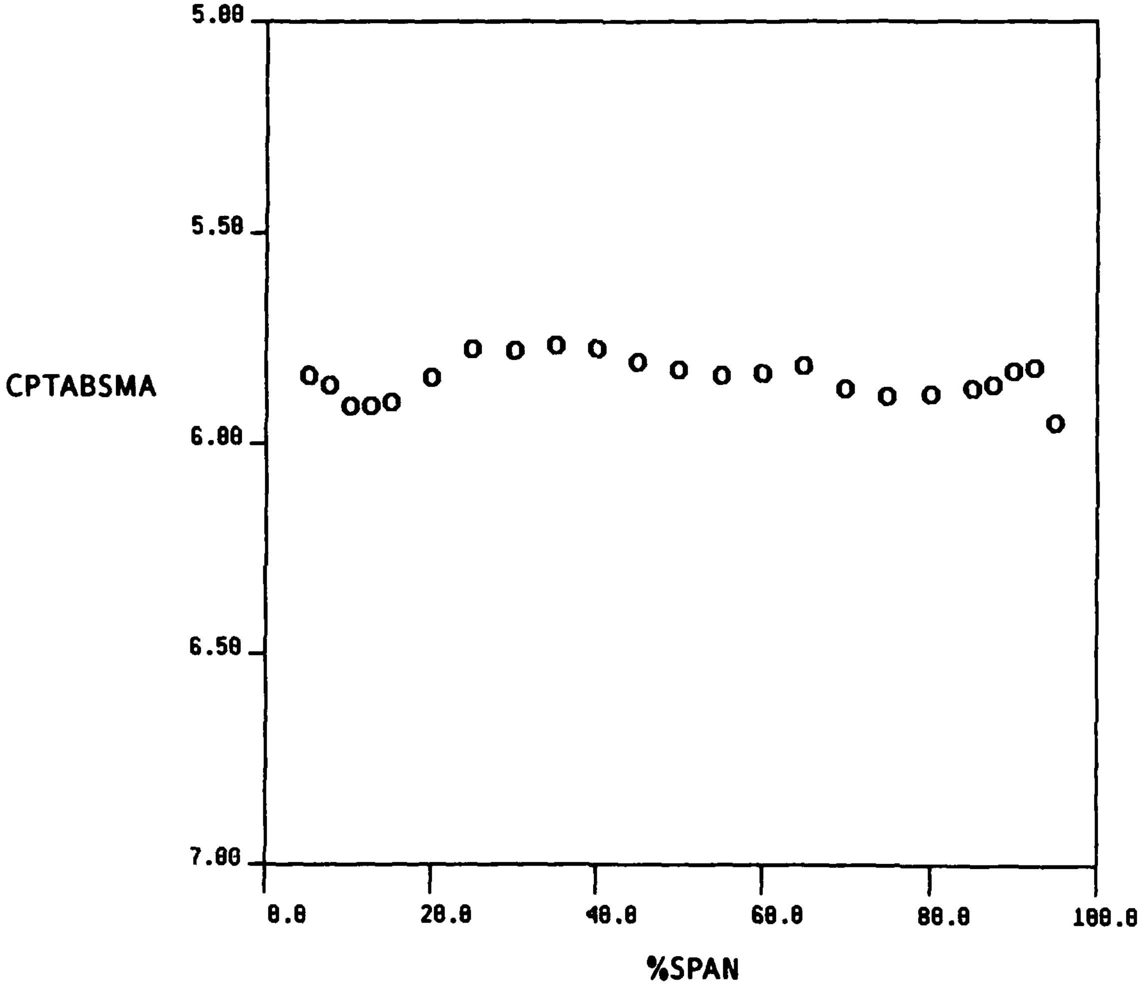

Fib. V–10b Second Stator Exit Results, Plane 4–Abs., Measured 14% aft, Absolute Total Pressure, Circumferential Mass Average

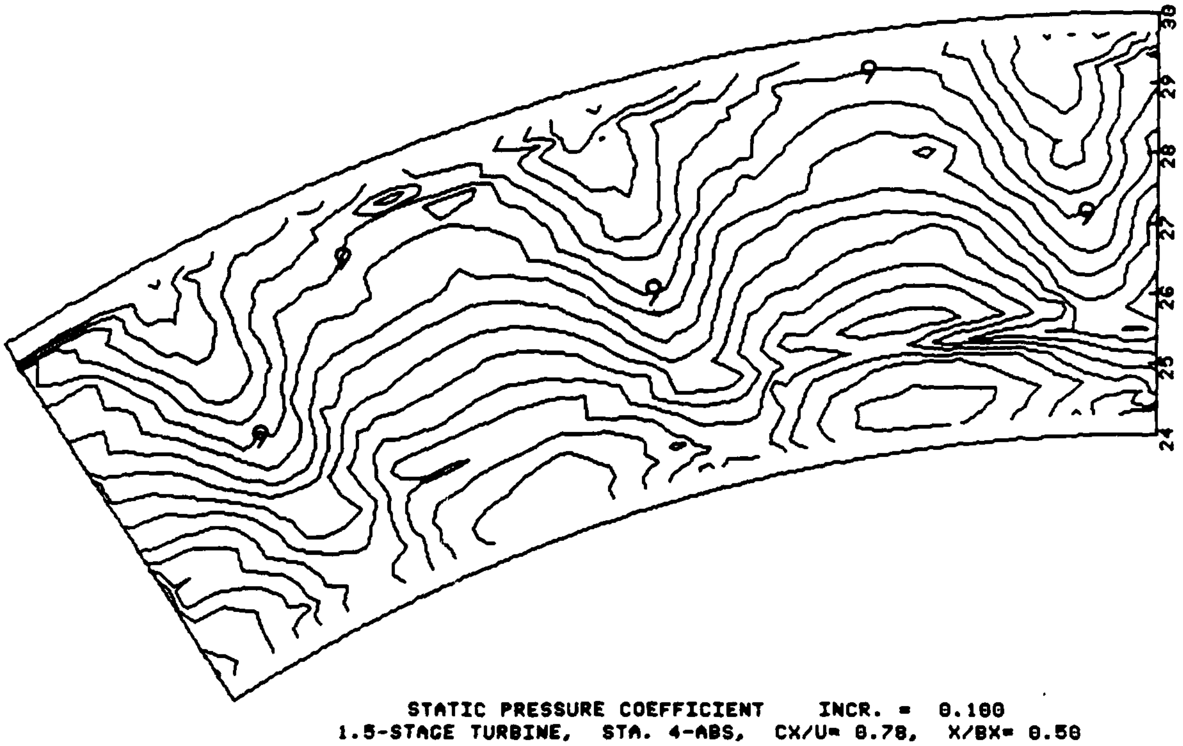

Fig. V–10c Second Stator Exit Results, Plane 4–Abs., Measured 14% aft, Static Pressure Contours, $\Delta CPS = 0.10$

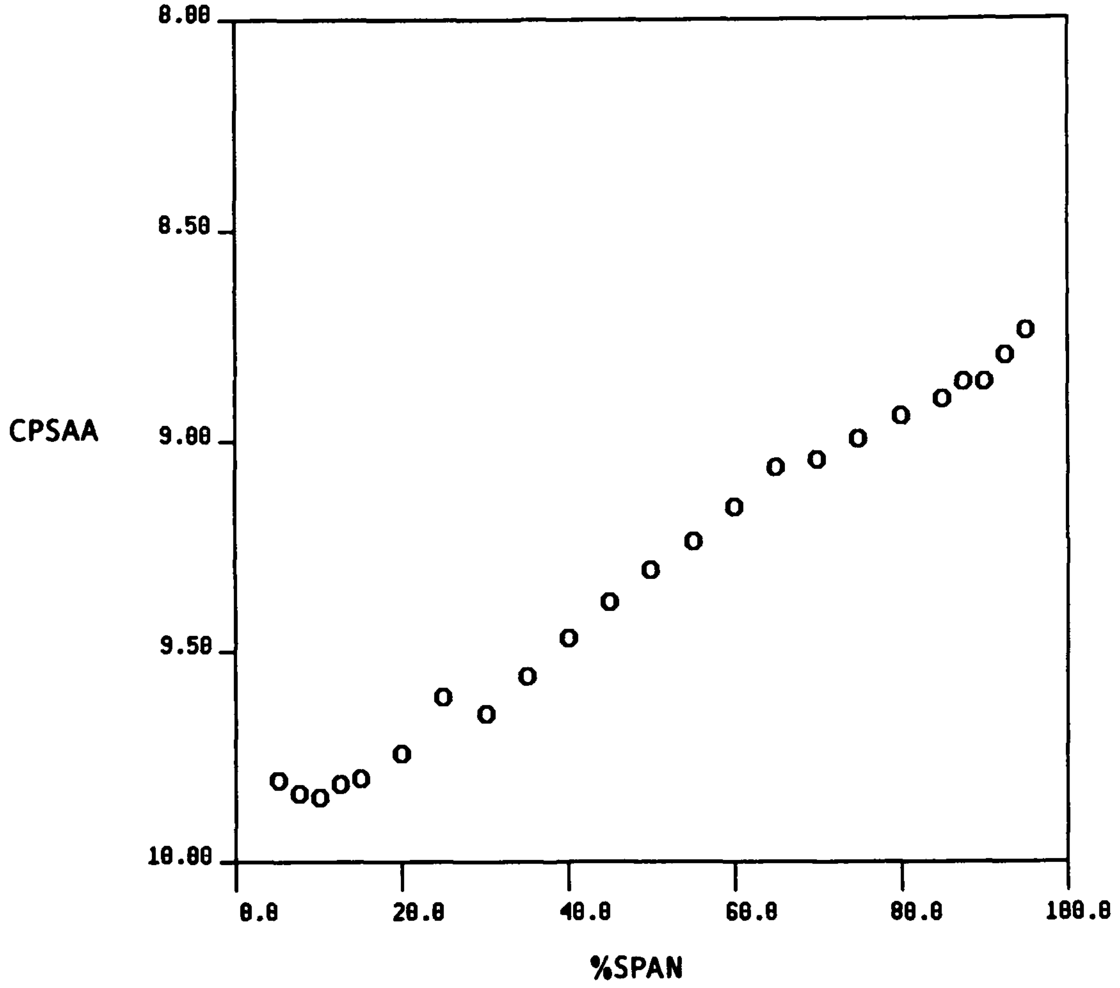

Fig. V–10d Second Stator Exit Results, Plane 4–Abs., Measured 14% aft, Static Pressure, Circumferential Area Average

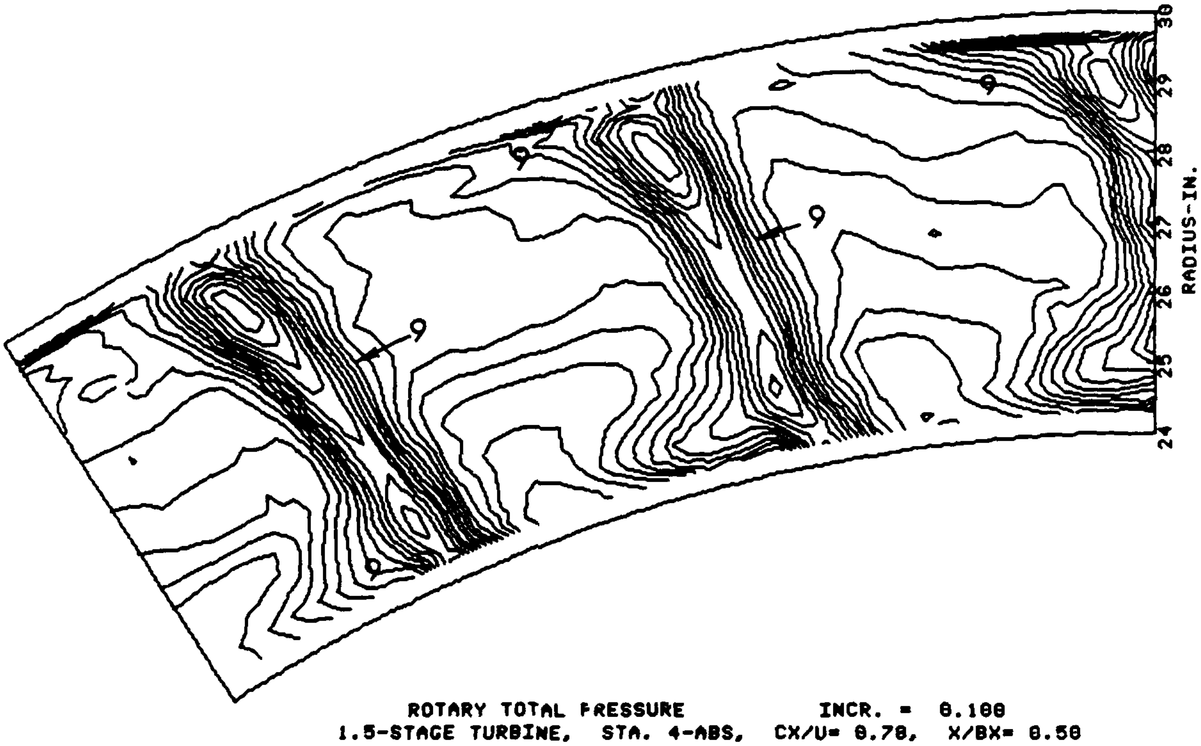

Fig. V–10e Second Stator Exit Results, Plane 4–Abs., Measured 14% aft, Rotary Total Pressure Contours, $\Delta CPTROT = 0.10$

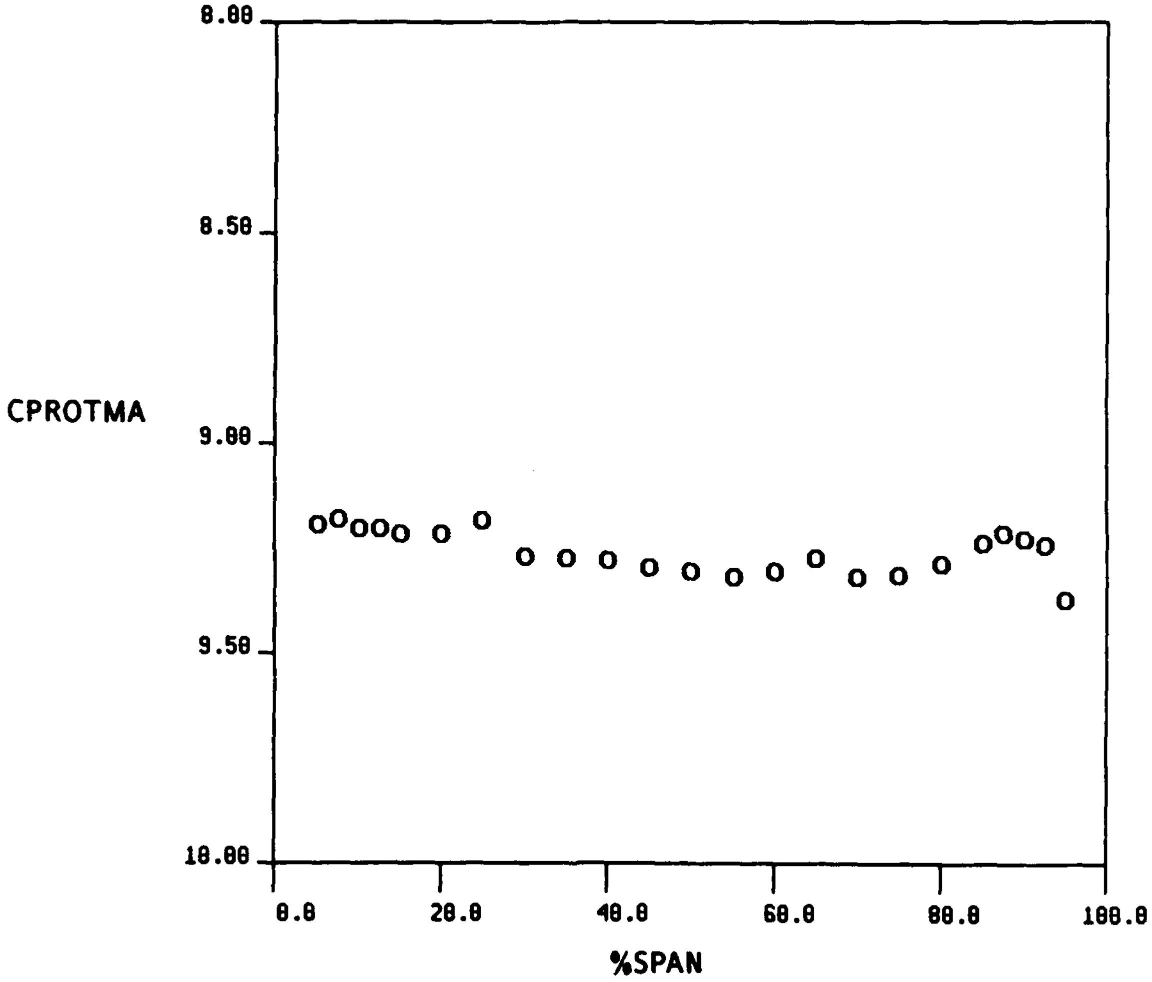

Fig. V–10f Second Stator Exit Results, Plane 4–Abs., Measured 14% aft, Rotary Total Pressure, Circumferential Mass Average

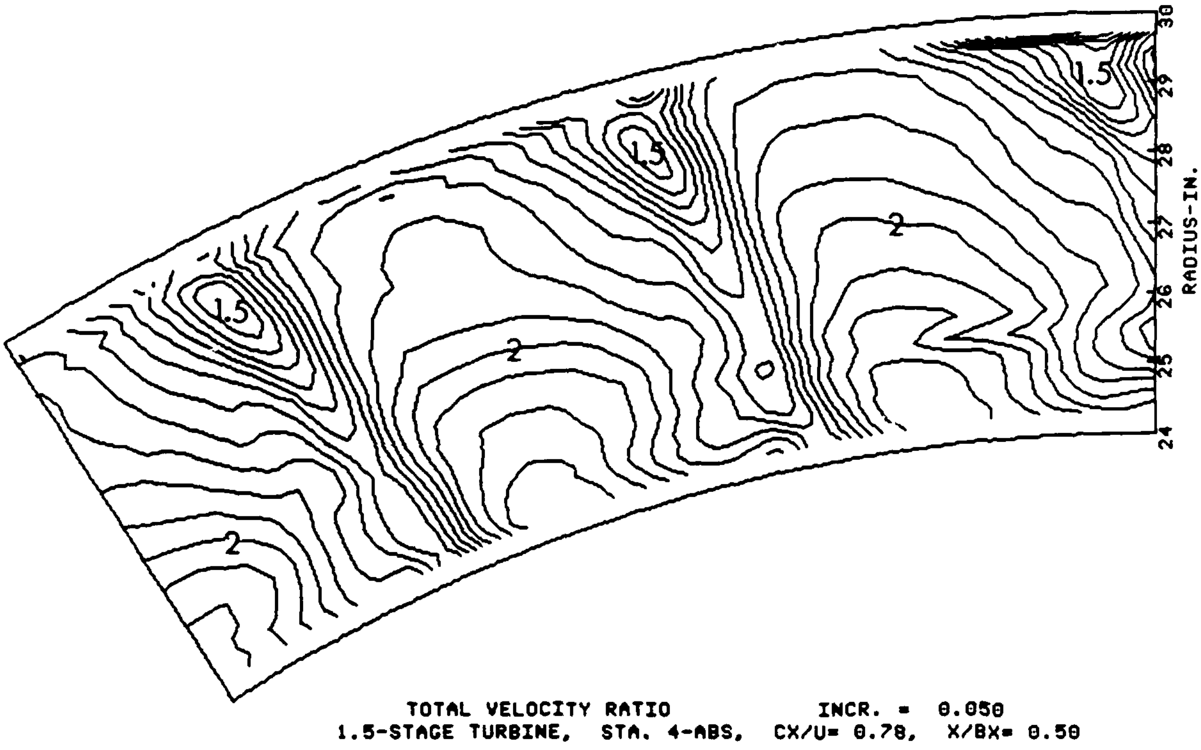

Fig. V–10g Second Stator Exit Results, Plane 4–Abs., Measured 14% aft, Absolute Velocity Contours, $\Delta(C/U_m) = 0.05$

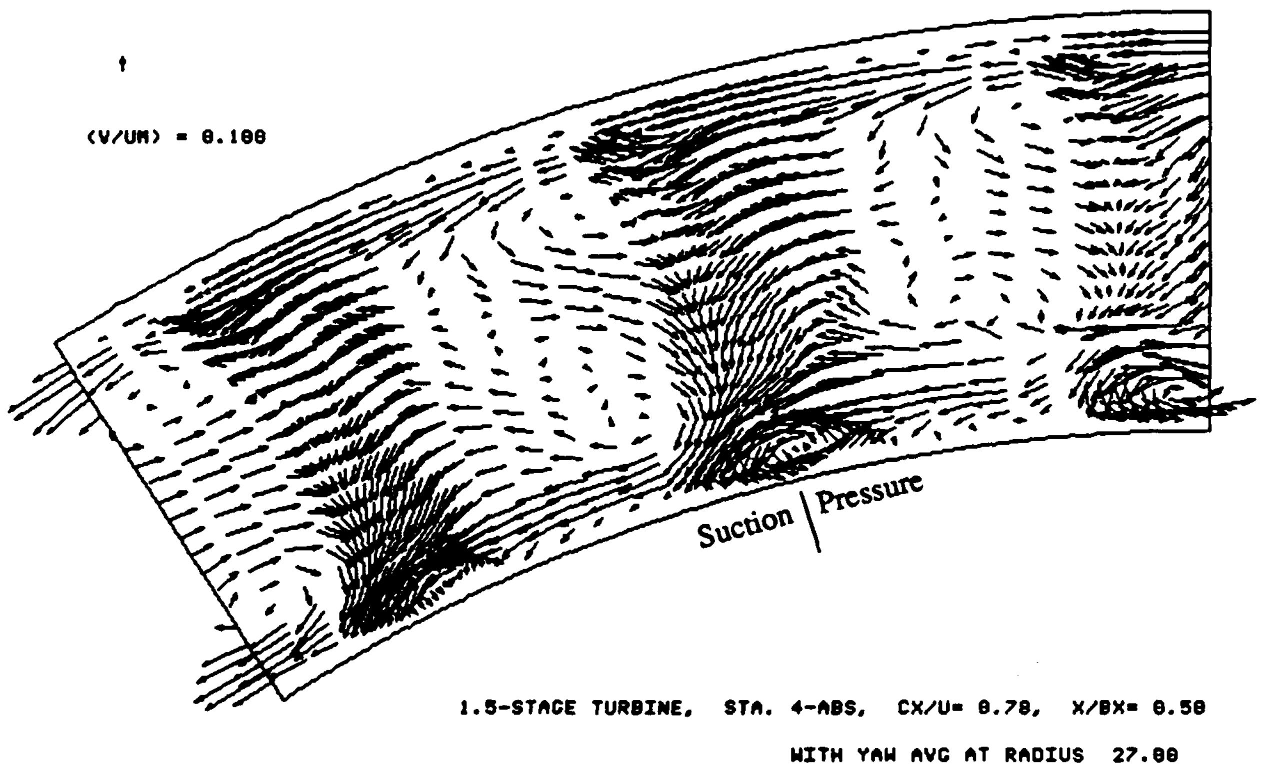

Fig. V–10h Second Stator Exit Results, Plane 4–Abs., Measured 14% aft, Secondary Flow with Average Yaw (Absolute) at 50% Span

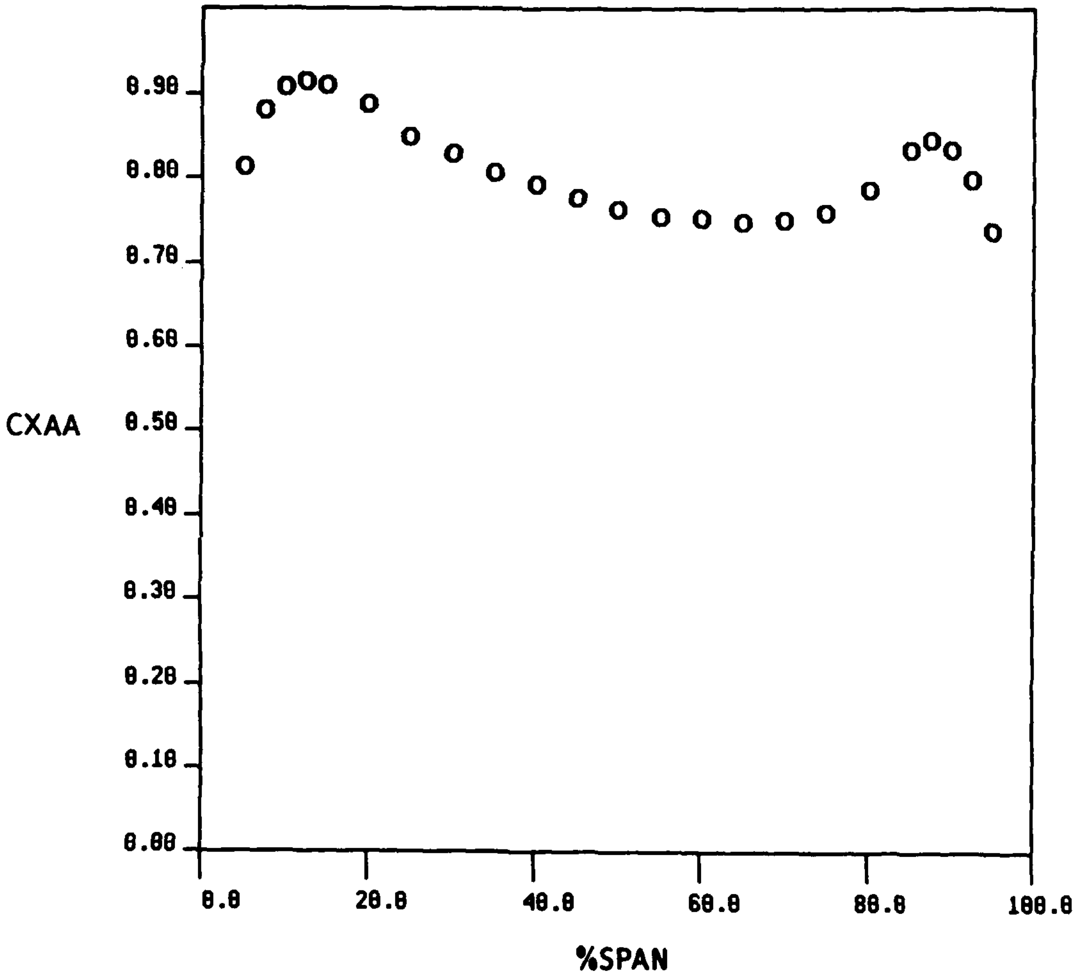

Fig. V–10i Second Stator Exit Results, Plane 4–Abs., Measured 14% aft, Axial Velocity (C_x/U_m), Circumferential Area Average

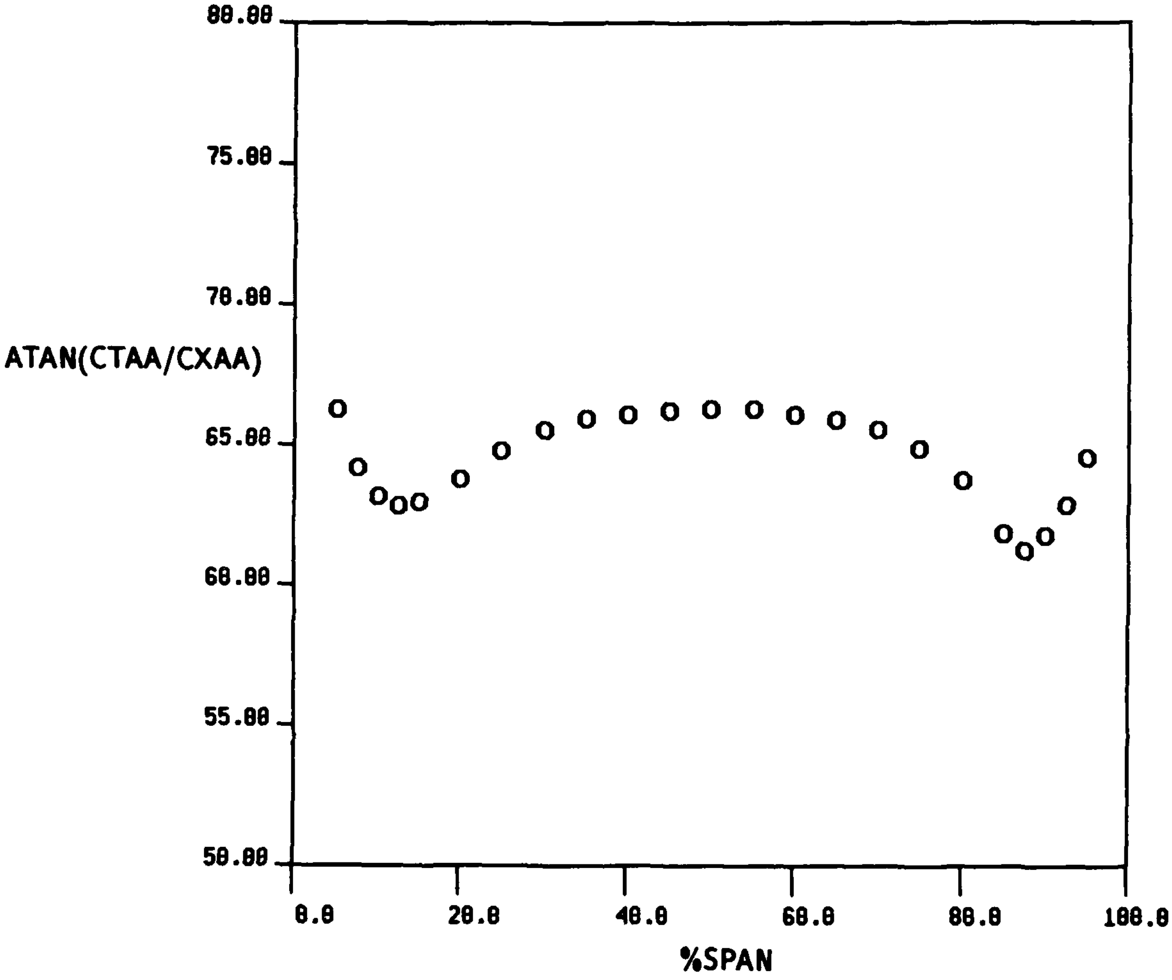

Fig. V–10j Second Stator Exit Results, Plane 4–Abs., Measured 14% aft, Absolute Flow Angle (Arctan[CTAA/CXAA])

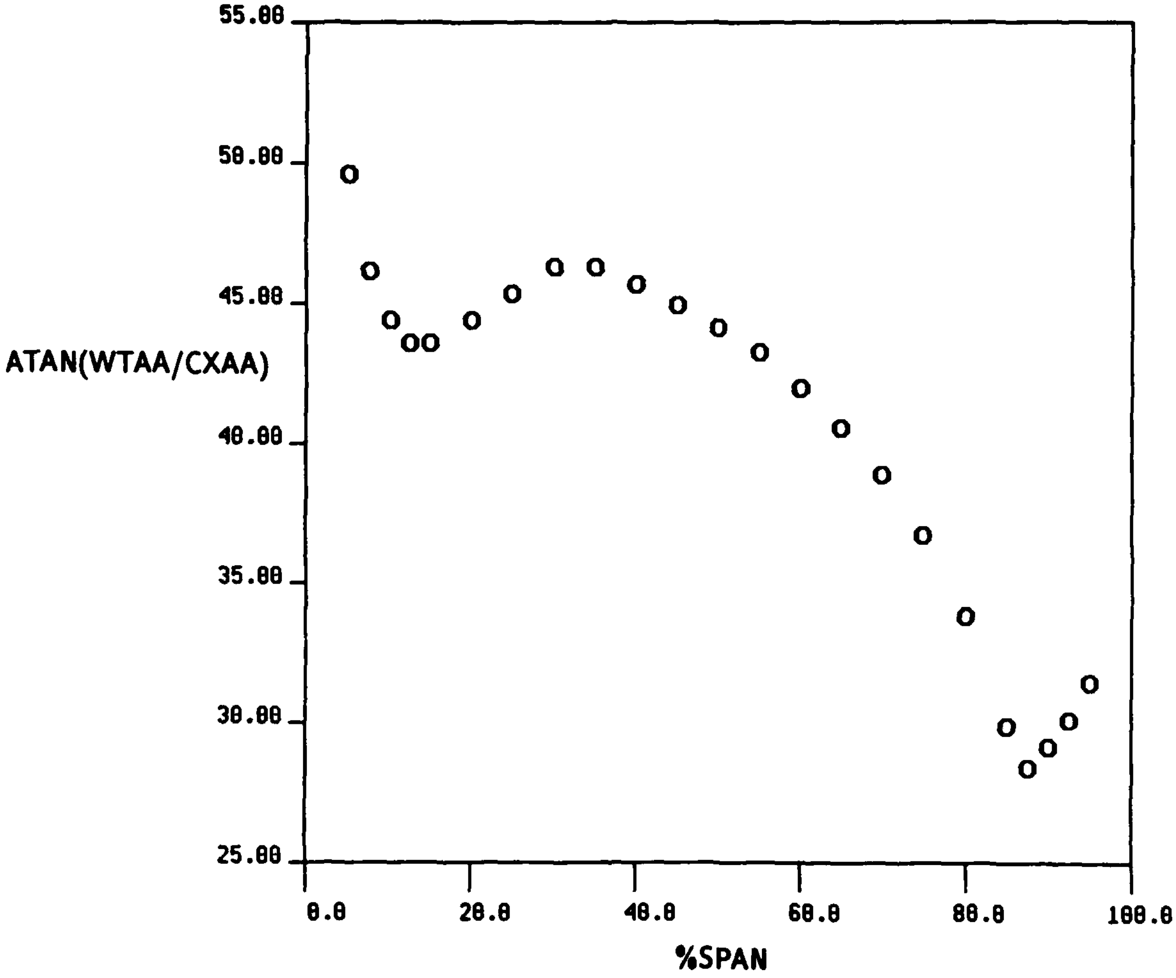

Fig. V–10k Second Stator Exit Results, Plane 4–Abs., Measured 14% aft, Relative Flow Angle (Arctan[WTAA/CXAA])

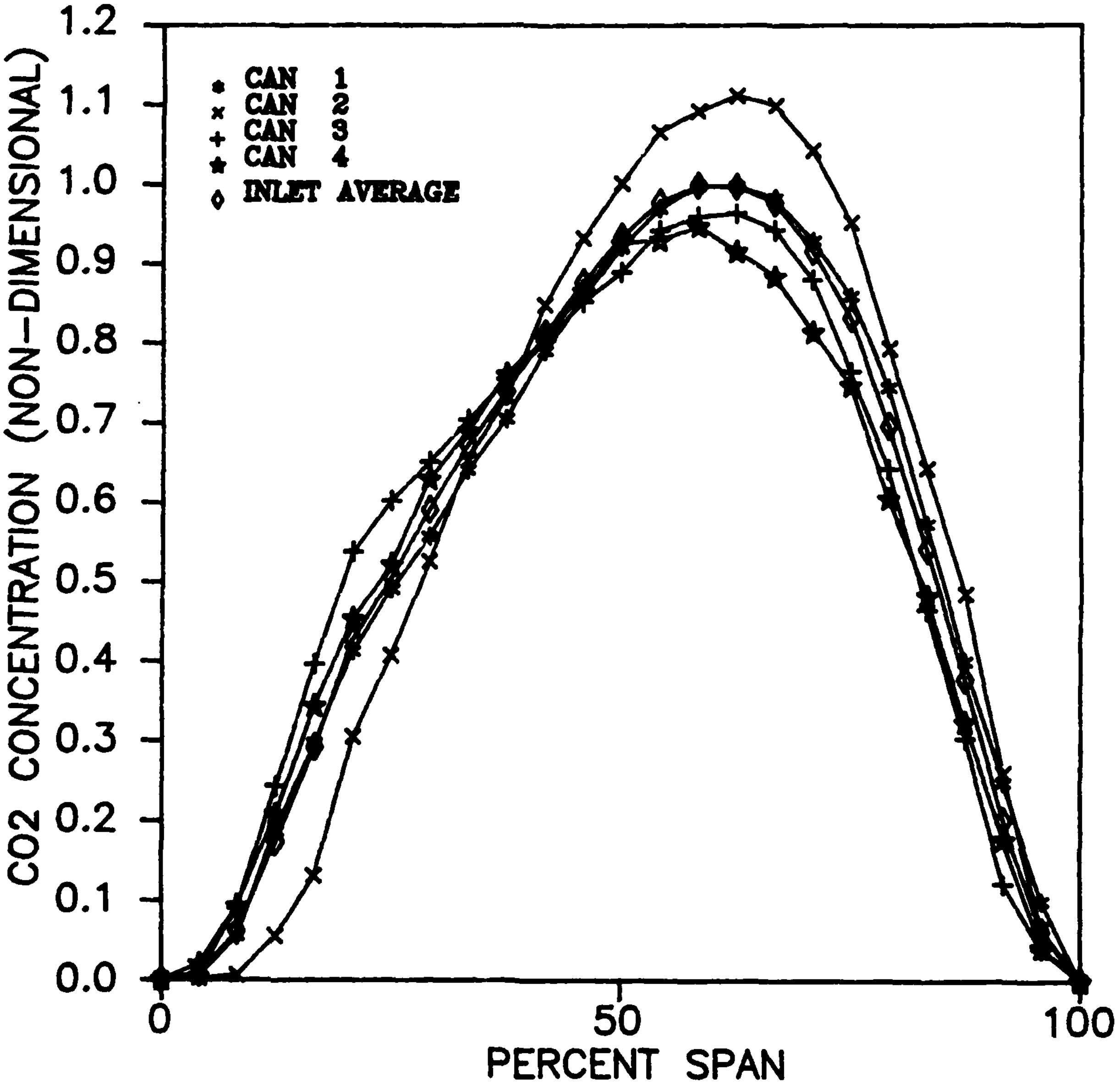

Fig. V–11 Inlet, Plane 1, Trace Gas Concentration Profiles

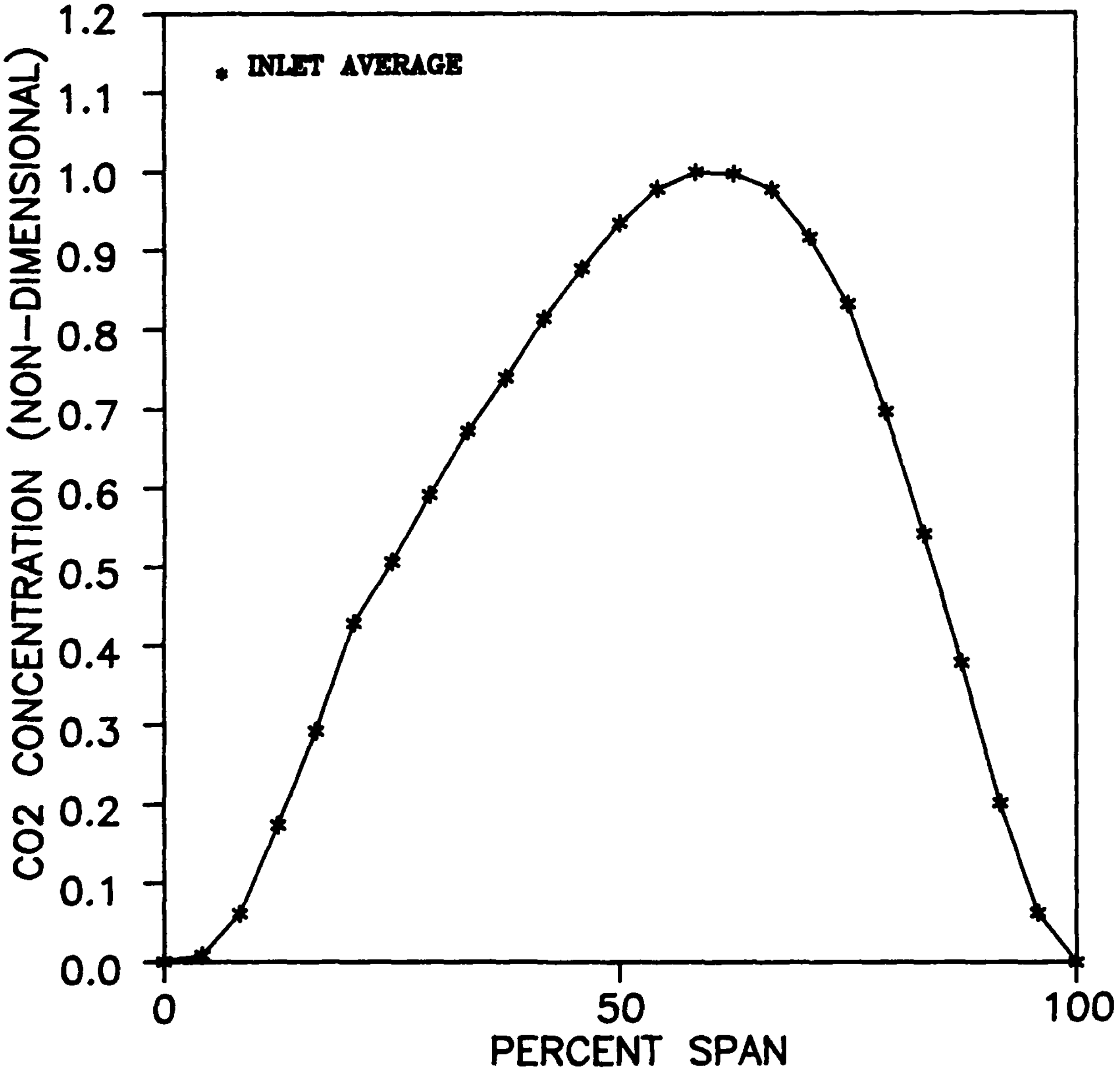

Fig. V–12 Averaged Inlet, Plane 1, Trace Gas Concentration Profile

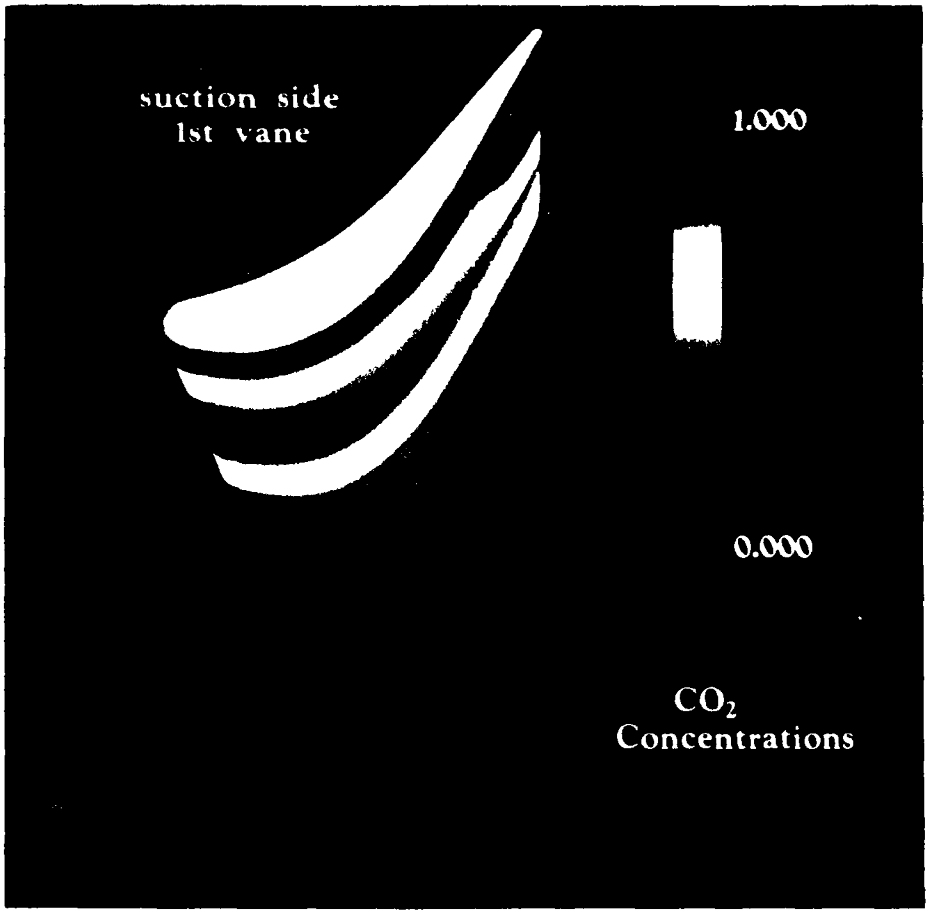

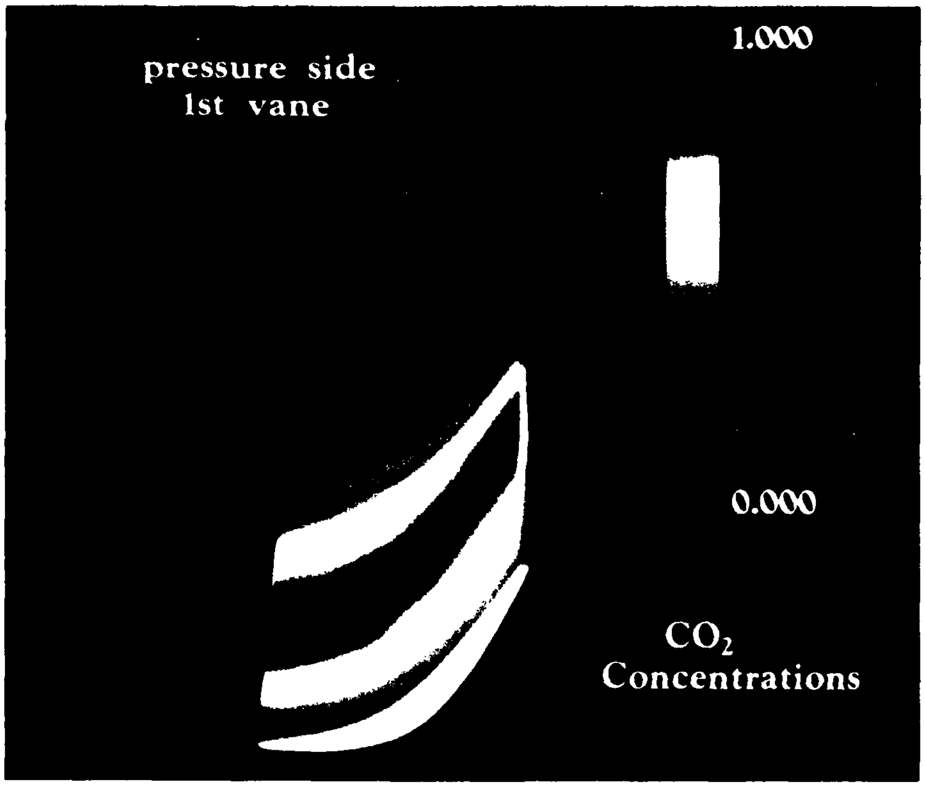

Fig. V–13 First Stator Surface Trace Gas Concentration

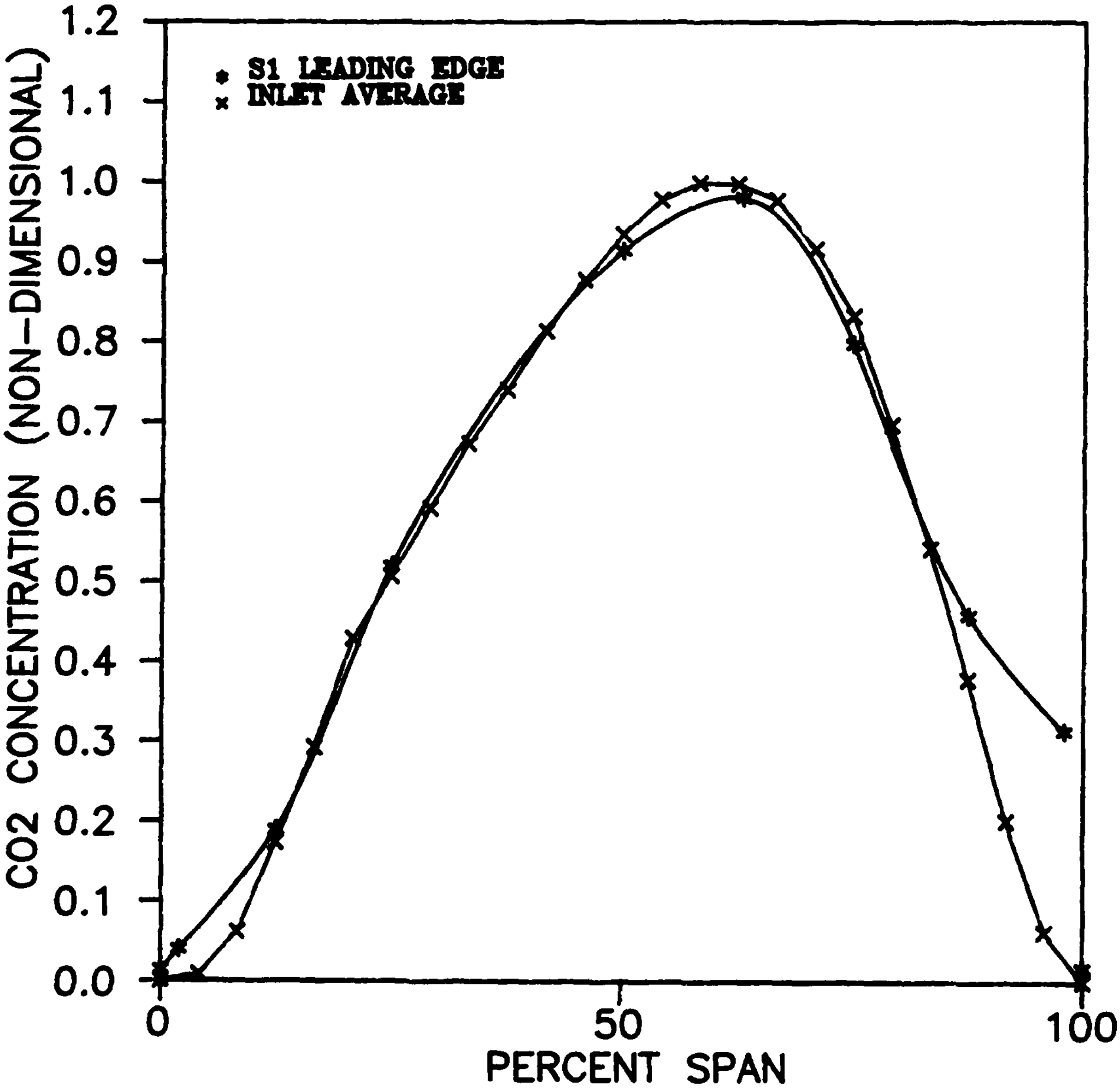

Fig. V–14 First Stator Leading Edge Trace Gas Concentration Profile

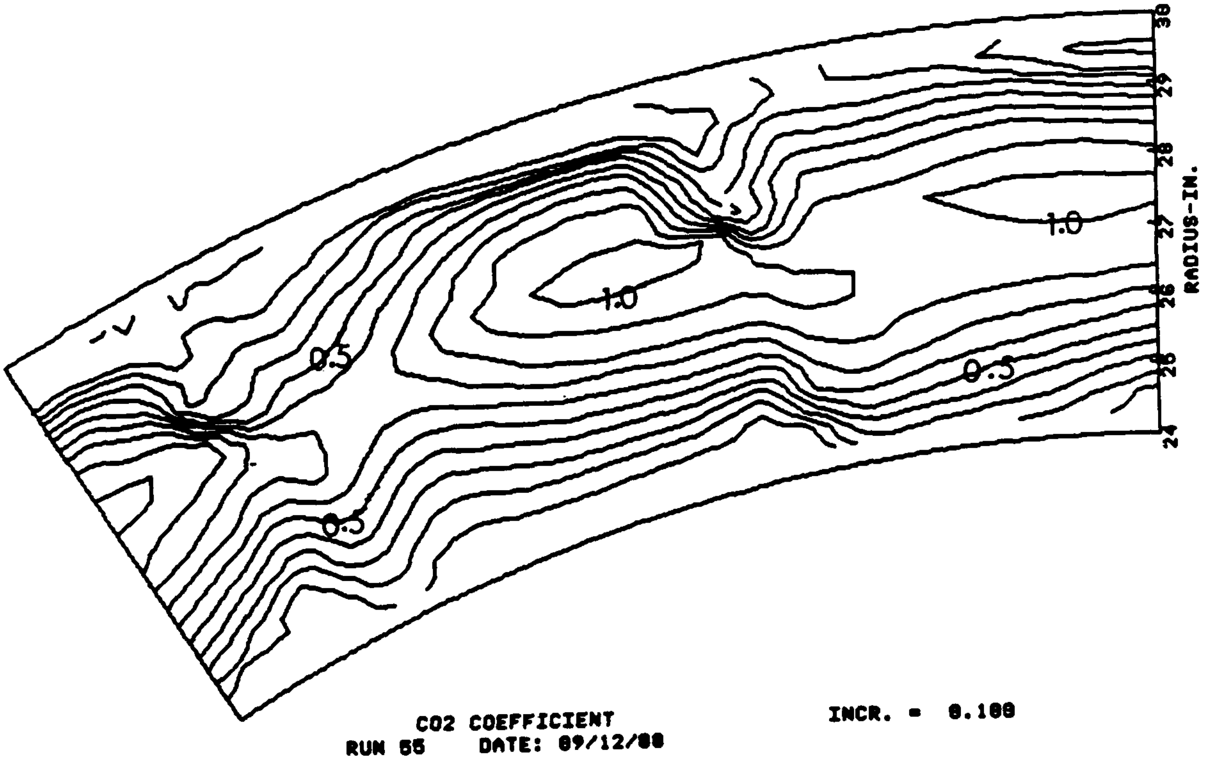

Fig. V–15 First Stator Exit, Plane 2, Trace Gas Contours, $\Delta F = 0.1$

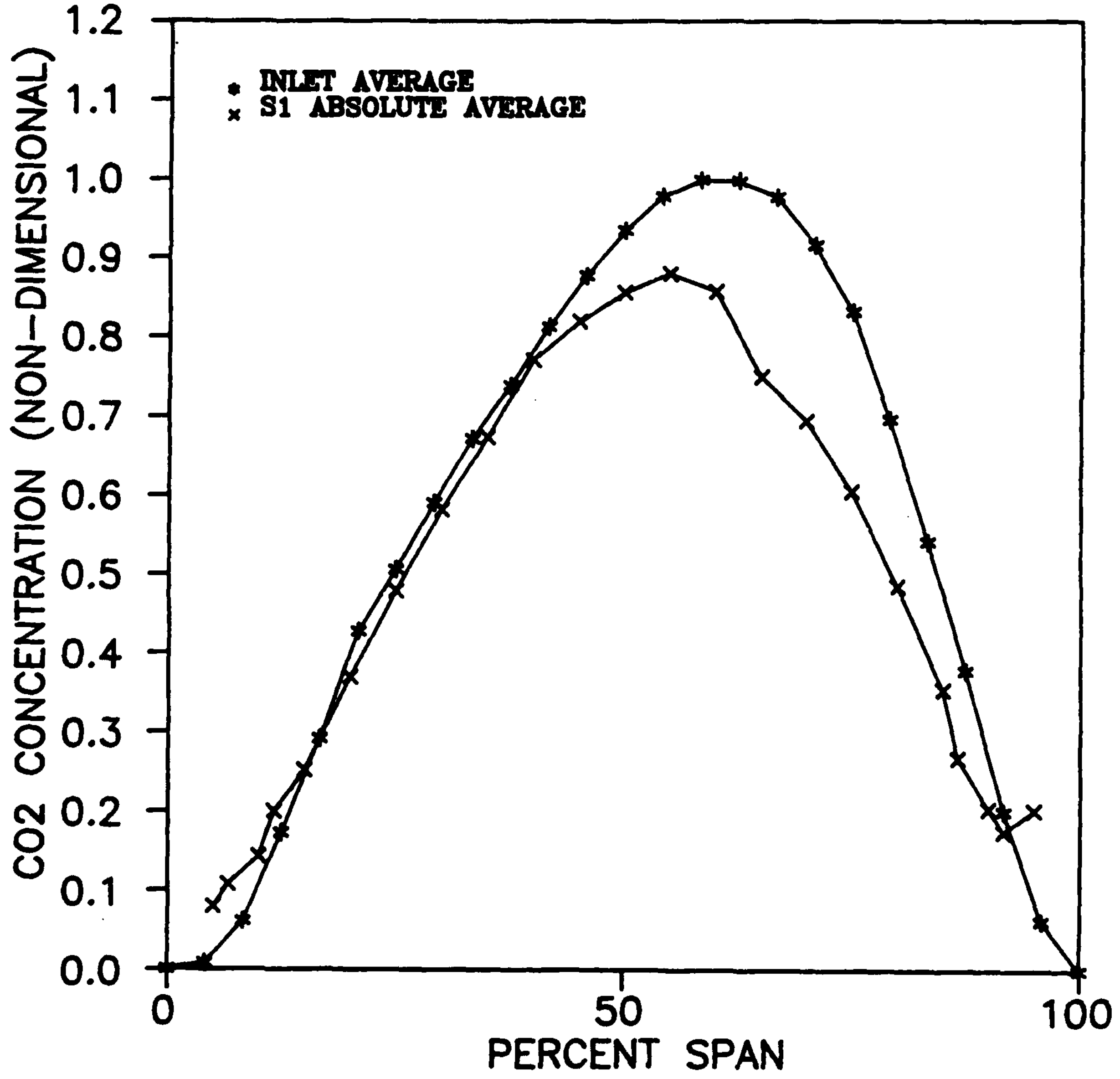

Fig. V–16 First Stator Exit, Plane 2, Trace Gas Average Profile

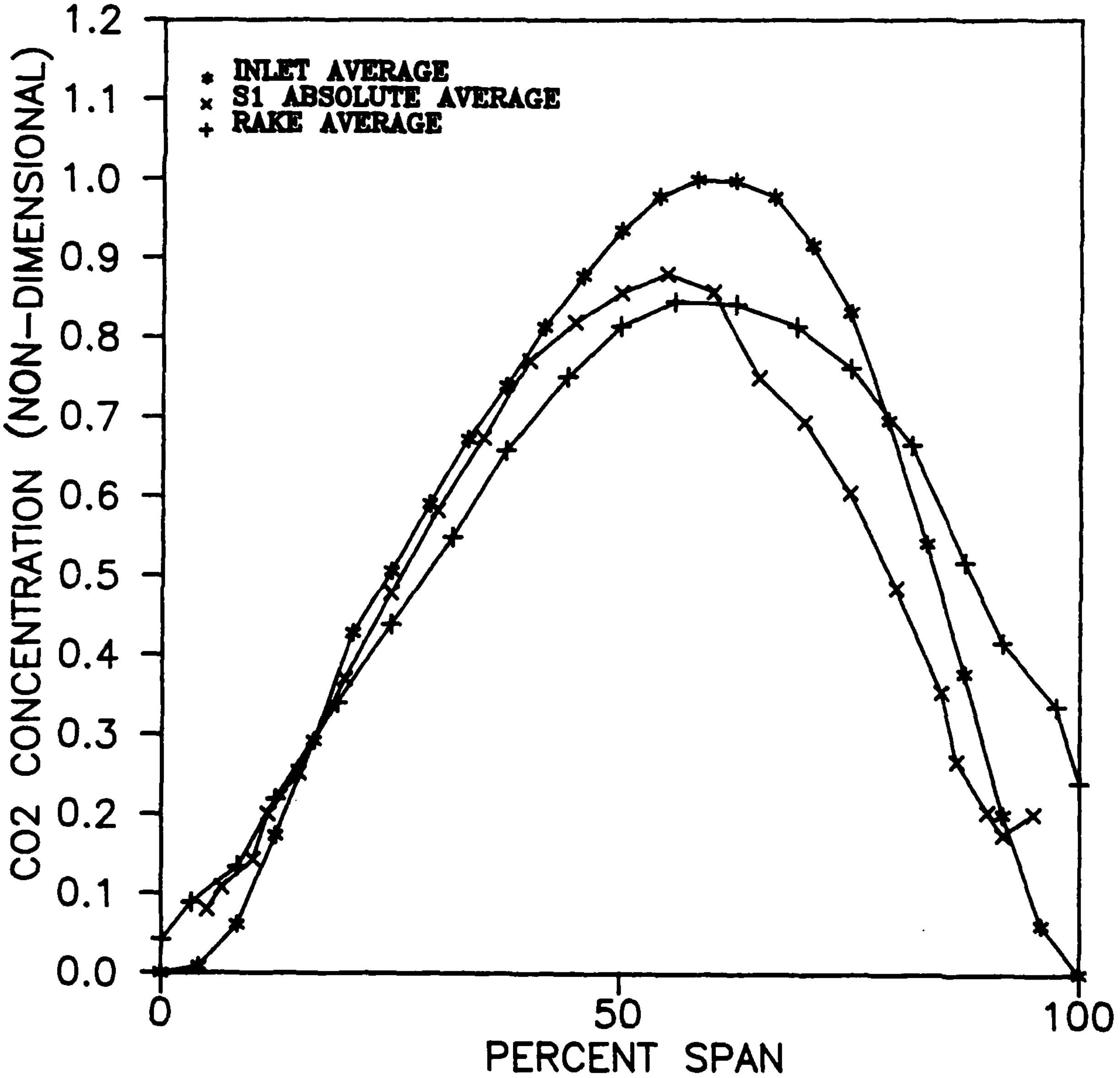

Fig. V–17 Comparison of the Average Inlet (Plane 1) Profile with the Averaged Profile at Plane 2 and the Rotor Rake

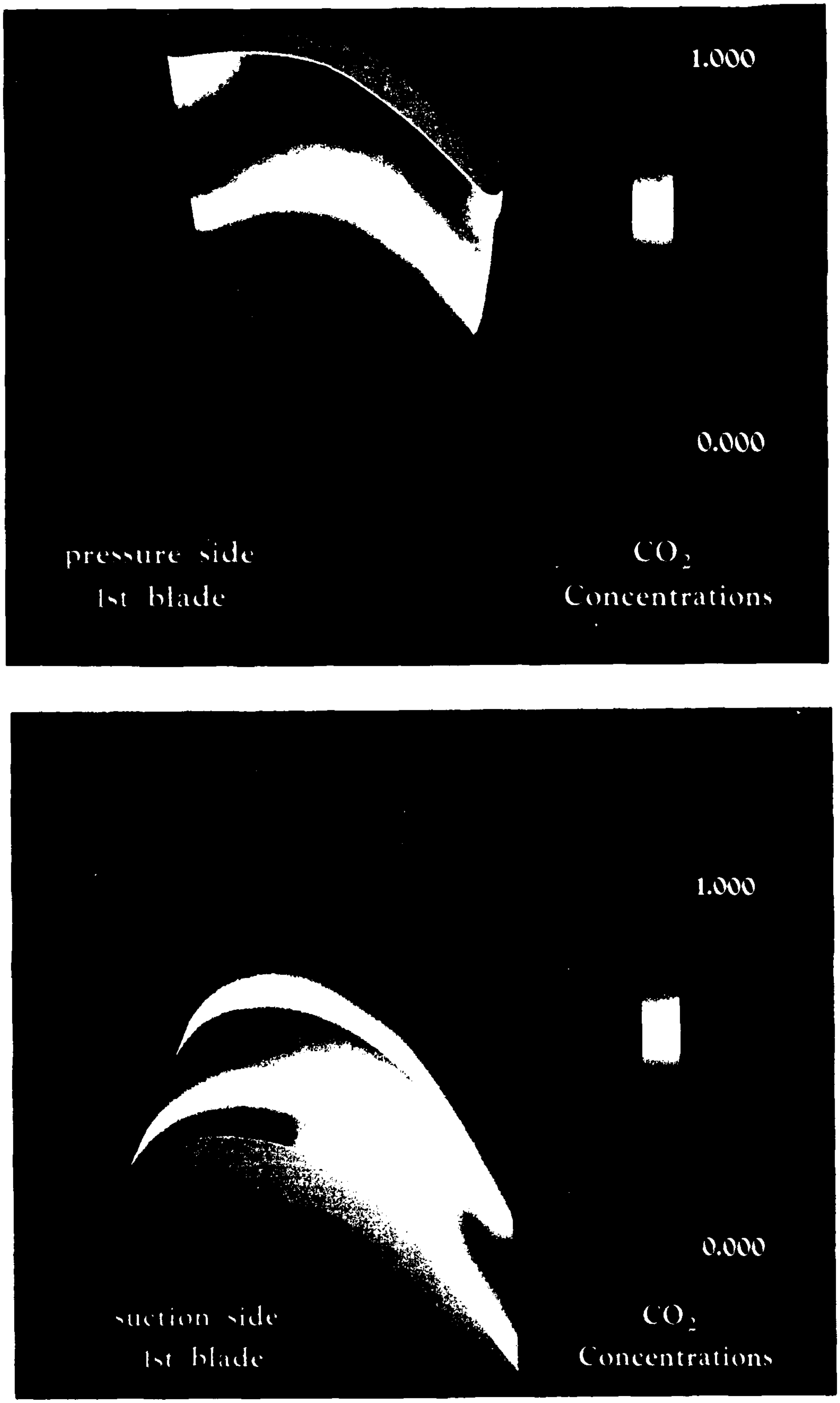

Fig. V–18 Rotor Surface Trace Gas Concentration

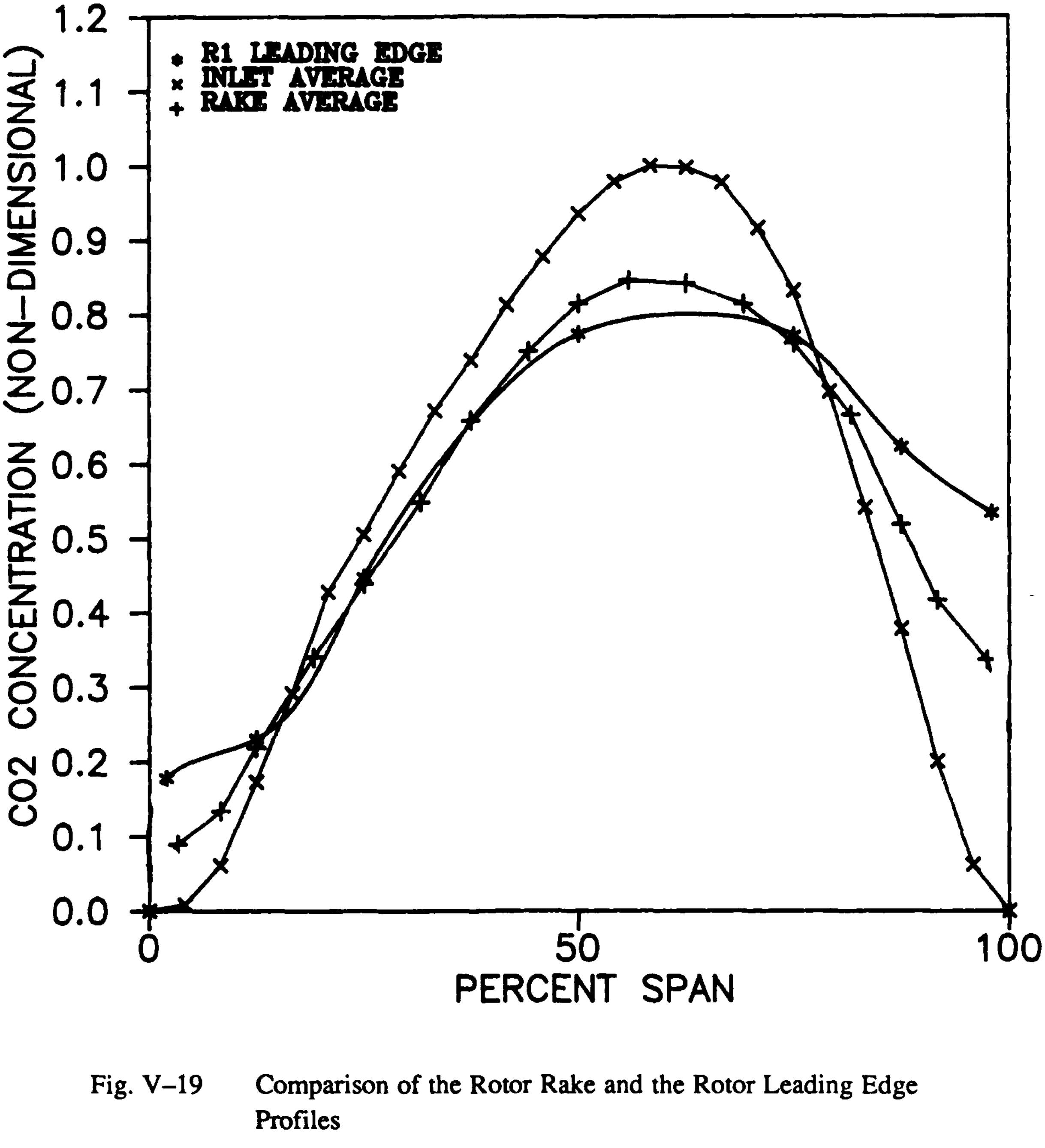

Fig. V-19 Comparison of the Rotor Rake and the Rotor Leading Edge Profiles

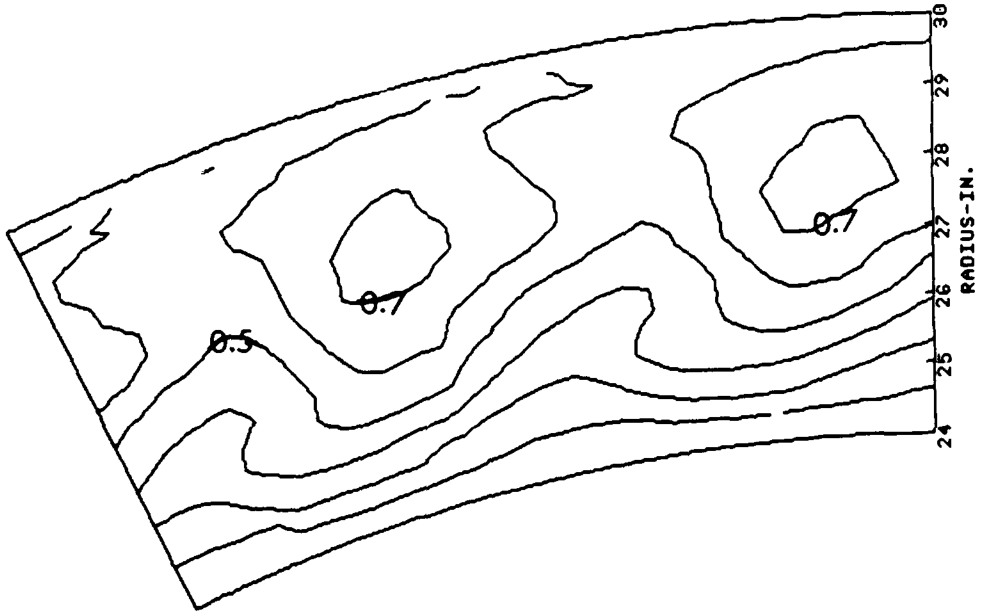

CO2 COEFFICIENT INCR. = 0.100
RUN 60 & 61 DATE: 10/18/88

Fig. V–20 Rotor Exit Relative, Plane 3–Relative, Trace Gas Contours, $\Delta F = 0.1$

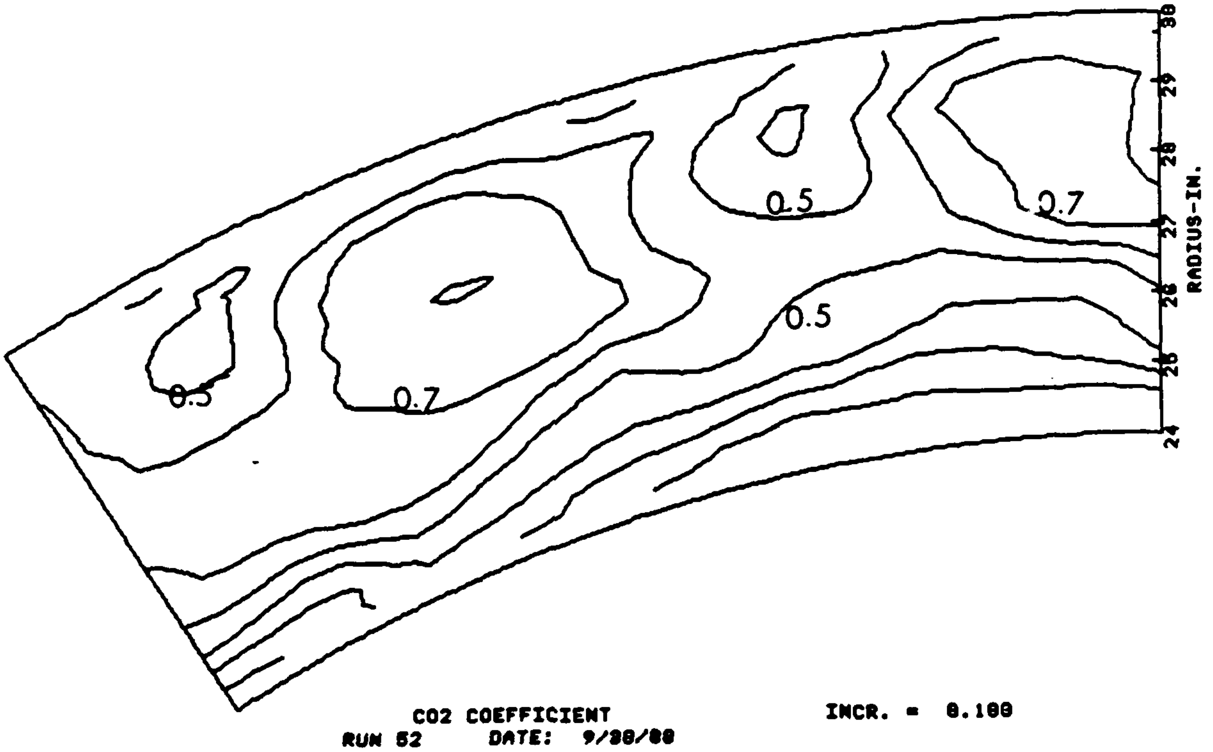

Fig. V–21 Rotor Exit Absolute, Plane 3–Absolute, Trace Gas Contours, $\Delta F = 0.1$

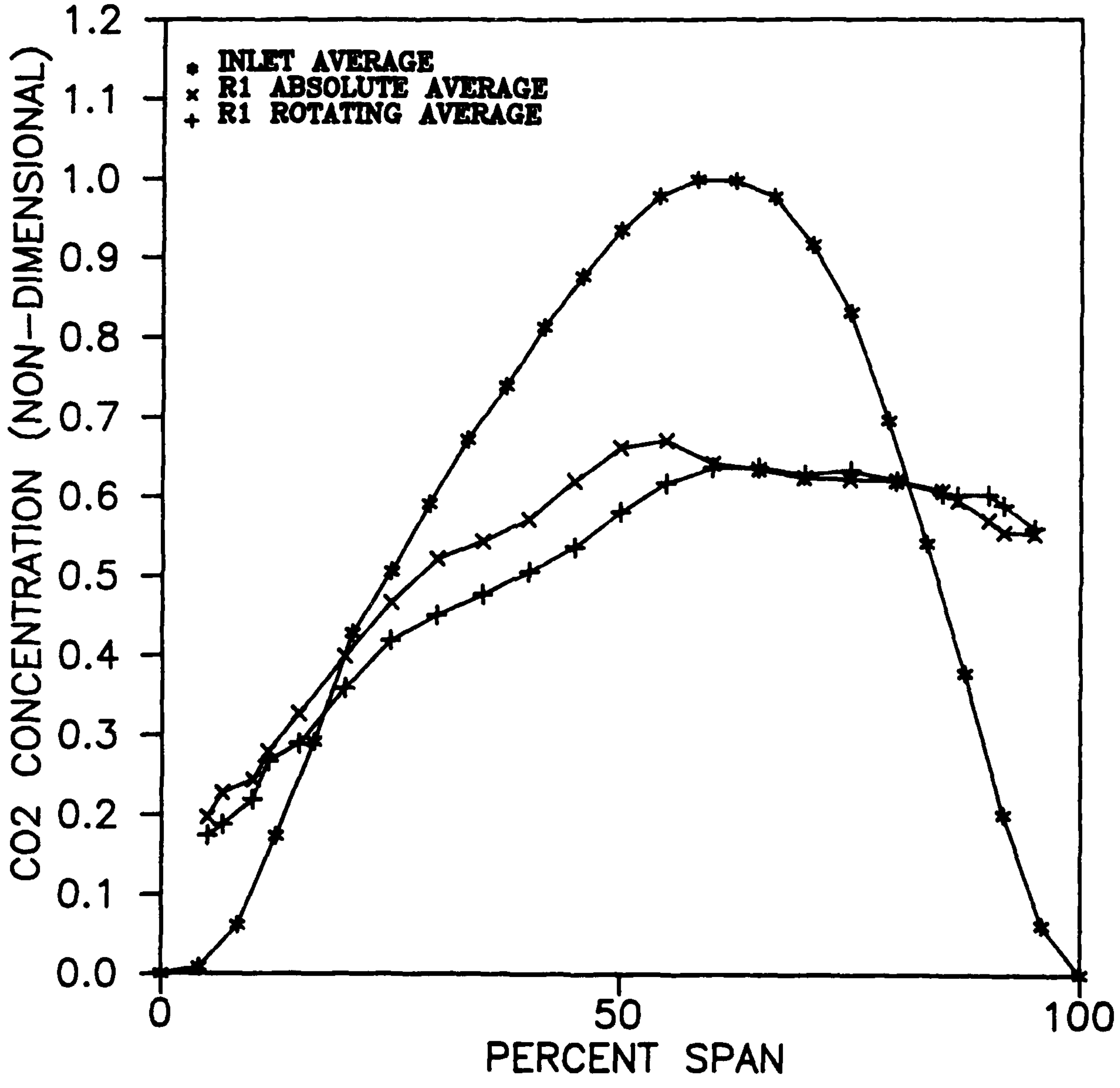

Fig. V–22 Rotor Exit (Plane 3–Relative and Absolute)
Trace Gas Average Profiles

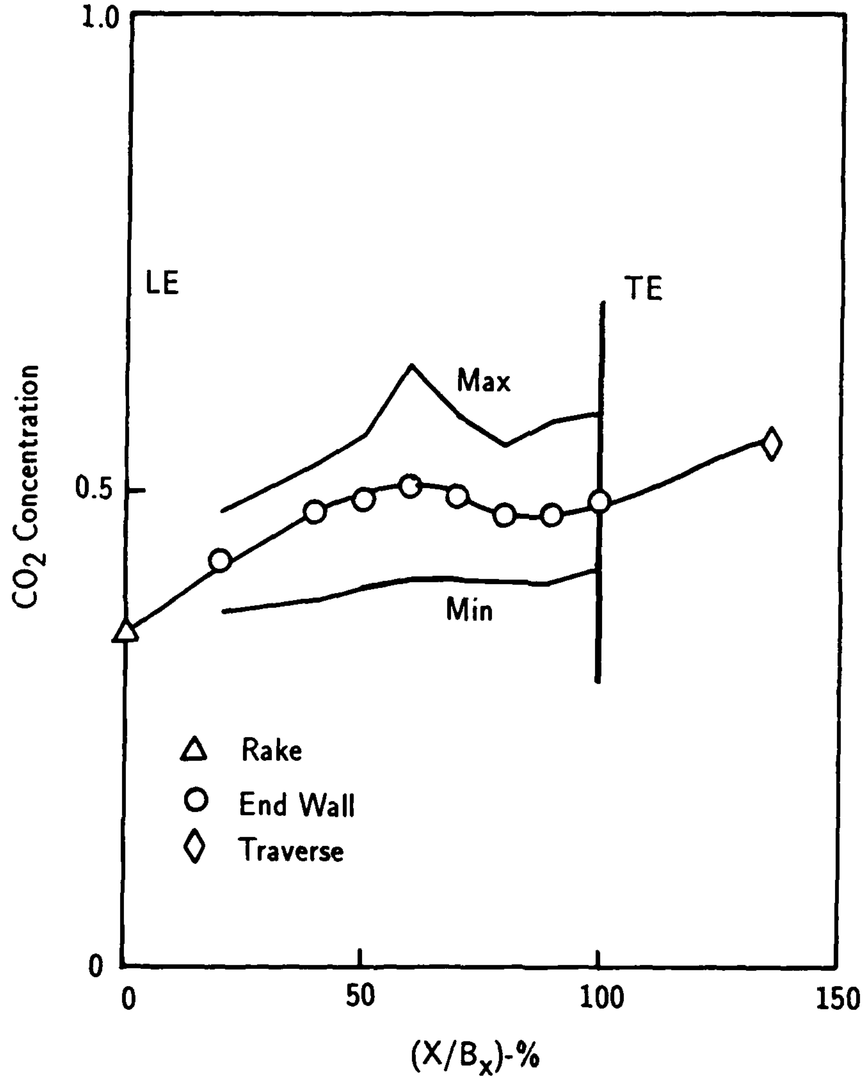

Fig. V–23 Rotor Shroud Trace Gas Concentration

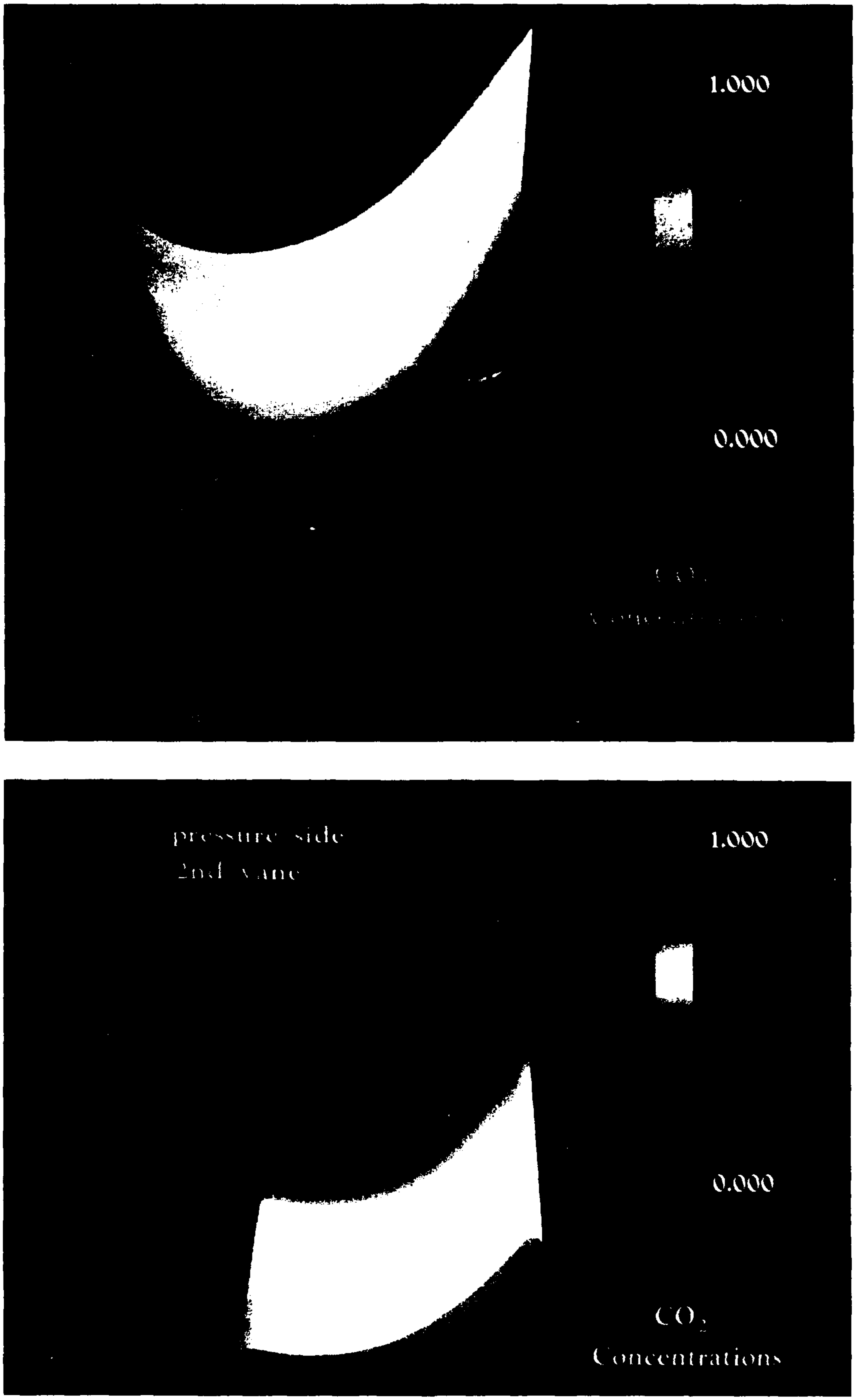

Fig. V–24 Second Stator Surface Trace Gas Concentration

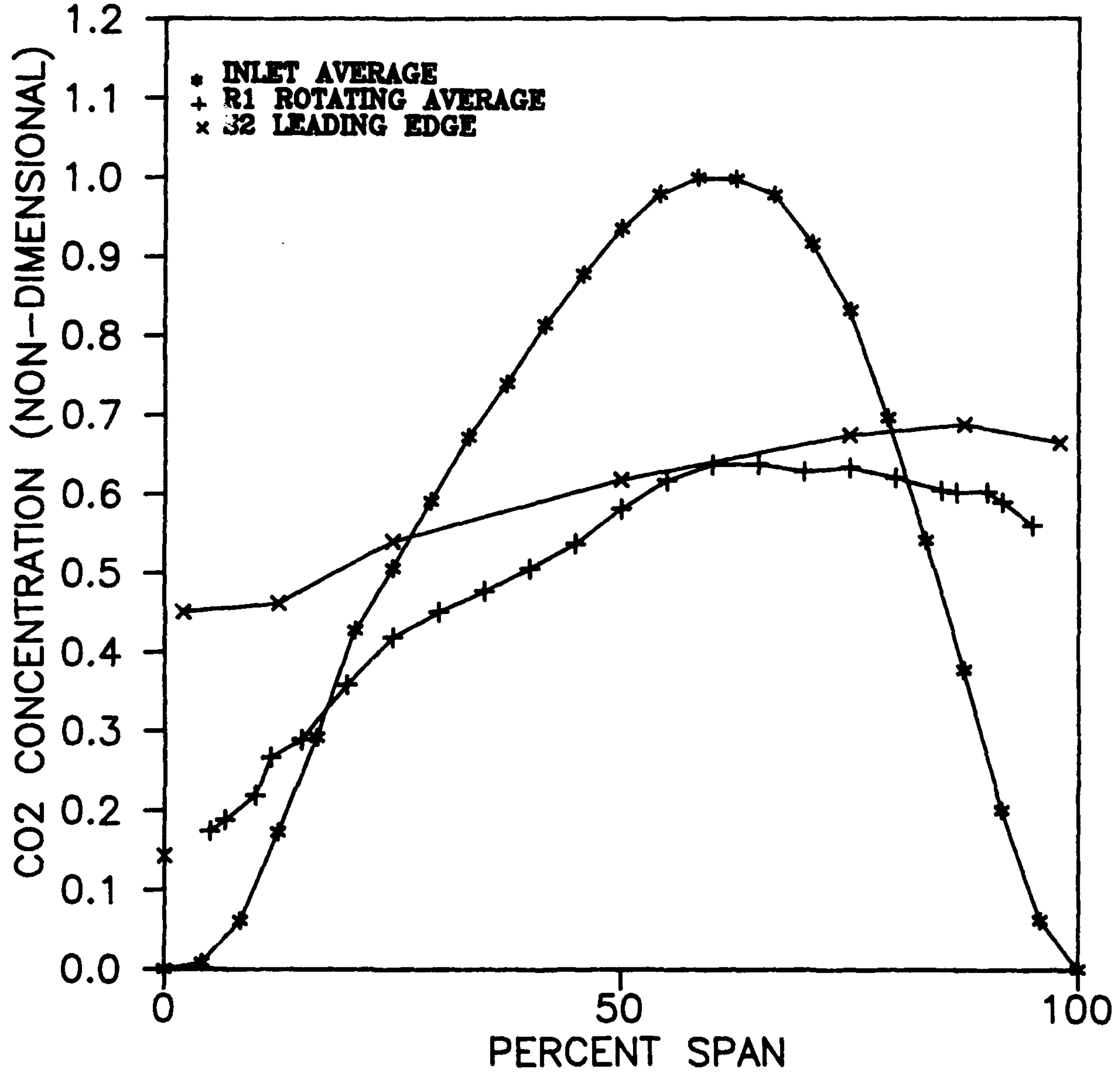

Fig. V–25 Comparison of the Second Stator Leading Edge Concentration Profile, the Rotor Rake Profile and the Inlet Profile

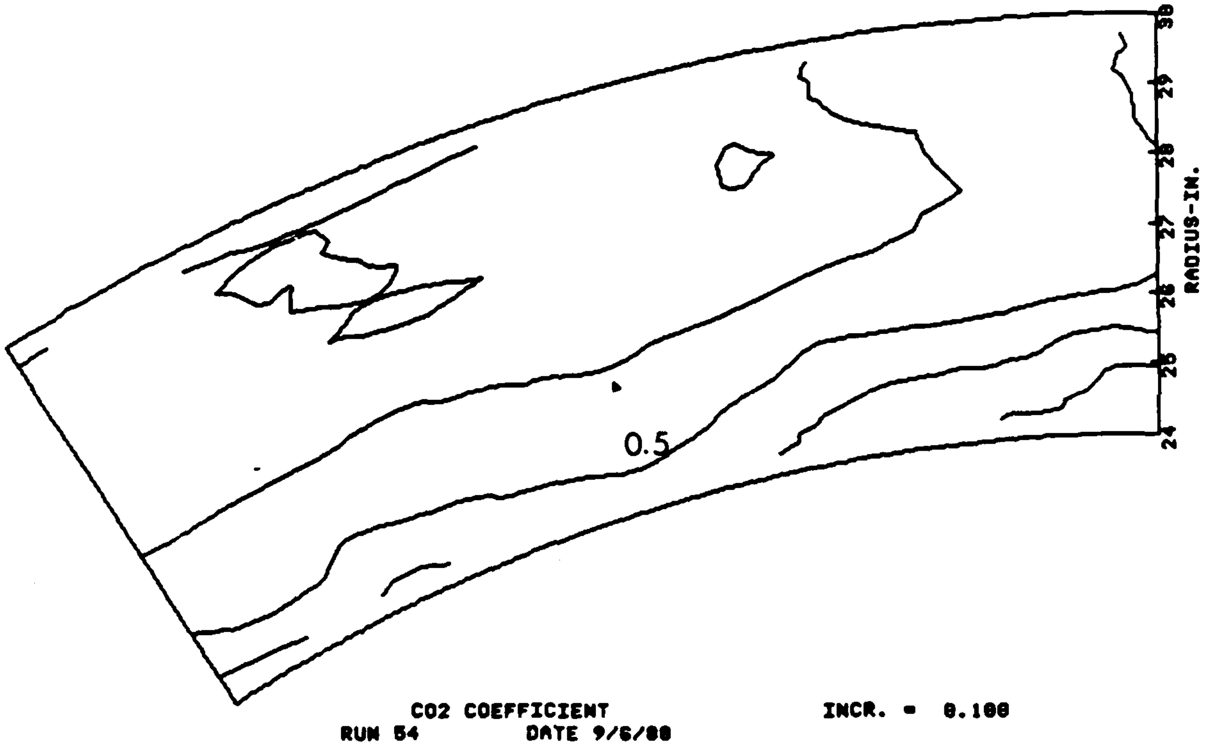

Fig. V–26 Second Stator Exit, Plane 4, Trace Gas Contours, $\Delta F = 0.1$

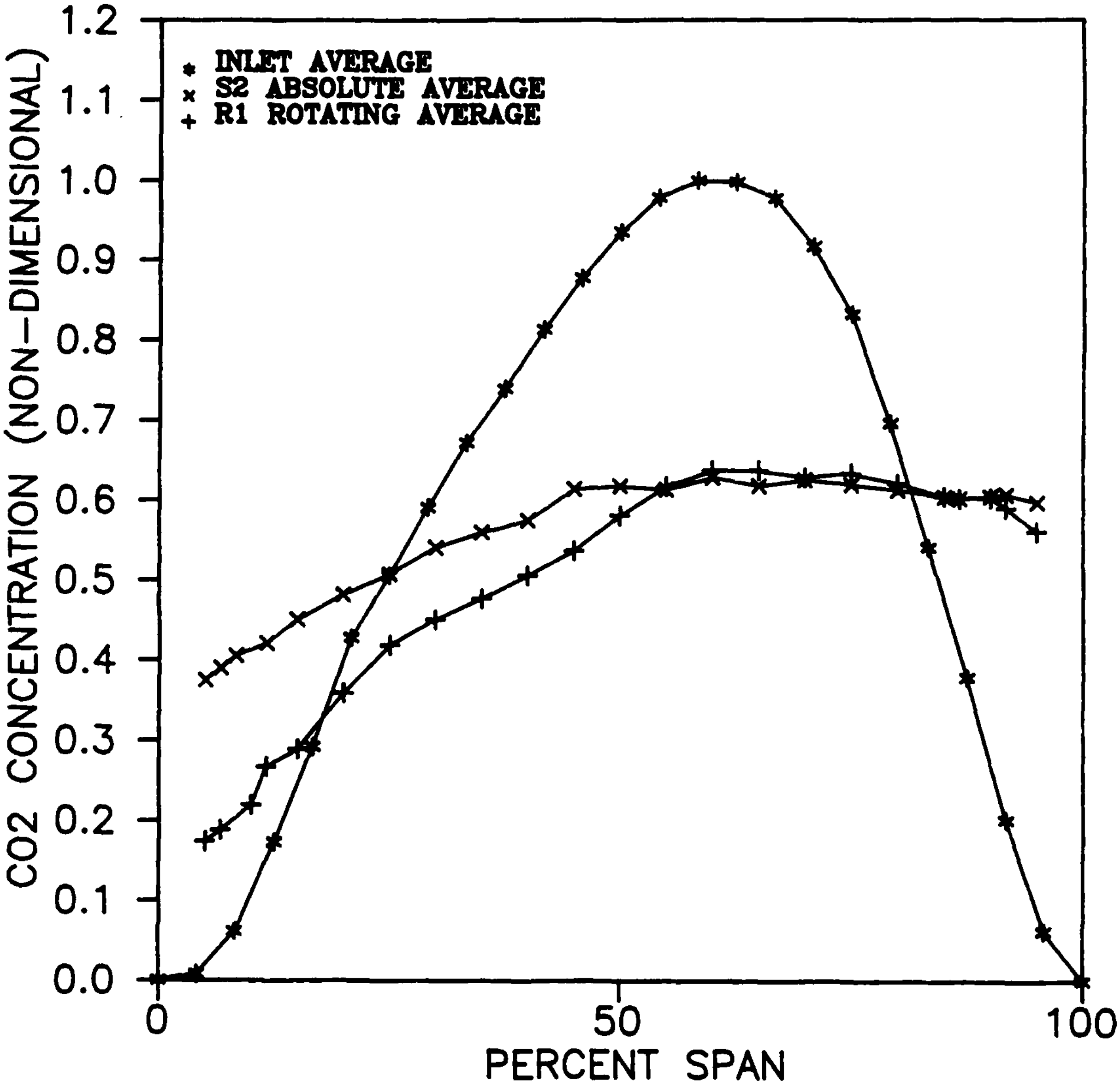

Fig. V–27 Second Stator Exit (Plane 4) Trace Gas Average Profile Compared with the Rotor Exit Average (Plane 2–Relative) and the Inlet Profile (Plane 1)

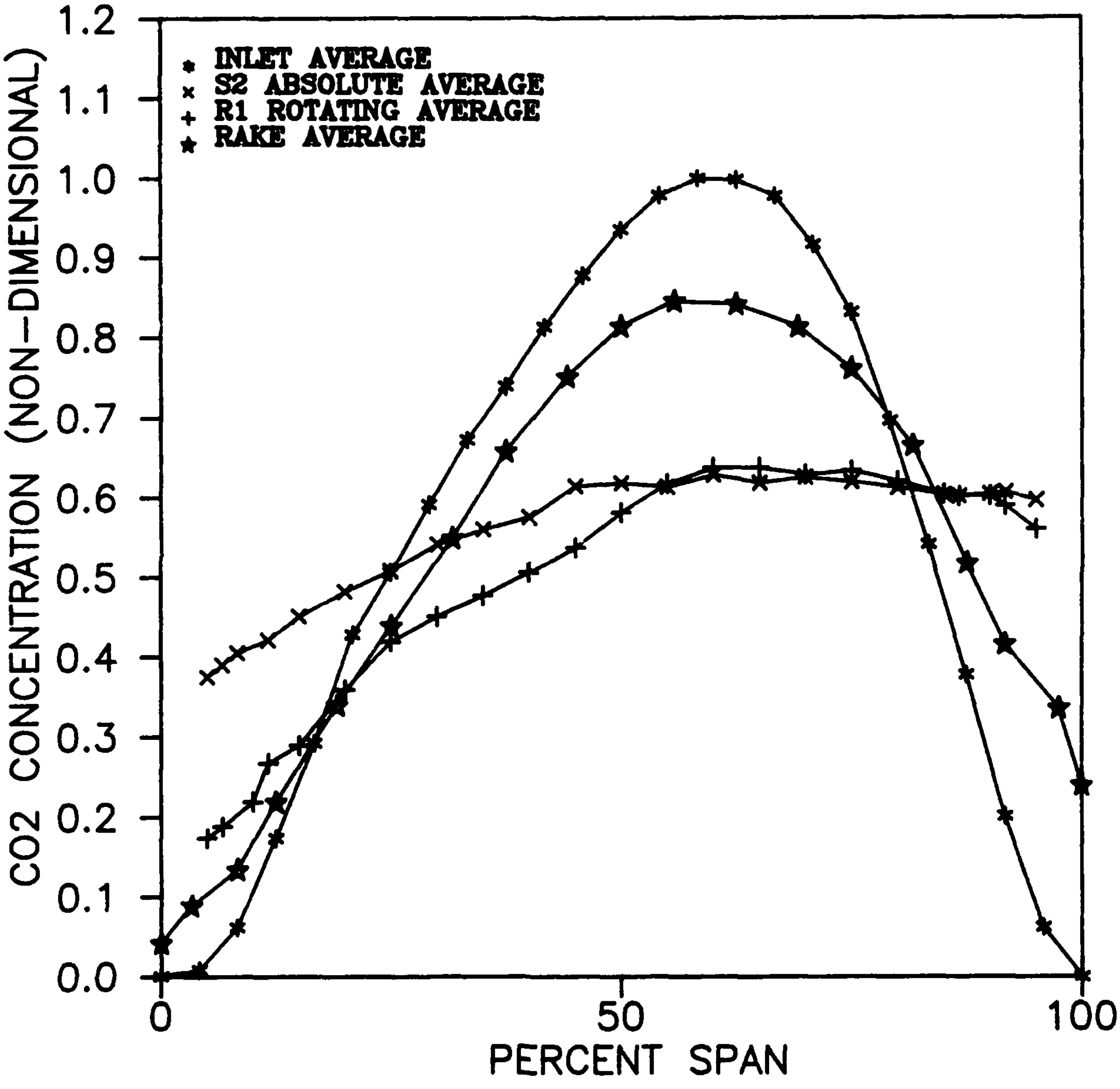

Fig. V–28 Comparison of Concentration Profiles at Planes 1, 2, 3 and 4

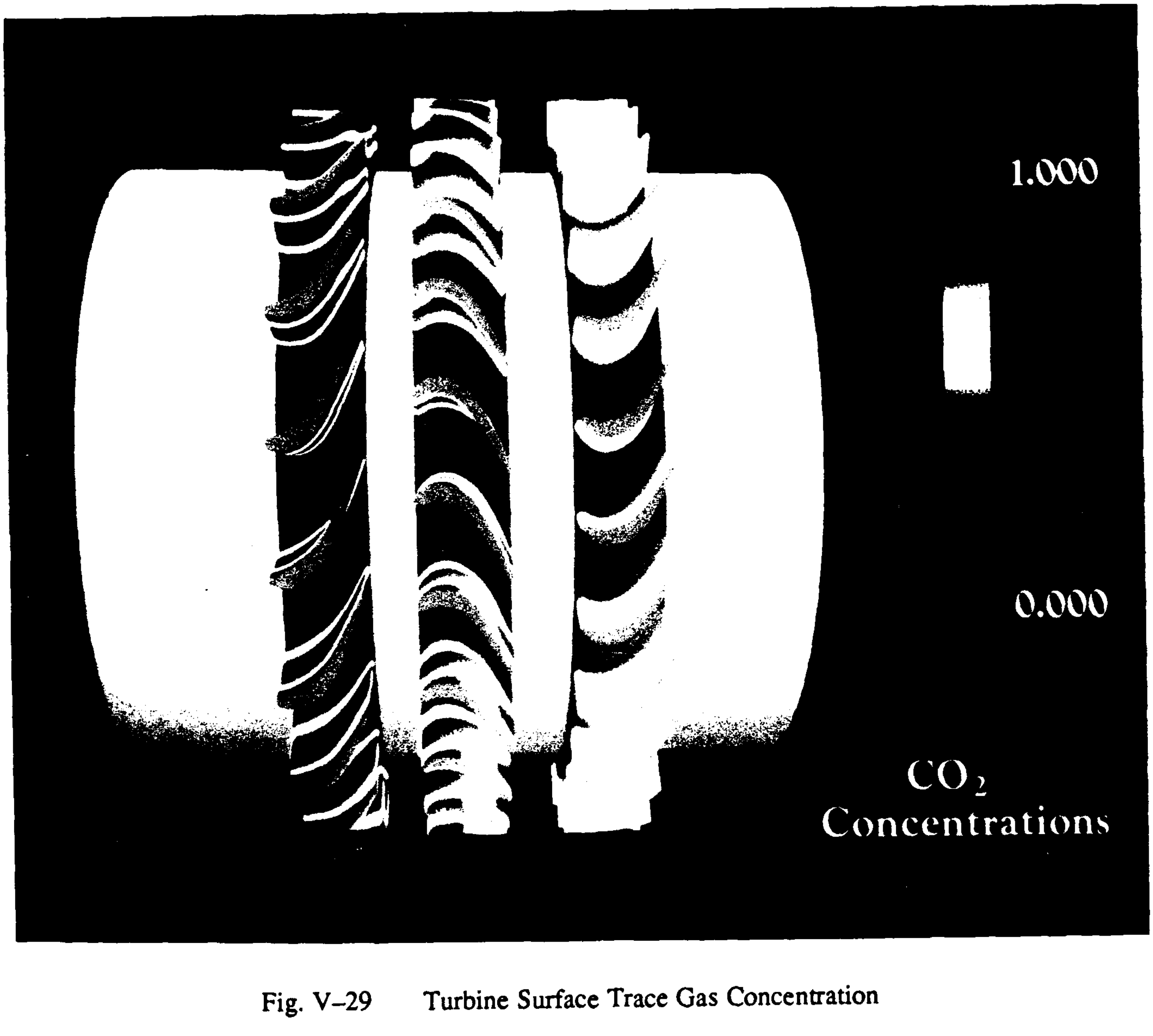

Fig. V–29 Turbine Surface Trace Gas Concentration